Nernst effect of Ni-doped $NdBa_2Cu_3O_{7-\delta}$ and transport properties in UPt_2Si_2

Inaugural Dissertation

zur

Erlangung des Doktorgrades
der mathematisch-naturwissenschaftlichen Fakultät
der Universität zu Köln

vorgelegt von

Niko Johannsen

aus Mainz

Köln, im Mai 2008

Berichterstatter:	Prof. Dr. A. Freimuth Prof. Dr. A. Schadschneider
Vorsitzender der Prüfungskommission:	Prof. Dr. U. Ruschewitz
Tag der mündlichen Prüfung:	26.6.2008

Was hinter jener Kurve ist -
Ich weiß es nicht.
Du weißt es nicht.
Es rauszufinden ist die Pflicht,
Die uns das Schicksal zugemißt.

Nein: zugemußt. Nein: zugemaßt.
Ich weiß es nicht.
Weißt Du es denn?

Robert Gernhardt

Contents

1 Introduction **1**

2 Formal Transport Theory **5**
- 2.1 Basic equations 5
  - 2.1.1 Electric conductivity in a magnetic field 6
  - 2.1.2 Heat conductivity in a magnetic field 6
- 2.2 Galvanomagnetic effects 6
  - 2.2.1 Isothermal test conditions 7
  - 2.2.2 Adiabatic test conditions 7
- 2.3 Thermomagnetic effects 7
  - 2.3.1 Isothermal test conditions 8
  - 2.3.2 Adiabatic test conditions 8
  - 2.3.3 Relations between transport coefficients 9
  - 2.3.4 Notations 9

3 Introducing the Seebeck and Nernst Effects **11**
- 3.1 Seebeck effect 11
- 3.2 Nernst effect 14
  - 3.2.1 Finite magnetic field 14
- 3.3 Some examples 16
  - 3.3.1 Bismuth 16
  - 3.3.2 $NbSe_2$ 17
  - 3.3.3 URu_2Si_2 18
  - 3.3.4 $CeCoIn_5$ 19
  - 3.3.5 Ferromagnetic materials 20
- 3.4 Nernst effect in the vortex liquid phase 21

4 Superconductivity **23**
- 4.1 Introduction 23
  - 4.1.1 Theoretical background 23
  - 4.1.2 Pinned and depinned vortices 27
- 4.2 Vortex dynamics 30
  - 4.2.1 Voltages in high-T_c materials 30
  - 4.2.2 Some forces on vortices 31
  - 4.2.3 Vortex motion in a transport current 32

4.2.4 Spectral flow . . . 35
4.2.5 Vortex motion in a temperature gradient . . . 41
4.2.6 Summary . . . 43
4.3 The system $NdBa_2\{Cu_{1-y}Ni_y\}_3O_{7-\delta}$ . . . 44
4.3.1 Structure . . . 44
4.3.2 Doping . . . 46
4.4 Pseudogap - a brief overview . . . 50

5 Experimental 53
5.1 Measurement of transport properties . . . 53
5.1.1 Preparing electrical contacts . . . 53
5.1.2 Stabilizing temperature and magnetic field . . . 56
5.1.3 Sweeping the field or the temperature . . . 57
5.2 Data analysis . . . 59
5.2.1 Extracting the Nernst signal . . . 59
5.2.2 Sign conventions . . . 61
5.2.3 Error analysis . . . 61
5.2.4 Nernst effect calibration in $La_{2-x}Sr_xCuO_4$ . . . 63

6 Motivation 67

7 Nernst Effect and Transport in Ni-doped $NdBa_2Cu_3O_{7-\delta}$ 73
7.1 Thermal conductivity . . . 74
7.1.1 Introduction . . . 74
7.1.2 Data and analysis . . . 75
7.2 Seebeck effect . . . 80
7.2.1 Introduction . . . 80
7.2.2 Data and analysis . . . 80
7.3 Nernst effect . . . 87
7.3.1 Data and analysis . . . 87
7.3.2 Phasediagram, conclusion and outlook . . . 91
7.4 Thermal Hall angle . . . 96

8 Nernst Effect and Transport in UPt_2Si_2 101
8.1 Motivation . . . 101
8.2 Physical background . . . 101
8.3 Magnetic properties and structure of UPt_2Si_2 . . . 103
8.4 Measurements and analysis . . . 103
8.4.1 Configuration $(\nabla T, j) \parallel a$, $B \parallel c$ . . . 104
8.4.2 Configuration $\nabla T \parallel c$, $B \parallel a$ . . . 113
8.4.3 Conclusion . . . 116

9 Summary 117

List of Figures **123**

Bibliography **125**

Publications **137**

Danksagung **139**

Offizielle Erklärung **141**

Abstract **143**

Kurzzusammenfassung **145**

1 Introduction

Since the discovery of high-temperature superconductivity by Bednorz and Müller more than 20 years ago [1], the search for its mechanism is enthusiastically carried on. Still driven by the dream of superconductivity at room temperature, many promising experiments are performed in this special class of ceramic superconductors. It is known that magnetic fields can enter into these systems in units of elementary flux quanta. Such a flux line is encircled by a supercurrent of Cooper-pairs [2]. The whole entity is referred to as "vortex". These structures can be forced to move through the sample by either applying a temperature gradient or a transport current. A moving vortex produces a voltage which is directed perpendicular to its moving direction. This is due to quantum-mechanically induced "phase-slips". When vortices move down the temperature gradient a voltage perpendicular to ∇T is detected. This is the Nernst effect. Introduced by Nernst and Ettingshausen in 1886 [3], this effect was long time left unnoticed, mainly because it is vanishingly small in normal metals. Nowadays, the impact of this effect truly justifies calling it a "renaissance" of the Nernst effect. This is because it turned out that the transverse voltage in the vortex liquid phase causes an extraordinary large anomalous Nernst effect that is highly non-linear in its magnetic field dependence. These findings immediately identified the Nernst effect as one of the most sensitive tools for the detection of the motion of vortices or vortex-like excitations. In 2000 [4], Xu *et al.* published the finding of large Nernst signals lasting to temperatures far above the critical temperature (T_c) in $\mathrm{La_{2\text{-}x}Sr_xCuO_4}$. The interpretation was straightforward: Since vortices are unambiguously related to superconductivity, there has to be at least some fraction of superconducting densities above T_c. Depending on the charge carrier concentration, T_c forms a superconducting dome in the cuprates. If we now leave the superconducting dome on the underdoped side by increasing the temperature above T_c, it turns out that the system is still far from behaving like a normal metal. Up to temperatures as high as room temperature there is a so-called "pseudogap" phase. Pseudo refers to the fact the density of states is only reduced rather than zeroed, as in a normal gap. This observation was based on data of optical conductivity measurements [5]. The nature of this phase is discussed in terms of an onset of a spin-pairing mechanism, similar to the Cooper-pair formation at T_c [6–8]. It seems to be a good approach towards the understanding of the mechanisms of high-T_c superconductivity to first understand the normal state from which it arises.

Here, the Nernst effect comes back into play. Its sensitivity in detecting signatures of the superconducting state can be exploited to unravel possible relations between the pseudogap and superconductivity. As a function of charge carrier doping in the cuprates, T_c is found to increase until a maximum value is reached while the pseudogap temperature T^* decreases. By determining the onset temperatures of the anomalous Nernst signal in this doping range, it is very interesting to observe whether it shows some scaling behavior with either one of the two phases. Such measurements were carried out by Wang *et al.* [9], obtaining onset temperatures that were interpreted as tracking T^*.

In order to further investigate this aspect, it would be very helpful to examine a system in which the most relevant parameters, T_c and T^*, can be tuned individually. Given such a system, one could examine whether there is a relation between the pseudogap and superconductivity by shifting the pseudogap and observing if the Nernst signal follows or not. Fortunately, such a system exists, namely $NdBa_2\{Cu_{1-y}Ni_y\}_3O_{7-\delta}$. Recent measurements of the optical conductivity of Ni-doped $NdBa_2Cu_3O_{7-\delta}$ revealed a strongly enhanced pseudogap while superconductivity is suppressed at the same time [10]. This compound therefore offers the unique opportunity to study the development of the Nernst signal while tuning T_c and the pseudogap individually and even in opposite directions. This is the systematic investigation that is presented in this work. The measurements were performed on a series of optimally doped (O_7) and two series of underdoped ($O_{6.8}$ and $O_{6.9}$) samples with Ni contents ranging from y = 0 to 0.12. These data as well as a detailed analysis of their scaling relations with either T_c or T^* represent the heart of this thesis.

The second part of this work leaves the physics of the high-T_c's, but still deals with the Nernst effect. After extensive studies of the Nernst effect in the high-T_c's, it was also studied in some superconductors with low T_c's. Among them were samples of the class of the "heavy Fermions". There it turned out that large Nernst effects are also present in other phases but the superconducting one. As an example, in URu_2Si_2, which is superconducting below 1.5 K, a Nernst signal could be resolved below 17.5 K [11]. This temperature marks the onset of a mysterious phase referred to as "hidden-order" phase. Consequently, new mechanisms had to be discussed as sources of an enhanced Nernst signal in such systems. These mechanisms are searched for quite similar to the analysis of the physics of the thermopower by means of the Mott formula. An "altered" Mott formula for the Nernst effect suggests that a large Nernst signal can be caused by small Fermi energies and long scattering times, in some simple cases. These conditions can be met in very clean systems with low itinerant charge carrier densities. The findings of a large Nernst effect that emerges with the onset of the mysterious "hidden-order" in URu_2Si_2 impelled the investigation of the Nernst effect in the related system UPt_2Si_2 in this work. UPt_2Si_2 is a system that is neither superconducting nor is it a heavy Fermion. It is a local moment antiferromagnet with an ordering temperature of $\simeq 31$ K [12]. The more surprising that a pronounced Nernst effect is found to emerge with the antiferromagnetic ordering. Not only the Nernst signal, but a detailed analysis of all participating transport properties has been performed in this work. Additional measurements of the Seebeck and Hall effects, the magnetoresistivity and the thermal Hall effect, also referred to as Righi-Leduc effect, are shown. An early theory, published in 1972 [13, 14], calculated the thermopower and the Nernst effect for generic antiferromagnets. Included in the calculations is the appearance of a charge gap at the Fermi surface upon entering into the antiferromagnetic order. This gap, together with a modeling of spin and phonon scattering mechanisms leads to a substantial increase of the thermomagnetic quantities according to the predictions of the theory. The measurements on UPt_2Si_2 and a detailed comparison to the results of this theory are shown in the second part of this thesis.

This thesis is organized as follows: Chapter 2 formally introduces the transport coefficients that are of importance here, with special emphasis on the difference of isothermal and adiabatic test conditions. In chapter 3, the Nernst effect is discussed in more detail. By some examples of recent studies, different mechanisms that are proposed to effect large Nernst signals are illustrated. Chapter 4 briefly introduces the theory of superconductivity with emphasis on properties of the high-T_c's that is needed to become familiar with the vocabulary used later on. It further illustrates how vortices produce voltages in situations of applied transport currents and temperature gradients. Chapter 5 describes in detail the experimental subtleties of this work. Chapter 6 gives a detailed motivation for the investigation of this work. Finally the measurements and the detailed analysis are presented in chapter 7. The investigation of transport properties of UPt_2Si_2 is completely covered in chapter 8 and the main results are summarized in chapter 9.

2 Formal Transport Theory

2.1 Basic equations

In this chapter a brief overview into the basic theory of transport phenomena will be given. First the general definitions of the transport coefficients will be introduced as they are derived from statistical mechanics. Then some special cases are discussed as the main focus of this thesis lies in measurements of the Nernst effect, the thermopower or Seebeck effect and the thermal conductivity. A detailed derivation of the transport equations is given in refs. [15–22]. The tensor equations for the charge and heat current densities are:

$$\mathbf{j} = \mathbf{L_{11}}\mathbf{E} + \mathbf{L_{12}}(-\nabla\,\mathbf{T}) \qquad \text{and} \tag{2.1}$$

$$\mathbf{j_h} = \mathbf{L_{21}}\mathbf{E} + \mathbf{L_{22}}(-\nabla\,\mathbf{T}). \tag{2.2}$$

Solving these equations for the heat current density $\mathbf{j_h}$ and the electric field $\mathbf{E}$, we get

$$\mathbf{E} = \rho\mathbf{j} + \mathbf{S}\nabla\,\mathbf{T} \qquad \text{and} \tag{2.3}$$

$$\mathbf{j_h} = \mathbf{\Pi}\mathbf{j} - \kappa\nabla\,\mathbf{T}. \tag{2.4}$$

The coefficients used above are defined by

$$\text{Electrical resistivity tensor:} \qquad \rho = (\mathbf{L_{11}})^{-1}, \tag{2.5}$$

$$\text{Seebeck tensor:} \qquad \mathbf{S} = (\mathbf{L_{11}})^{-1} \cdot \mathbf{L_{12}}, \tag{2.6}$$

$$\text{Peltier tensor:} \qquad \mathbf{\Pi} = \mathbf{L_{21}} \cdot (\mathbf{L_{11}})^{-1}, \tag{2.7}$$

$$\text{Heat conductivity tensor:} \qquad \kappa = \mathbf{L_{22}} - \mathbf{L_{21}} \cdot (\mathbf{L_{11}})^{-1} \cdot \mathbf{L_{12}}. \tag{2.8}$$

In the presence of a magnetic field, the tensor coefficients in equations (2.1) and (2.2) fulfill the symmetries that depend on the magnetic field according to the universal Onsager relations,

$$\mathbf{L_{11}}(\mathbf{B}) = \mathbf{L_{11}}^{T}(-\mathbf{B}), \qquad \mathbf{L_{22}}(\mathbf{B}) = \mathbf{L_{22}}^{T}(-\mathbf{B}), \qquad \mathbf{L_{12}}(\mathbf{B}) = \mathbf{L_{21}}^{T}(-\mathbf{B}). \tag{2.9}$$

and thereby

$$\rho_{ij}(\mathbf{B}) = \rho_{ji}(-\mathbf{B}), \qquad \kappa_{ij}(\mathbf{B}) = \kappa_{ji}(-\mathbf{B}), \qquad S_{ij}(\mathbf{B}) = S_{ji}(-\mathbf{B}), \qquad \Pi_{ij}(\mathbf{B}) = \Pi_{ji}(-\mathbf{B}). \tag{2.10}$$

2.1.1 Electric conductivity in a magnetic field

All external sources such as electric currents or temperature gradients are defined to be applied in x direction as not mentioned otherwise. If a magnetic field is applied to the sample it will be in z direction. So the transverse effects will be monitored in y direction. For the electrical conductivity under the influence of a magnetic field, Eq. (2.3) becomes

$$E_x = \rho_{xx}(B) \cdot j_x + \rho_{xy}(B) \cdot j_y \qquad \text{and} \tag{2.11}$$

$$E_y = \rho_{yx}(B) \cdot j_x + \rho_{yy}(B) \cdot j_y, \tag{2.12}$$

which resembles the ohmic law. The symmetric part of the resistivity tensor can be written as

$$\rho_{xx}(B) = \frac{1}{2}\big(\rho(B) + \rho(-B)\big). \tag{2.13}$$

The symmetry can be deduced from Eq. (2.10),

$$\rho_{xx}(-B) = \rho_{xx}(B) \tag{2.14}$$

and means that all elements of the symmetric conductivity tensor are even functions of the magnetic field strength $\mathbf{B}$. For the antisymmetric part of the conductivity tensor

$$\rho_{xy}(B) = \frac{1}{2}\big(\rho(-B) - \rho(B)\big) \tag{2.15}$$

the symmetry relations (Eq. (2.10)) yield

$$\rho_{xy}(-B) = -\rho_{xy}(B). \tag{2.16}$$

This means that all elements of the antisymmetric part of the resistivity tensor are odd functions of the magnetic field. In the simplest case the Hall-resisivity (ρ_{xy}) is proportional to $\mathbf{B}$. The whole effect that is caused by the antisymmetric part of the resistivity tensor is known as the Hall effect.

2.1.2 Heat conductivity in a magnetic field

In the same way as described above we derive for the heat conductivity in a magnetic field (from (2.4)):

$$j_{qx} = -\kappa_{xx}(B) \cdot \nabla_x T - \kappa_{xy}(B) \cdot \nabla_y T, \tag{2.17}$$

where the heat conductivity tensor κ also has been decomposed into a symmetric (κ_{xx}) and an antisymmetric (κ_{xy}) part. The whole antisymmetric part of the heat conductivity tensor is responsible for the Righi-Leduc effect.

2.2 Galvanomagnetic effects

Galvanomagnetic effects are defined as the resulting effects of externally applied electric currents and magnetic fields. These effects can be further classified into longitudinal effects (subscript xx or yy), where the measurand and the cause are oriented parallel and transverse effects (subscript xy or yx), where they are oriented perpendicular to each other.

2.2.1 Isothermal test conditions

Here, isothermal means a vanishing temperature gradient throughout the whole sample, $\nabla T = 0$. The two effects of this class are:

$$\text{isothermal electric resistivity:} \quad \rho^i_{xx} \equiv \frac{E_x}{j_x} \quad \text{and} \tag{2.18}$$

$$\text{isothermal Hall effect:} \quad \rho^i_{xy} \equiv \frac{E_y}{j_x}. \tag{2.19}$$

2.2.2 Adiabatic test conditions

Adiabatic means a vanishing temperature gradient along the direction of the injected charge current, $\nabla T_x = 0$. A transverse temperature gradient is now present, $\nabla T_y \neq 0$ while no transverse heat currents are allowed, $(j_h)_y = 0$. The associated transport effects are:

$$\text{adiabatic electric resistivity:} \quad \rho^a_{xx} \equiv \frac{E_x}{j_x}, \tag{2.20}$$

$$\text{adiabatic Hall effect:} \quad \rho^a_{xy} \equiv \frac{E_y}{j_x} \quad \text{and} \tag{2.21}$$

$$\text{Ettingshausen effect:} \quad \epsilon^a \equiv \frac{(\nabla T)_y}{j_x}. \tag{2.22}$$

The transport equations (2.3) and (2.4) can now be written as

$$E_x = \rho_{xx} j_x + S_{xy} (\nabla T)_y, \qquad E_y = \rho_{yx} j_x + S_{yy} (\nabla T)_y \qquad \text{and} \tag{2.23}$$

$$(j_h)_x = \Pi_{xx} j_x - \kappa_{xy} (\nabla T)_y, \qquad 0 = -\Pi_{yx} j_x - \kappa_{yy} (\nabla T)_y. \tag{2.24}$$

Solving these equations leads to the formulation of the transport coefficients as

$$\rho^a_{xx} = \rho^i_{xx} - \frac{\Pi_{xy} S_{xy}}{\kappa_{xx}}, \tag{2.25}$$

$$\rho^a_{xy} = \rho^i_{xy} - \frac{\Pi_{xy} S_{xx}}{\kappa_{xx}}, \tag{2.26}$$

$$\epsilon = -\frac{\Pi_{xy}}{\kappa_{xx}}. \tag{2.27}$$

2.3 Thermomagnetic effects

Thermomagnetic effects are defined as the resulting effects of externally applied heat currents and magnetic fields. The classification into longitudinal and transverse effects is analogous to section 2.2.

2.3.1 Isothermal test conditions

Here, isothermal means a vanishing transverse temperature gradient, $(\nabla T)_y = 0$ while no charge current is allowed to flow, $\mathbf{j} = 0$. The following effects are classified under these conditions:

$$\text{isothermal heat conductivity:} \qquad \kappa^i \equiv -\frac{(j_h)_x}{(\nabla T)_x}, \tag{2.28}$$

$$\text{isothermal Nernst effect:} \qquad Q^i \equiv \frac{E_y}{(\nabla T)_x}, \tag{2.29}$$

$$\text{isothermal thermoelectric power:} \qquad S^i \equiv \frac{E_x}{(\nabla T)_x}. \tag{2.30}$$

The transport equations (2.3) and (2.4) turn to

$$E_x = S_{xx}(\nabla T)_x, \qquad E_y = -S_{yx}(\nabla T)_x \qquad \text{and} \tag{2.31}$$

$$(j_h)_x = -\kappa_{xx}(\nabla T)_x, \qquad (j_h)_y = \kappa_{yx}(\nabla T)_x, \tag{2.32}$$

with

$$\kappa^i = \kappa_{xx}, \tag{2.33}$$

$$Q^i = -S_{xy} \qquad \text{and} \tag{2.34}$$

$$S^i = S_{xx}. \tag{2.35}$$

2.3.2 Adiabatic test conditions

Again, no charge current is allowed, $\mathbf{j} = 0$, while a transverse temperature gradient is now present, $\nabla T_y \neq 0$, but without a heat current along y ($(j_h)_y = 0$). The following effects can result from these conditions:

$$\text{adiabatic heat conductivity:} \qquad \kappa^a \equiv -\frac{(j_h)_x}{(\nabla T)_x}, \tag{2.36}$$

$$\text{adiabatic Nernst effect:} \qquad Q^a \equiv \frac{E_y}{(\nabla T)_x}, \tag{2.37}$$

$$\text{adiabatic thermoelectric power:} \qquad S^a \equiv \frac{E_x}{(\nabla T)_x}, \tag{2.38}$$

$$\text{Righi-Leduc effect:} \qquad R^a \equiv \frac{(\nabla T)_y}{(\nabla T)_x}. \tag{2.39}$$

The transport equations (2.3) and (2.4) turn out to be

$$E_x = S_{xx}(\nabla T)_x + S_{xy}(\nabla T)_y, \qquad E_y = -S_{yx}(\nabla T)_x + S_{yy}(\nabla T)_y \qquad \text{and} \tag{2.40}$$

$$(j_h)_x = -\kappa_{xx}(\nabla T)_x - \kappa_{xy}(\nabla T)_y, \qquad 0 = \kappa_{yx}(\nabla T)_x - \kappa_{yy}(\nabla T)_y, \tag{2.41}$$

and the coefficients can be written as

$$\kappa^a = \kappa_{xx} + \frac{\kappa_{xy}^2}{\kappa_{xx}}, \tag{2.42}$$

$$Q^a = -S_{xy} + \frac{\kappa_{xy}}{\kappa_{xx}} S_{xx}, \tag{2.43}$$

$$S^a = S_{xx} + \frac{\kappa_{xy}}{\kappa_{xx}} S_{xy}, \tag{2.44}$$

$$R^a = \frac{\kappa_{xy}}{\kappa_{xx}}. \tag{2.45}$$

2.3.3 Relations between transport coefficients

Using the Onsager relation $TS_{xy} = \Pi_{xy}$ and inserting the coefficients defined in equations (2.27) and (2.34) one derives

$$TQ = \kappa\epsilon \qquad \text{and} \tag{2.46}$$

$$TS = \Pi, \tag{2.47}$$

which are known as the Bridgeman and the Kelvin relation, respectively. The experimental relevance of these two relations is expressed by the physical equivalence of either applying an electric current to the sample and measuring a thermal response or applying a heat current and measuring the electric response. This equivalence holds for both situations: the longitudinal response, Eq. (2.47), and the transverse one, Eq. (2.46).

2.3.4 Notations

Recent publications denote the Nernst effect with the following expressions: A Nernst signal, which is mostly assigned to the characters e_y [23, 24], e_N [25, 26] or N [11, 27] and is equivalent to $-Q$ in this formal introduction. For the Nernst coefficient, which is the signal divided by the magnetic field B, $\nu = e_y/B$ is now widely used.

3 Introducing the Seebeck and Nernst Effects

Thomas Johann Seebeck discovered in 1821 that a metal bar which is heated solely at one end produces a voltage between its two ends. This effect is called Seebeck effect [28]. It should be mentioned here, that it is not restricted to metals. In fact, the voltage usually gets larger, the less conducting the material is.

The Nernst-Ettingshausen effect or Ettingshausen-Nernst effect has been formulated by Walther Nernst and his coworker Albert von Ettingshausen in 1887 and is mostly referred to as Nernst effect today [3]. When a conductor or semiconductor is subjected to a temperature gradient and to a magnetic field perpendicular to the temperature gradient, an electric field arises perpendicular to both the temperature gradient and the magnetic field. So, practically spoken, it is easy to expand a Seebeck experiment to a Nernst effect experiment by adding two electrical contacts perpendicular to the applied longitudinal temperature gradient and to turn on a magnetic field.

Under the influence of this externally applied magnetic field, the entropy carrying charge currents are subject to the Lorentz force and thereby can give rise to the Nernst effect. Both of these effects will be introduced in detail in this chapter, starting with the Seebeck effect. The second part will take care of the Nernst effect in the normal (non superconducting) state and normal metals (basically following the argumentation of [25]). These effects will be accompanied by some examples of recent measurements. The high-T_c superconductors have to be treated in a completely different way, this is subject to a detailed analysis in chapter 4.

3.1 Seebeck effect

We consider a thermal gradient along the x-direction of a sample as schematically drawn in Fig. 3.1 without an external magnetic field. Driven by the temperature gradient is a charge current density, $j_x^{th} = \alpha_{xx}(-\partial_x T)$. α_{xx} denotes the part of the Peltier conductivity tensor that acts along the temperature gradient. Since this is a diffusion process, it is intuitively clear that α will be closely related to the entropy of the charge carriers involved. For j_x^{th}, the superscript th stands for "thermally driven" and is not to be confused with a heat current. The boundary conditions require that the total electrical current remains zero since no charge supply is connected to the sample. Therefore, an electrical field E_x develops which drives the colder and slower charge carriers in the opposite direction. This charge current is denoted by $j_x^E = \sigma_{xx} E_x$. Here, the superscript E should be read as "electric field driven".

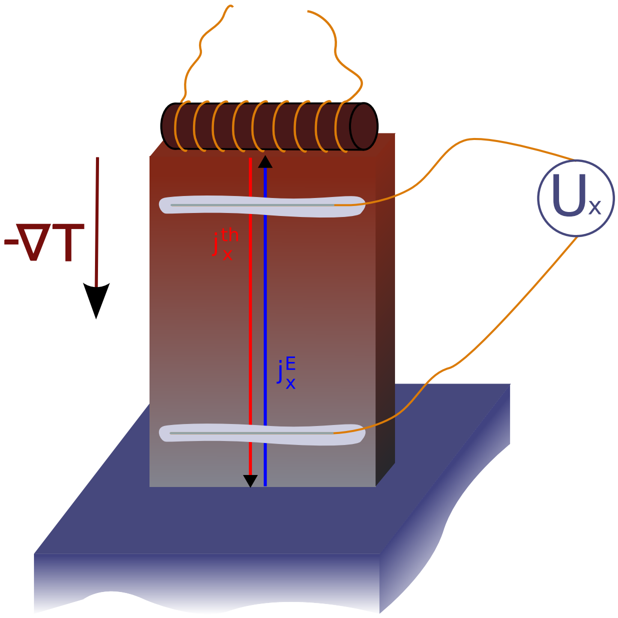

Figure 3.1: Illustration of the Seebeck effect or thermopower, arising from two electric current densities of opposite directions and equal magnitude: One is thermally driven from the hot to the cold end, $j_x^{th} = \alpha_{xx}(-\partial_x T)$ and $j_x^E = \sigma_{xx} E_x$ is caused by the electric field that is set up by the condition $j_x = 0$. Consequently, a voltage develops between the two contacts, U_x.

The resulting equilibrium gives a thermopower equation,

$$0 = \sigma_{xx} E_x + \alpha_{xx}(-\partial_x T). \tag{3.1}$$

Thus,

$$E_x = -(\alpha_{xx}/\sigma_{xx})(-\partial_x T) \tag{3.2}$$

defines the Seebeck coefficient as $S_{xx} = \alpha_{xx}/\sigma_{xx}$.

Now that all the physical quantities such as temperature gradient, electric field and the resulting currents are assumed to be perfectly aligned along one of the principal axis in the situation sketched above (in orthogonal systems), α and σ lose their tensor character and can also be written as scalars. This will be used from now on. The temperature dependence of the diffusion thermopower can be modeled within a Boltzmann picture which leads to the formulation of the Mott formula as [17, 29–31]

$$S_d = -\frac{\pi^2 k_B^2 T}{3e} \frac{\partial \ln \sigma(\epsilon)}{\partial \epsilon} |_{\epsilon_F}, \tag{3.3}$$

with $\sigma(\epsilon)$ being the energy-dependent conductivity and ϵ_F the Fermi energy. $\sigma(\epsilon)$ is related with the scattering time $\tau(\epsilon)$ via [17]

$$\sigma(\epsilon) = e^2 \tau(\epsilon) \int \frac{d\mathbf{k}}{4\pi^3} \delta(\epsilon - \epsilon(\mathbf{k})) v(\mathbf{k}) v(\mathbf{k}), \tag{3.4}$$

with $\mathbf{k}$ being the electron wavevector. Inserting this expression into Eq. (3.3), it becomes clear that the thermopower contains information on both, transport and thermodynamic properties of the system.

$$S_d = -\frac{\pi^2 k_B^2 T}{3e}\left[\left(\frac{\partial \ln \tau(\epsilon)}{\partial \epsilon}\right)_{\epsilon_F} + \frac{\int d\mathbf{k}\delta(\epsilon - \epsilon(\mathbf{k}))\mathbf{M}^{-1}(\mathbf{k})}{\int d\mathbf{k}\delta(\epsilon - \epsilon(\mathbf{k}))v(\mathbf{k})v(\mathbf{k})}\right] \tag{3.5}$$

The purely thermodynamic term is given by the right side of Eq. (3.5) with $\mathbf{M}^{-1}$ being the inverse of the effective mass tensor. This term reduces to $3/(2\epsilon_F)$ in the case of a free electron gas. Furthermore, according to [32] the scattering time can be modeled by

$$\tau(\epsilon) = \tau_0 \epsilon^{\zeta}, \tag{3.6}$$

leading to a fairly simple expression for the Seebeck coefficient of a free electron gas:

$$S_d = -\frac{\pi^2 k_B^2}{3e}\frac{T}{\epsilon_F}\left(\zeta + \frac{3}{2}\right). \tag{3.7}$$

In the simplest case of an energy independent scattering time, ζ is zero and in the case of a constant mean free path l_e, implying $\tau = l_e/v \propto \epsilon^{-1/2}$, the exponent becomes $\zeta = -1/2$. In the low temperature limit the energy independent mean free path is believed to hold even in the presence of strong correlations [33]. $\zeta = -1/2$ then leads to the well known linear temperature dependence of S_d that is also expressed by Cohn *et al.* when discussing the high-T$_c$ thermopower [34].

$$S_d = -\frac{\pi^2 k_B^2}{3e}\frac{T}{\epsilon_F} = -\frac{2\pi^2 k_B^2}{9e}\frac{TD(\epsilon_F)}{n}. \tag{3.8}$$

Here, the Fermi energy is related to the density of states $D(\epsilon_F)$ and the carrier concentration n for free electrons by the relation $D(\epsilon_F) = 3n/(2\epsilon_F)$.

Other than caused just by the diffusion process described above, the thermopower can be influenced by mechanisms that are due to interactions of charge carriers and phonons. In high-temperature regimes (typically $T \geq \Theta_D$), anharmonic phonon-phonon interactions are dominant, leading to a quasi equilibrium of the lattice. Here the thermopower is dominated by the diffusion term, S_d. In the low temperature regime and under the influence of an applied temperature gradient, the lattice is no longer to be considered in a state of equilibrium. A flow of phononic excitations is the consequence of the temperature gradient and can cause a transfer of energy and impulse to the charge carriers. Phonons drag the carriers with the movement. Depending on the scattering time between electrons and phonons, $\tau_{p,e}$ and the scattering time of phonons with other arbitrary excitations, $\tau_{p,x}$ this phonon drag term is described as

$$S_g = -\frac{c_v}{3Ne}\frac{\tau_{p,x}}{\tau_{p,x} + \tau_{p,e}}, \tag{3.9}$$

with c_v being the phononic specific heat [32]. Then, the measured thermopower has contributions of both parts,

$$S = S_d + S_g. \tag{3.10}$$

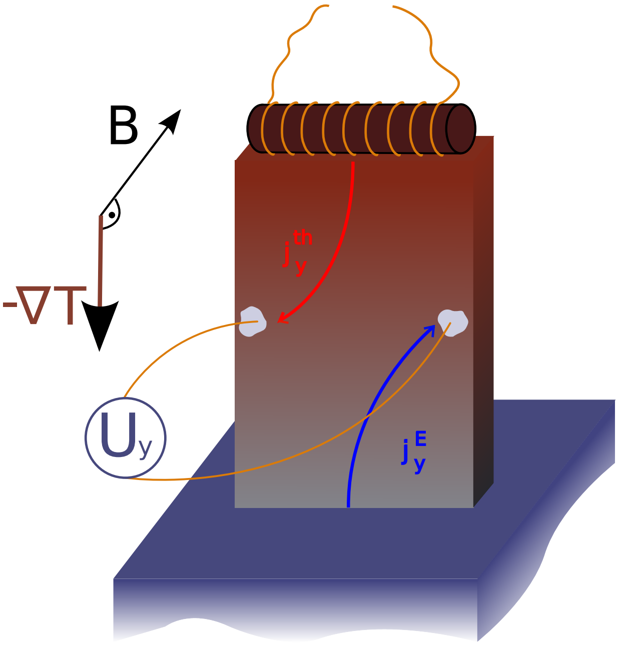

Figure 3.2: Illustration of the isothermal Nernst effect in a metal. Two electric current densities tend to cancel each other because of their opposing deflections due to the Lorentz force: One that is thermally driven from the hot to the cold end, $j_y^{th} = \alpha_{yx}(-\partial_x T)$ and $j_y^E = \sigma_{yx}E_x$ is caused by the electric field that is set up by the condition $j_x = 0$. If j_y^{th} and j_y^E are not equal, a Nernst voltage develops in transverse direction (U_y) due to the second condition $j_y = 0$.

3.2 Nernst effect

Now that it is explained how voltages develop in a temperature gradient, we just have to turn on a magnetic field perpendicular to the temperature gradient and the charge current densities of Fig. 3.1. The charge currents are then subjected to the Lorentz force and driven aside in opposite directions, which is the reason for the usually small voltages. This is sketched in Fig. 3.2.

3.2.1 Finite magnetic field

Isothermal Nernst effect, $\nabla T_y = 0$

For isothermal conditions, we assume that the temperature gradient has no contributions in y-direction. Whether this condition can safely be assumed in experiment or not has to be considered individually for every system. In the cuprate family, however, the phononic thermal conductivity is more than ten times larger than the electronic thermal conductivity. Therefore the phonons are able to short circuit any developing temperature gradient in y direction, and consequently $\nabla T_y \approx 0$ is assumed [25]. This will be of importance when the Nernst effect of a member of this cuprate family is discussed in chapter 7. In addition to the longitudinal charge current densities that define the thermopower in Eq. (3.2), the appliance of a magnetic field B directed perpendicular to the thermal gradient and the heat current leads to two additional types of currents which both are antisymmetric in B. The first is the Hall current $\sigma_{yx}E_x$ and the other is the off-diagonal Peltier current $\alpha_{yx}(-\partial_x T)$. These two parts are opposite in direction and equal in magnitude (see Fig.

3.2) in the simplest cases. Again the condition that no overall current flows along the direction perpendicular to the temperature gradient leads to

$$0 = j_y = \alpha_{yx}(-\partial_x T) + \sigma_{yx} E_x + \sigma_{yy} E_y. \tag{3.11}$$

The first two parts of the right side of Eq. (3.11) are the parts that set up a counterflow of charged particles. Only if they are not equal in magnitude a resulting electric field E_y develops which in turn sets up a Nernst voltage.

Adiabatic Nernst effect, $\nabla T_y \neq 0$

In the case that the transverse thermal conductivity κ_{xy} is non-zero, a transverse temperature gradient is set up. This effect is also referred to as Righi-Leduc effect. The last term of Eq. (3.12), $\alpha_{yy}(-\partial_y T)$ shows that a transverse temperature gradient is also able to contribute to a transverse electric field. This will be the case in metals in which the electronic thermal conductivity κ^e dominates the phonon conductivity κ^{ph}. Under these conditions the transverse thermal gradient produces an additional current in the direction of the Hall current $\sigma_{yx}E_x$. In other words, a transverse temperature gradient just sets up a thermopower voltage that superimposes the measured Nernst voltage.

$$0 = j_y = \alpha_{yx}(-\partial_x T) + \sigma_{yx} E_x + \sigma_{yy} E_y + \alpha_{yy}(-\partial_y T). \tag{3.12}$$

A Nernst experiment in which E_y is measured under these conditions does not yield the desired isothermal Nernst coefficient. In the presence of a pronounced Righi-Leduc effect, the transverse temperature gradient has to be measured additionally in order to subtract the contribution arising from the last term of the right hand side of Eq. (3.13):

$$\nu = \frac{E_y}{|\partial_x T| B} = \left[\rho \alpha_{xy} - S\left(\frac{\sigma_{xy}}{\sigma} + \frac{\kappa_{xy}}{\kappa}\right)\right]\frac{1}{B}, \tag{3.13}$$

with ν defining the Nernst coefficient. Several measurements of the off-diagonal component of the thermal conductivity, κ_{xy}, can be found in [35] and [36] for YBCO and in [25] as a comment for LSCO. An estimation can be given for the case of $YBa_2Cu_3O_{7-\delta}$ [36]. κ_{xx}(100K, 12 T)≈ 10 W/Km while κ_{xy}(100K, 12 T)≈ $5 \cdot 10^{-2}$ W/Km. Together with a thermopower magnitude of $S \approx$ -5 μV/K [37] the last term of Eq. (3.13) yields an absolute value of 25 nV/K as a contribution to the Nernst signal, which has typically a magnitude of about 200 nV/K at 100 K and 12 T [37]. The term $\alpha_{yy}(-\partial_y T)$ in Eq. (3.12) can thus be neglected in the cuprates and Eq.(3.12) reduces again to

$$\begin{aligned} 0 = j_y =& \alpha_{yx}(-\partial_x T) + \sigma_{yx} E_x + \sigma_{yy} E_y & (3.14)\\ =& \left[\alpha_{xy} - \sigma_{yx}\frac{\alpha_{xx}}{\sigma_{xx}}\right](-\partial_x T) + \sigma_{yy} E_y. & (3.15)\end{aligned}$$

Together with $\tan\theta = \sigma_{xy}/\sigma_{xx}$ Eq. (3.15) can be rewritten as

$$\nu_N = \frac{E_y}{|\partial_x T| B} = \left[\frac{\alpha_{xy}}{\sigma_{xx}} - \frac{\alpha_{xx}}{\sigma_{xx}}\frac{\sigma_{xy}}{\sigma_{xx}}\right]\frac{1}{B} = \left[\frac{\alpha_{xy}}{\sigma_{xx}} - S\tan\theta\right]\frac{1}{B}. \tag{3.16}$$

In the appendix of ref. [25] the carrier Nernst coefficient is expressed in a Boltzmann approach, very similar to the derivation of the Mott formula for the diffusion thermopower, compare Eq. (3.3). The off-diagonal Peltier conductivity then yields

$$\alpha_{xy} = \frac{\pi^2}{3} \frac{k_B^2 T}{e} \left[\frac{\partial \sigma_{xy}}{\partial \epsilon} \right]_{\epsilon_F} . \tag{3.17}$$

The diagonal components are expressed similarly [38],

$$\alpha = \frac{\pi^2}{3} \frac{k_B^2 T}{e} \left[\frac{\partial \sigma}{\partial \epsilon} \right]_{\epsilon_F} . \tag{3.18}$$

Inserting (3.17) and (3.18) into (3.16) gives an approximation for the Nernst coefficient

$$\nu = \frac{\pi^2}{3} \frac{k_B^2 T}{e} \frac{\theta}{B} \left[\frac{\partial \ln \theta}{\partial \epsilon} \right]_{\epsilon_F} , \tag{3.19}$$

using the simplification for small Hall-angles $\sigma_{xy}/\sigma \approx \theta$. Since the Hall-angle can be expressed as $\omega_c \tau$, with ω_c and τ being the cyclotron frequency and the scattering time, respectively, ν in Eq. (3.19) can be interpreted in measuring the energy dependence of the scattering time at the Fermi level. From Eq. (3.19) it becomes clear that if θ is not or only weakly dependent on energy at the Fermi level, the Nernst coefficient is zero or very small, respectively. The vanishing of the effect is often referred to as "Sondheimer cancellation" [38]. This seems to be a good estimation for conventional metals.

3.3 Some examples

While in single band metals the Nernst signal is usually very small, i.e. the isothermal Nernst coefficient of gold is of order $\sim 0.1\,\mathrm{nV/KT}$ [11], other mechanisms can lead to much larger signals. Some of those mechanisms will be briefly introduced here, starting with bismuth which is the system the original work of Nernst and Ettingshausen in 1886 was based on [3]. Some of the systems that are introduced here as examples are superconductors. But they are not high-T$_c$'s and have low critical temperatures. Let me stress that the Nernst effect that is found in these samples is not attributed to superconductivity as in the high-T$_c$'s. It is just the different mechanisms that are held responsible for large Nernst signals, that make them interesting.

3.3.1 Bismuth

Bismuth is characterized as one of the classical semimetals. A semimetal is usually thought of as a system with just a small overlap between valence band and conduction band. In a work of Behnia *et al.* [39] the Nernst effect of elemental bismuth is investigated, following the tracks of Nernst and Ettingshausen [3]. It is argued that in a Fermi liquid the Nernst

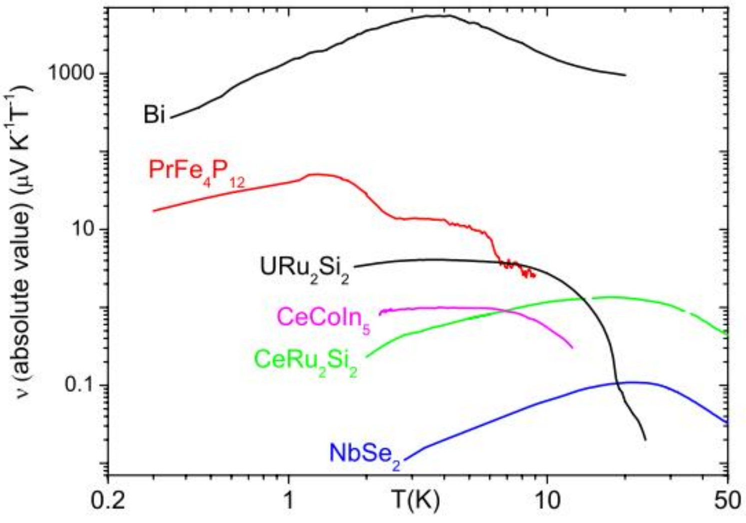

Figure 3.3: Comparison of the overall magnitude of Nernst signals for various materials in a double logarithmic plot with bismuth on top [39].

coefficient roughly tracks $\omega_c\tau/\epsilon_F$. Replacing θ by $\omega_c\tau$ and $\partial\tau/\partial\epsilon$ by τ/ϵ_F in Eq. (3.19) leads to a rough estimation of the Nernst signal [11],

$$\nu \approx 283\frac{\mu V}{K}\frac{\omega_c\tau}{B}\frac{k_BT}{\epsilon_F}. \tag{3.20}$$

Thus, enhanced T-linear Nernst coefficients can be found in systems combining a large scattering time, a reduced effective mass ($\omega_c \propto 1/m^*$) and a reduced carrier density which affects the Fermi energy. Finding all these features in bismuth together with a giant Nernst signal, the authors doubt that the emergence of a giant Nernst effect is solely related to exotic orders (e.g URu_2Si_2) but can also be found in materials that show the above described combination of physical properties. The magnitude of the Nernst coefficient is extraordinary large in bismuth as depicted in Fig. 3.3, overwhelming the Nernst coefficients of all other systems.

3.3.2 $NbSe_2$

Although $NbSe_2$ is a type-II superconductor with a transition temperature of $T_c = 7.2\,K$, the flux lines that penetrate the sample are basically pinned and cannot be responsible for the Nernst signal found here (this mechanism is discussed in detail in chapter 4).

Nevertheless, the magnitude of the Nernst signal in $NbSe_2$ is comparable to the vortex signal in the superconducting state of the high-T_c's [40]. The Fermi surface is believed to be three banded [41], so that more than one transport channel can contribute to a finite Nernst signal. In materials like $NbSe_2$, at least one electron and one hole channel has to

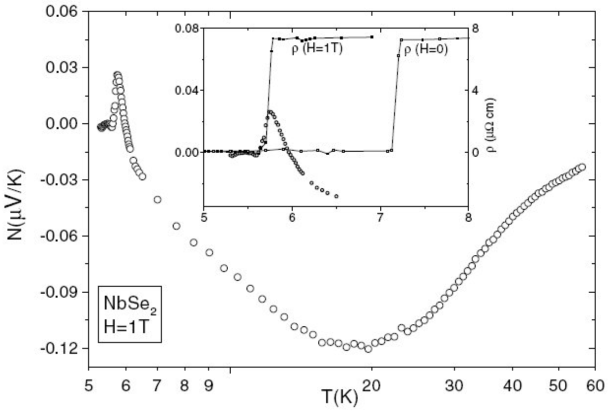

Figure 3.4: Ambipolar Nernst Effect in NbSe$_2$, measured at $H = 1\,\mathrm{T}$. Inset shows the shift of the resistive transition from $T_c = 7.2\,\mathrm{K}$ to about $5.7\,\mathrm{K}$ under the influence of $H = 1\,\mathrm{T}$ from [40].

be considered [42] and Eq. 3.16 is expanded to ([40, 42])

$$\nu_N = \frac{E_y}{|\partial_x T| B} = \frac{S}{B}\left(\frac{\alpha^+_{xy} + \alpha^-_{xy}}{\alpha^+_{xx} + \alpha^-_{xx}} - \frac{\sigma^+_{xy} + \sigma^-_{xy}}{\sigma^+_{xx} + \sigma^-_{xx}}\right), \tag{3.21}$$

with $S = (\alpha^+_{xx} + \alpha^-_{xx})/(\sigma^+_{xx} + \sigma^-_{xx})$ being the thermopower where the superscripts denote the sign of the dominant carriers. Here a finite transverse temperature gradient is neglected as well. Now this two band model would yield a finite Nernst signal which can be understood in the following picture. Even if a cancellation is valid separately for each band,

$$\frac{\alpha^+_{xy}}{\alpha^+_{xx}} = \frac{\sigma^+_{xy}}{\sigma^+_{xx}} \quad \text{and} \quad \frac{\alpha^-_{xy}}{\alpha^-_{xx}} = \frac{\sigma^-_{xy}}{\sigma^-_{xx}}, \tag{3.22}$$

the right side of Eq. (3.21) would not cancel out. If a compensated situation is assumed, i.e $\sigma^-_{xy} = -\sigma^+_{xy}$, the second term on the right side of Eq. 3.21 would vanish but not the first term because $\alpha^\pm_{xx}$ have different signs and $\alpha^\pm_{xy}$ would be of the same sign. Generally, in semimetals or intrinsic semiconductors, the electrical conductivity is the sum of the conductivities due to each contribution separately and in the Seebeck, Hall and Righi-Leduc effects the electron and hole contributions tend to cancel each other. However, in the Nernst effect and the thermal conductivity, the hole and electron parts are additive which can lead to an enhancement of these effects. This mechanism is sometimes referred to as “ambipolar” or “bipolar”[43].

3.3.3 URu$_2$Si$_2$

This system is referred to as “heavy Fermion”. This name is basically given because the mass of charge carriers becomes “heavy”, leading to a variety of effects that will be discussed in more detail in chapter 8. Furthermore it is also a superconductor with a transition

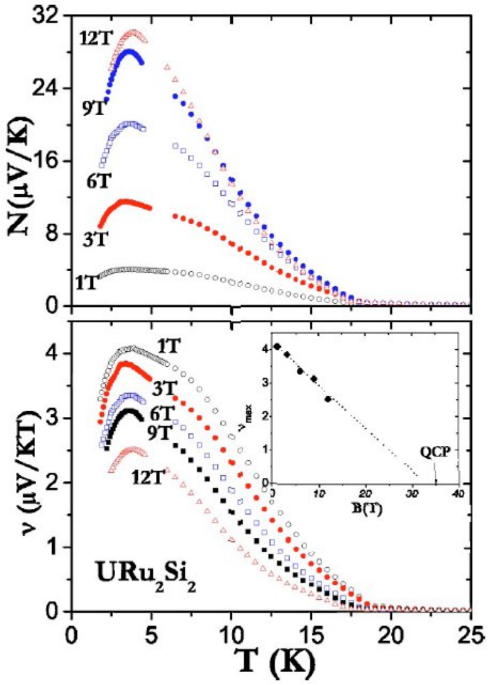

Figure 3.5: Nernst Effect in URu_2Si_2 for different magnetic fields. Upper panel shows the Nernst signal and the lower one the Nernst coefficient which is the signal divided by the magnetic field. The onset of the signal is coinciding with the onset of what is referred to as "hidden order". The inset in the lower panel shows the field dependence of the peak value of ν, from [11].

temperature as low as $T_c = 0.8\,\mathrm{K}$. Very recently, even a very narrow vortex-liquid phase could be detected in this compound [44]. In addition to these features, it hosts a mysterious phase which is referred to as "hidden order" (HO) and has a large Nernst signal. The onset temperature of both, the HO and the large Nernst effect coincide at about 17 K. The HO phase [45] exhibits an antiferromagnetic order with a very weak magnetic moment [46] which cannot account for the large amount of entropy that is lost at the transition [45] into this phase. For the various speculations about the origin of this effect, please refer to publications [47–52]. This hidden order state was found to host an exceptionally large Nernst effect [11]. In this phase the system undergoes a tenfold reduction in carrier density while the entropy per charge carrier is enhanced by a factor of three. As expressed in Eq. (3.19) the Nernst signal measures the energy dependence of the scattering time at the Fermi energy. The Fermi surface in this material is found to have four different orbits with the largest occupying less than 5% of the Brillouin zone [53]. A small Fermi energy in addition to a long scattering time are proposed to be a partial explanation for this huge Nernst signal although a reduced Fermi energy should enhance the Seebeck coefficient as well, which is not the case [11]. A closer look to this system and a related substance, UPt_2Si_2 will be given in chapter 8.

3.3.4 $CeCoIn_5$

Quite similar to URu_2Si_2, we again deal with a "heavy Fermion" that is superconducting at the low temperature of $T_c \approx 2.3$ [54]. Here, a large Nernst signal is found to emerge at

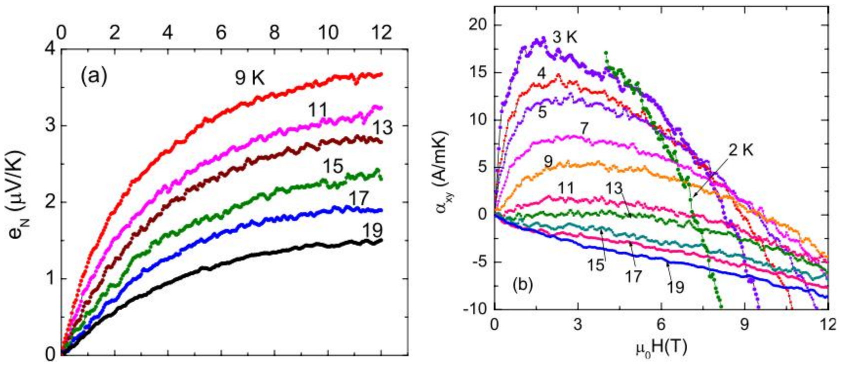

Figure 3.6: e_N and α_{xy} vs magnetic field in CeCoIn$_5$ for the same temperatures, showing that the differences in their field dependence is caused by the large contributions of charge and thermal Hall currents [57].

about 25 K with a magnitude drastically exceeding what is expected for a multiband Fermi-liquid metal. Explanations of these features remain highly speculative until now. Beyond the arguments of the energy dependence of the relaxation times as described above, antiferromagnetic fluctuations are also suspected of being able to produce an anomalous Nernst signal [55]. Other exotic explanations include the discussion of the influence of a quantum critical point on the off-diagonal conductivity tensor σ_{xy} [56]. The energy derivative at the Fermi energy of this tensor is related to the off-diagonal Peltier conductivity. This is expressed in Eq. (3.17). Then in turn, because the Nernst signal is intimately related to the off-diagonal Peltier conductivity such a proposed alteration of σ_{xy} might enhance the Nernst signal. These results were presented by Bel *et al.* in 2004 [11]. Three years later, Onose *et al.* again analyzed the Nernst signal of CeCoIn$_5$ [57]. Their results indicate that the measured Nernst signal has significant contributions due to a transverse thermopower which itself is caused by a transverse temperature gradient. After subtraction of this thermal Hall contribution, the enhanced Nernst signal is found to correlate with the thermopower anomalies in the precursor state of CeCoIn$_5$. Analyzing α_{xy} of Eq. (3.13) also reveals that the magnetic field dependence of e_N and α_{xy} is distinctly different, as can be compared in Fig. 3.6. The enhancement of α_{xy} below 15 K is interpreted as being concomitant with a steep decrease of the entropy current of the electrons towards T_c. Based on these revised experimental data, the original interpretation appears questionable.

3.3.5 Ferromagnetic materials

In ferromagnets, the Hall resistivity ρ_{xy} decomposes into the sum of the normal Hall resistivity, $\rho_{xy}^n = R_0 B$ and the anomalous part, $\rho_{xy}^a = R_a M$ that is proportional to the magnetization [58–60]. The anomalous Hall effect is furthermore distinguished between intrinsic mechanisms, such as the Berry phase that leads to dissipationless currents [61–63] and extrinsic contributions like skew scattering ($\rho_{xy} \propto \rho_{xx}$) [64] and side jump ($\rho_{xy} \propto \rho_{xx}^2$). The

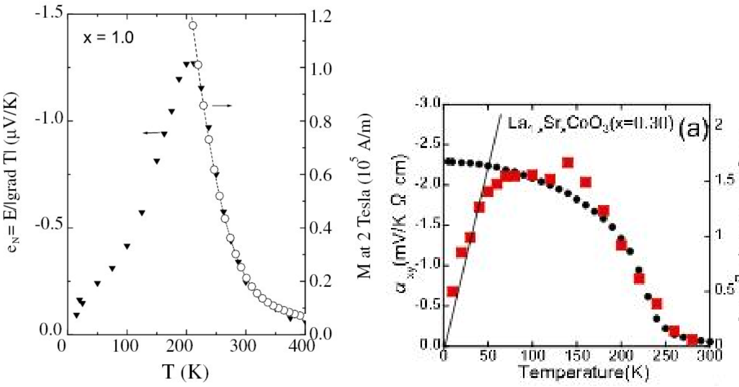

Figure 3.7: Left panel: Temperature dependence of the Nernst signal at 2 T for $CuCr_2Se_{4-x}Br_x$. Above T_C e_N scales with the paramagnetic magnetization $M(2\,T)$ [60]. Right panel: Temperature dependence of α_{xy} in $La_{0.7}Sr_{0.3}CoO_3$, scaling with the ferromagnetic magnetization until saturation and decreasing nearly linear in temperature for lower T [58].

latter describes small displacement of a charge carrier being scattered by an impurity [65]. Analogous to the Hall effect the Nernst signal can also be decomposed into terms that are separately proportional to the magnetic field and to the magnetization, $e_N = Q_0 B + Q_a M$ [60]. In $CuCr_2Se_{4-x}Br_x$ as shown in Fig. 3.7 (left panel) the Nernst signal is found to scale with $M(T)$ above the ferromagnetic transition, interpreted as a significant transverse electrical current caused by fluctuations in the paramagnetic magnetization. In the work of Miyasato *et al.* [58] the off-diagonal Peltier coefficient, α_{xy} is found to obey the Mott rule (Eq. (3.23)): α_{xy} increases just below the Curie temperature T_c proportionally to the magnetization and after the magnetization saturates it decreases linearly with T until it goes to zero which can be well understood using (Eq. (3.23)). Just below T_c the band structure changes due to the ferromagnetic transition, enhancing the factor $(\partial\sigma_{xy}(\epsilon)/\partial\epsilon)_{\epsilon_F}$. After the magnetization is saturated, the T-linear term in (Eq. (3.23)) becomes dominant in the change of α_{xy} as shown in Fig 3.3.5 (right panel).

$$\alpha_{xy} = \frac{\pi^2}{3}\frac{k_B^2 T}{e}\left[\frac{\partial\sigma_{xy}}{\partial\epsilon}\right]_{\epsilon_F}. \tag{3.23}$$

3.4 Nernst effect in the vortex liquid phase

The mentioning of this effect is a bit forestalled because it will cover the largest part of this work from the next chapter on. However, this small section completes the listing of different mechanisms that cause large Nernst effects. The basic Nernst signal in the mixed phase of high-temperature superconductors is given by the product of the finite transport entropy in the vortex core, s_Φ, and the flux flow resistivity ρ:

$$e_N \approx \rho\frac{s_\Phi}{\Phi_0} = e_N^s. \tag{3.24}$$

Φ_0 denotes the elementary flux quantum. A more detailed discussion of the vortex physics in a temperature gradient will be the content of section 4.2.5. Completing the above equation with the normal-state (metallic) Nernst signal derived in Eq. (3.16) yields the sum of both (assuming isothermal test conditions),

$$e_N = e_N^s + e_N^n = \rho \frac{s_\Phi}{\Phi_0} + \rho^n \alpha_{xy}^n - S \tan \Theta. \tag{3.25}$$

The aim of one part of this work is the systematic investigation of the evolution of the vortex Nernst signal crossing the superconducting transition temperature of the Ni-doped high-T_c compound $\mathrm{NdBa_2\{Cu_{1\text{-}y}Ni_y\}_3O_{7-\delta}}$. Therefore the separation of the superconducting Nernst signal from the normal state Nernst signal is crucial. Fortunately the normal-state signal in the investigated system turned out to be a quasiparticle signal that depends linearly on the applied magnetic field while the vortex Nernst signal is highly non-linear and therefore is easy to separate. An introduction into the physics of high-temperature superconductors, the appearance of vortices and the generation of voltages in the superconducting state will be given in the next chapter.

4 Superconductivity

4.1 Introduction

Superconductivity was discovered by Heike Kamerlingh Onnes in 1911 [66] when he found that the electrical resistivity of mercury suddenly vanished when the temperature fell below a certain critical value, $T_c = 4.2\,\mathrm{K}$. The next hallmark was the discovery of an effect observed by Meißner and Ochsenfeld [67] in 1933: A superconductor that is exposed to a magnetic field at a temperature $T > T_c$ and is then cooled down below its critical temperature is able to expel the applied magnetic field. This perfect diamagnetism or Meißner effect together with zero resistivity characterize superconductors.

In 1986, a new class of superconductors were discovered by J. Bednorz and K. Müller [1]. These substances are ceramic compounds with critical temperatures (T_c) reaching as high as 138 K $(Hg_{0.8}Tl_{0.2})Ba_2Ca_2Cu_3O_{8.33}$ up to now. This property truly entitles these compounds with the name "high-T_c's". A common structural feature of these substances are the copper-oxide (CuO) planes. It is believed that most of the physical properties including superconductivity are determined by mobile charge carriers that move within these planes. Since the CuO planes are separated by various other planes, such as i.e. LaO or BaO, most of theses structures can be addressed to as quasi-two-dimensional. These additional planes play structural roles and provide screening and doping environments. The copper-oxide plane is a square lattice with copper ions being placed at the corners and oxygen ions placed at the center of the bonds that connect the copper ions. Because of those planes, the high-T_c's are also called cuprate superconductors. The research in the field of the high-T_c's is mostly driven by the desire to unravel the origin of this special kind of superconductivity.

In this chapter, a brief introduction into the different types of superconductors, their phenomenology and some theories on superconductivity will be given with focus on the physics that is needed for the understanding of the thermomagnetic effects in high-T_c's [17, 68–73].

4.1.1 Theoretical background

London theory

The London theory quantitatively describes the behavior of shielding currents and the penetration depth of magnetic fields in surface sheets of superconductors. Since the exclusion of the magnetic field cannot happen discontinuously (implicating an infinite current density), the field strength has to fall off within a certain typical length scale,

$$\lambda_L^2 = \frac{m_s}{\mu_0 n_s e_s^2}, \tag{4.1}$$

that is called the London penetration depth. m_s, n_s and e_s relate to the mass, the density and the charge of Cooper-pairs [2], respectively. λ_L is derived from the London equations,

$$\frac{d\mathbf{j_s}}{dt} = \frac{n_s e_s^2}{m_s}\mathbf{E} \quad \text{and} \quad \nabla \times \mathbf{j_s} + \frac{n_s e_s^2}{m_s}\mathbf{B} = 0. \tag{4.2}$$

Ginzburg-Landau theory

The Ginzburg-Landau (GL) theory is based on Landau's theory of second-order phase transitions. The superconducting order parameter is defined as the wave function of the Cooper-pairs, $\Psi(\mathbf{r}) = |\Psi(\mathbf{r})|e^{i\phi}$. The square of its absolute value is connected to the Cooper-pair density, $|\Psi(\mathbf{r})|^2 \propto n_s$. This density cannot discontinuously jump to zero at the surface of superconductors or at junctions between superconducting (s) and normal (n) conducting materials. To be descriptive, the length scale in which n_s is allowed to vary spatially has to be at least the diameter of one Cooper-pair. This characterizing length scale is given by the coherence length, ξ. The characteristic length scales λ_L and ξ are visualized in Fig. 4.1. Within mean-field theory, they obey the same temperature dependence in the vicinity of T_c, $\xi(T), \lambda_L(T) \propto (1-t)^{-1/2}$ with $t = T/T_c$, so that it is reasonable to define the Ginzburg-Landau-parameter,

$$\kappa = \frac{\lambda_L(T)}{\xi(T)}. \tag{4.3}$$

Typical values for a pure superconductor are in the range of $\lambda_L \approx 500\,\text{Å}$ and $\xi \approx 3000\,\text{Å}$. Assuming n_s is reduced to zero within a length of $\xi \approx 3000\,\text{Å}$, the loss of condensation energy of the superconducting phase is of the order of $B_{cth}^2 \cdot \xi$ per unit of the s-n interface area[1]. This loss on the other hand is a positive contribution to the surface energy. This surface energy is reduced again by $B_{cth}^2 \cdot \lambda_L$, because the magnetic field penetrates approximately 500 Å into the superconductor. So, because of $\xi > \lambda_L$ it would require additional energy to build up phase boundaries between superconducting and normal conducting zones, see Fig. 4.1.

The exact condition defining this so-called type-I superconductors is given by

$$\kappa > \frac{1}{\sqrt{2}} \qquad \text{type-I}, \tag{4.4}$$

characterizing materials that tend to expel magnetic fields completely. In case of $\xi < \lambda_L$, the superconductor tries to maximize the areas between superconducting and normal state

---

[1] B_{cth} is the thermodynamic critical field where the free enthalpy of the normal and the superconducting states are of the same value.

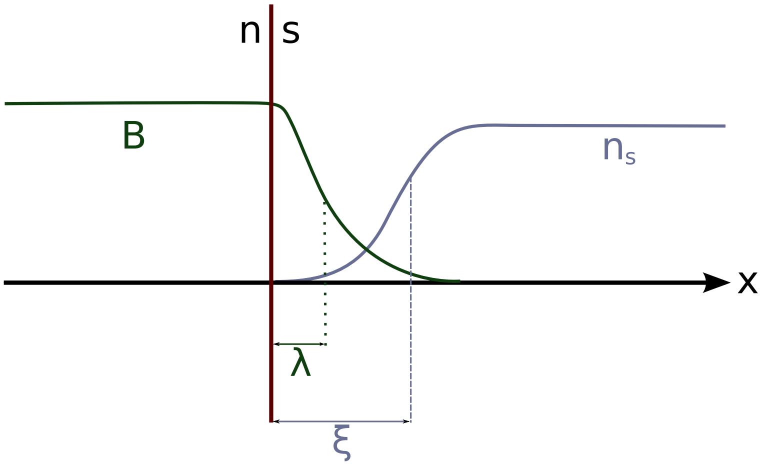

Figure 4.1: Junction of normal (n) and superconducting material (s). The magnetic field falls off on a typical length scale λ when entering the superconductor. The Cooper-pair density characteristically decreases on a length scale ξ when approaching the normal conducting region.

phases if a large enough magnetic field is applied. In this case, magnetic flux in units of elementary flux quanta $\Phi_0 = h/2e$ penetrates the bulk of the superconductor,

$$\kappa < \frac{1}{\sqrt{2}} \qquad \text{type-II.} \tag{4.5}$$

Such a flux line is encircled by a superconducting ring current of Cooper-pairs and often referred to as “vortex”. This phase is called mixed state or “Shubnikov” phase. The condition $\xi < \lambda$ is easy to fulfill by doping metallic impurities into a type-I superconductor. Doing so effects a decrease of the mean free path l which in turn makes the penetration length λ_L larger. Additionally, $\xi \propto \sqrt{l}$. Two distinct magnetic field regions now characterize the superconducting material. From $B = 0$ to $B = B_{c1}$ type-II superconductors expel the magnetic field just like a perfect diamagnet would do. B_{c1} is given by $B_{c1} \approx \Phi_0/(\pi\lambda_L)^2$. From B_{c1} to $B_{c2} \approx \Phi_0/(\pi\xi)^2$, magnetic flux tubes penetrate the bulk of the superconductor in units of Φ_0. At B_{c2} the superconductivity breaks down which can be visualized as follows: A flux tube covers the normal conducting area of $\approx \pi\xi^2$. The externally applied magnetic field reflects itself in the sum of single flux tubes that penetrate the sample, $B = n\Phi_0$. If the flux tube density becomes so large, that the sum of their normal conducting cross section covers the whole sample, no superconducting areas are left. This behavior is depicted in Fig. 4.2. Furthermore, the flux lines in the mixed state are repelling each other. It was theoretically predicted by Abrikosov and later verified experimentally that they tend to arrange themselves in a regular triangular lattice, called Abrikosov lattice [74]. Such an arrangement is shown in Fig. 4.3 (b) and (c) while subfigure (a) depicts the excitation spectrum of one vortex together with its magnetic field profile (governed by λ) and its spatial variation of the superconducting density (governed by ξ). The energy gap is denoted by Δ_∞.

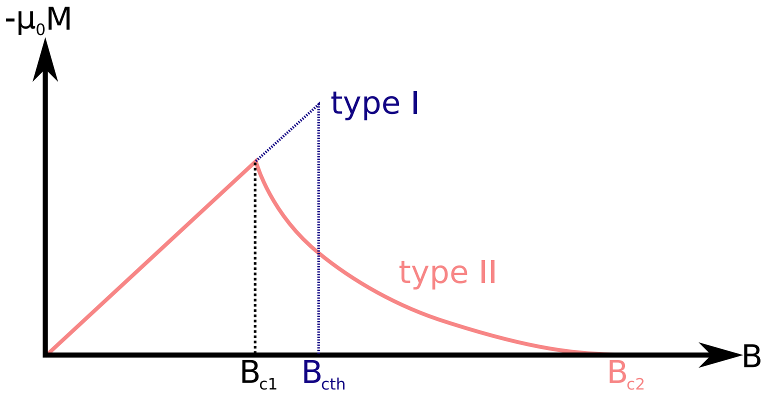

Figure 4.2: Negative magnetization of type-I (dashed line) and type-II superconductors (solid line). B_{c1} and B_{c2} denote the lower and the upper critical fields, respectively. B_{cth} is the thermodynamic critical field where the free enthalpy of the normal and the superconducting states are of the same value.

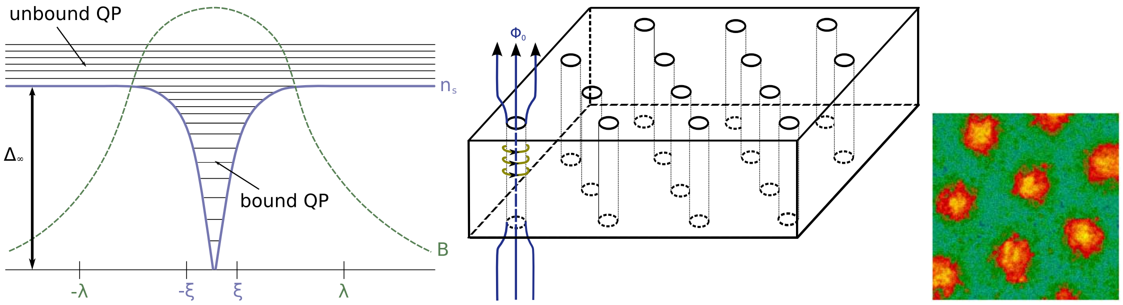

(a) One vortex

(b) Vortex lattice

(c) STM picture of MgB_2

Figure 4.3: Illustration of magnetic flux penetrating the bulk of a type-II superconductor. (a) Scheme of one vortex of diameter 2ξ: the normal conducting core carries bound quasiparticles (QT) while outside the core live excitations from the superconducting ground state that are unbound quasiparticles (at finite temperature). n_s and the magnetic field profile are schematically shown by the continuous and dashed lines, respectively. (b) depicts the arrangement of a vortex lattice in a typical type-II material. (c) shows the vortex lattice in MgB_2 as observed by STM [75].

BCS theory

A microscopic theory of superconductivity has been proposed by Bardeen, Cooper and Schrieffer (BCS)[76], stating that even a week attractive interaction between electrons causes the formation of bound pairs with equal momentum and opposite spin. Such an interaction could be mediated via lattice displacements of the positive charged lattice ions as represented in a simplified picture: A first electron moving through the lattice distorts the surrounding ions while the second "feels" this altered electrical potential and is thereby effectively attracted to the first electron. Such a Cooper-pair has a binding energy of

$$\Delta(T=0) = 2\hbar\omega_D e^{\frac{-2}{D(\epsilon_F)U}}, \tag{4.6}$$

with U expressing the coupling between electrons and phonons and $D(\epsilon_F)$ the density of states at the Fermi energy. At $T = 0\,\mathrm{K}$, all electrons are bound to Cooper-pairs of the same quantum state. The first excited state above this condensate is occupied by quasiparticles of the energy $E_{gap} = 2\Delta$. Increasing the temperature leads to a gradual excitation of quasiparticles until at T_c with $\Delta(T_c) = 0$ or $n_s(T_c) = 0$ superconductivity breaks down. BCS theory predicts in case of weak electron-phonon coupling an energy gap of size $E_{gap}(0) = 2\Delta(0) = 3.52k_BT_c$ and a temperature dependence (in the vicinity of T_c) of

$$\frac{\Delta(T)}{\Delta(0)} = \sqrt{1-\frac{T}{T_c}}. \tag{4.7}$$

4.1.2 Pinned and depinned vortices

Starting from the development of equilibrium theory for the behavior of type-II superconductors by Abrikosov [74] in magnetic fields, two categories of type-II superconductors can be distinguished. The first category comprises the type-II superconductors described so far, e.g. impurity doped type-I superconductors with $T_c < 26\,\mathrm{K}$. Their typical $B(T)$ phase diagram is shown in Fig. 4.4(a). The vortex lattice above B_{c1} spontaneously breaks two symmetries, namely phase coherence in the pairing field and translational symmetry due to the development of long range order of the vortex lattice. One flux tube has an energy per unit length of $\epsilon = B_{c1}\Phi_0/\mu_0$. A flux tube can lower its energy by going through a normal state region within the bulk of the superconductor e.g. caused by metallic impurities just because the superconducting length of the flux tube is reduced. Thus, these areas tend to trap the flux line, a phenomenon called "pinning". Consequently, such areas of static disorder will contribute to a finite pinning force density, f_p which is the pinning force per unit length of the flux line. f_p counteracts driving forces caused by application of currents or temperature gradients. Thermal fluctuations cause disorder that affect the phase diagram as well as the dynamic properties [77, 78]. These fluctuations tend to smooth the pinning potential which leads to thermal depinning of the flux line and thereby resulting in so called flux creep (thermally activated flux jumps from one pinning center to another). Quantitatively, the strength of thermal fluctuations may be expressed by the Ginzburg

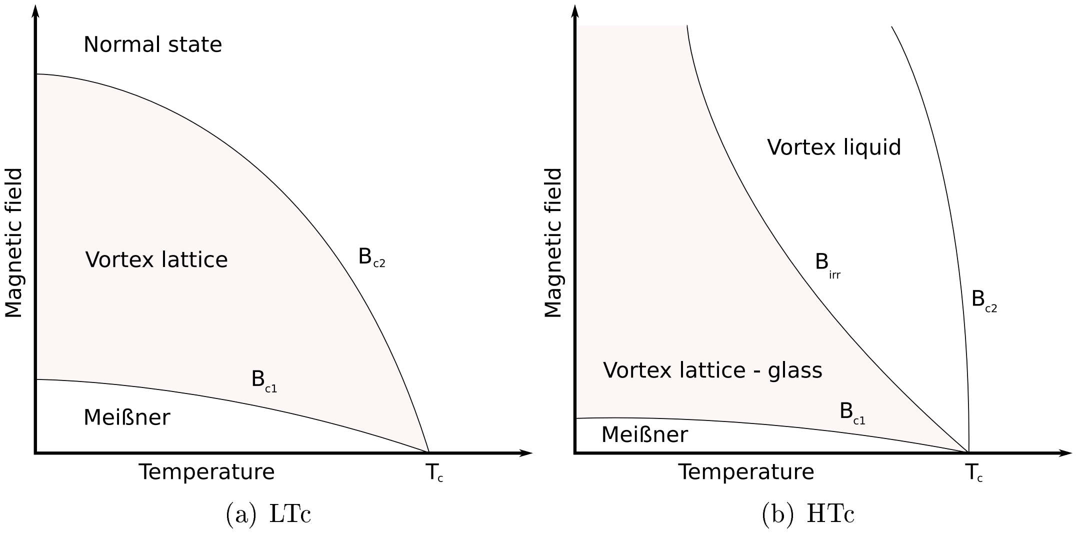

(a) LTc (b) HTc

Figure 4.4: Schematic phase diagram of a type II LTc (a) and that of a type II HTc (b). B_{c1} and B_{c2} are the lower and the upper critical fields, respectively. B_{irr} in (b) is the irreversibility line, or melting line of the vortex lattice. Adapted from [71].

number, $G = [2\mu_0 k_B T_c/(B_{cth}^2 \xi_\|^2 \xi_\perp)]^2/2$ measuring the relative size of the transition temperature and condensation energy within a coherence volume. The phenomenological phase diagram showing the modifications for a high-T_c is presented in Fig. 4.4(b). Here T_c and the Landau penetration depth are large, while the coherence length is very small. Therefore, these materials are governed by weaker pinning and significant thermal fluctuations, $G \approx 10^{-2}$ compared to $G \approx 10^{-8}$ in low-T_c superconductors. The experimental relevance is, that for type-II superconductors with low T_c's, vortices are mostly pinned in the whole temperature and magnetic field range accessible. In high-T_c's however, there is a distinct line separating reversible magnetic behavior and irreversible magnetic behavior. This is the irreversibility line $B_{irr}(T)$. Above this line, vortices are free to move, resulting in reversible magnetization curves. The irreversibility line is also called depinning or melting line and is shown exemplarily for two samples of $\mathrm{NdBa_2\{Cu_{1\text{-}y}Ni_y\}_3O_{7-\delta}}$ (0,3% Ni) in Fig. 4.5. It represents the field strength and thereby the flux density which is necessary to overcome pinning forces at fixed temperatures, in this case derived from Nernst effect measurements.

The vortex lattice melting from a low temperature ordered phase into a high temperature vortex liquid is believed to be a thermodynamic phase transition [79]. Taking into account the pinning disorder, a transition from the vortex-liquid into a vortex glass phase is also possible, as proposed by Fischer *et al.* [80]. The consequence is that vortices at low temperatures are frozen into random configurations.

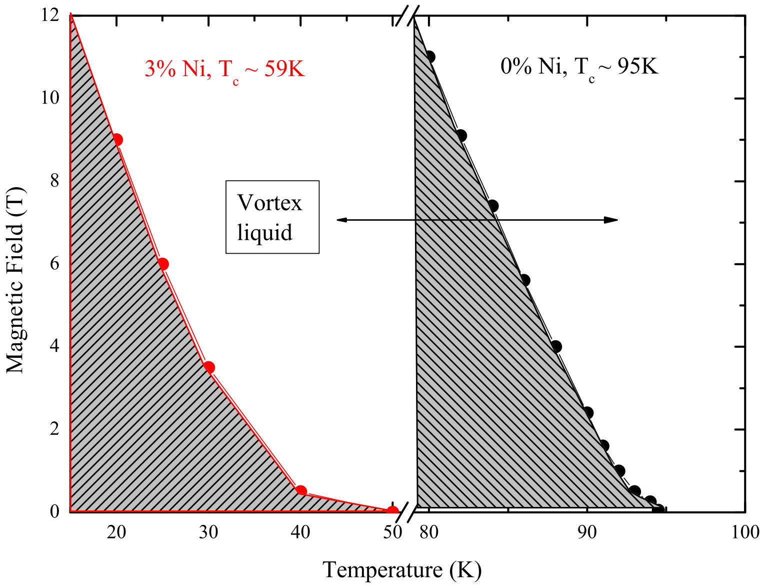

Figure 4.5: Vortex melting lines for two optimally doped samples of $\mathrm{NdBa_2\{Cu_{1\text{-}y}Ni_y\}_3O_{7-\delta}}$ with Ni contents of 0% and 3%. Data is extracted from measurements of the Nernst signal. For given temperatures (only below the superconducting transition temperature), a certain field strength has to be passed to generate voltages at the transverse contacts. This is then referred to as "pinning field" or "melting field" $B_m(T)$. The so extracted melting lines separate the vortex lattice from the vortex liquid phase.

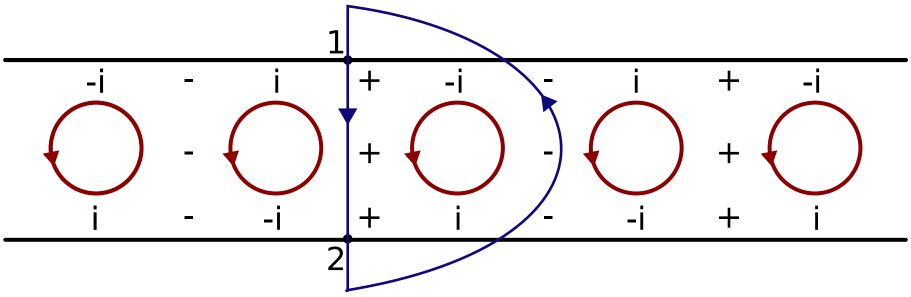

Figure 4.6: Voltage generation by vortex movement - scheme. One circle around a flux line collects a phase of 2π which is symbolized here by following the path along (i,-,-i,+). Moving vortices passing the reference points 1 and 2 produce a transverse electric field because of time dependent phase slip processes, resulting in $\mathbf{E} = \mathbf{v} \times \mathbf{B}$.

4.2 Vortex dynamics

4.2.1 Voltages in high-T$_c$ materials

As mentioned before, superconductors are mainly characterized by two basic features: perfect diamagnetism and a vanishing resistivity. The latter makes sure that no voltages can be developed because they will be immediately bypassed by a superconducting current. Nevertheless, resistive behavior can be observed in the mixed phase, once the melting line has been overcome. All following discussion will be based on the assumption that the magnetic field is directed perpendicular to the CuO planes. Because only within these planes supercurrents are able to encircle the magnetic field. A configuration with the magnetic field directed parallel to the planes would result in a scenario where charge carriers tunnel from plane to plane in c direction, thereby creating a vortex-like structure referred to as Josephson-vortex. The vortices oriented perpendicular to the planes can easily be forced to move through the sample by either applying a transport current or a temperature gradient perpendicular to the applied magnetic field. A moving vortex then produces a voltage perpendicular to its moving direction. Since a single flux line is surrounded by a supercurrent of Cooper-pairs, the continuity of their wave functions requires that the phase returns to itself modulo 2π. Because of this phase singularity at each vortex core, the motion of vortices produces a phase-slippage voltage [81], U, which can be understood by the Josephson equation:

$$\frac{\partial \Delta\phi}{\partial t} = \frac{2eU}{\hbar} \qquad \text{with} \qquad \Delta\phi = \phi_1 - \phi_2. \tag{4.8}$$

$\Delta\phi$ denotes the phase difference between two points 1 and 2 (Fig. 4.6).

As the flux lines cross a virtual line between 1 and 2, the average phase differences can be expressed by

$$\overline{\frac{\partial \Delta\Phi}{\partial t}} = 2\pi b v n, \tag{4.9}$$

with b the distance between the two points, v the vortex velocity and n the vortex density, controlled by the applied magnetic field:

$$n = \frac{B}{\Phi_0} \qquad \text{with} \qquad \Phi_0 = \frac{h}{2e}. \tag{4.10}$$

The consequence is an electric field perpendicular to the vortex motion and the magnetic field:

$$\mid \overline{E_y} \mid = v_x B_z \qquad \text{or} \qquad \mathbf{E} = \mathbf{v} \times \mathbf{B}. \tag{4.11}$$

4.2.2 Some forces on vortices

In this section the basic ideas of moving vortices will be introduced. The causes for vortex motion will be limited to two cases, namely vortex motion induced by a transport current and by an applied temperature gradient. Other mechanisms to make vortices move with respect to the lattice would e.g. be a timely modulation of the applied magnetic field and others [68, 70, 73, 82]. Forces will be given in notation of forces per unit length, $\mathbf{f} = \mathbf{F}/l$. The vector $\mathbf{z}$ denotes the unit vector in z direction which is the direction of the magnetic flux in the vortex core. The discussion is based on a “two fluid” scenario in which two kinds of charged particles are assumed to be spread within the bulk of the sample: the superconducting Cooper-pairs with density n_s and velocity $\mathbf{v_s}$ and the normal conducting quasiparticles with density n_n and velocity $\mathbf{v_n}$.

Magnus force

Here the concept of the Magnus force that arises due to a moving vortex with respect to the surrounding superconducting liquid is discussed. The force can be derived as it is long known in classical hydrodynamics and finds its most prominent example in the lift force that the flow of air produces on a wing of a plane [83, 84]. The implications of this transverse force on moving vortices in a Bose superfluid will be expatiated below. The Magnus force on a moving vortex first appeared in the work of Nozières and Vinen [85] and is normal to the relative vortex velocity. It is therefore a reactive force and produces no work [84]. Assuming a vortex with uniform velocity $\mathbf{v}_\Phi$ and a current of the superfluid far away from the vortex core, $\mathbf{v}_s$. Together with the flux vector $\mathbf{z}$ which is directed parallel to the magnetic field, the magnus force can be written as

$$\mathbf{f}_M = \frac{n_s h}{2}(\mathbf{v}_\Phi - \mathbf{v}_s) \times \mathbf{z}, \tag{4.12}$$

where n_s denotes the density of the superconducting fluid.

The nomenclature for the Magnus force often differs in literature, i.e. Eq. (4.12) can also be written as $\mathbf{f}_M = \frac{n_s h}{2}\mathbf{v}_\Phi \times \mathbf{z} - \frac{n_s h}{2}\mathbf{v}_s \times \mathbf{z}$. The first term on the right side resembles the part of the force that is directed perpendicular to the vortex movement. This term alone is sometimes also referred to as Magnus force [73, 86] or effective Magnus force [84]. The second term on the right side exerts a force that is directed perpendicular to the velocity of the Cooper-pairs. In the following this separation of the Magnus force will sometimes be used and the separate contributions will be denoted by $\mathbf{f_L}$ and $\tilde{\mathbf{f}}_\mathbf{M}$ for the Lorentz and the effective Magnus force, respectively.

Thermal force

A vortex carries entropy in its normal conducting core. This entropy per unit length is denoted by s_Φ and leads to a force that acts on the vortex if a temperature gradient is applied,

$$\mathbf{f_{th}} = -s_\Phi \nabla T. \tag{4.13}$$

This force obviously is directed along the temperature gradient and not dependent on the vortex velocity.

4.2.3 Vortex motion in a transport current

Here the case of a type-II superconductor in the mixed state and under an applied current parallel to the CuO planes will be discussed. Such a measurement of the resistive voltage is shown as a function of current for several magnetic fields in Fig. 4.8. Depending on the magnetic field, a certain threshold of the current is necessary to overcome pinning forces. By further increasing the current, the slope of the curves, dV/dI also increases until the linear flux-flow regime with constant dV/dI is attained. An overview of the early development of the phenomenological models of vortex dynamics can be found in [87–93]. In the following sections, the development of more recent theories will be focused on. Starting with the force balance equation as proposed in [73]

$$\frac{n_s h}{2}(\mathbf{v}_\Phi - \mathbf{v}_s) \times \mathbf{z} - \frac{h}{2} D \mathbf{v}_\Phi - \mathbf{f}_p = 0, \tag{4.14}$$

the Magnus force is balanced by a damping force with damping coefficient D and the pinning force $\mathbf{f}_p$. The size of D, which is determined by the physical regime, is addressed in more detail later in this section. For simplicity, parts of forces that may arise due to vortex interaction with the unbound quasiparticles (QP's) outside the core are neglected here. A more detailed picture is discussed later, after the excitation spectrum in vortices has been introduced (section 4.2.4).

Resistivity and Hall effect

Based on Eq. 4.14, one can easily see what happens if the vortex is allowed to move in an inviscid surrounding ($D = 0$) and neglecting pinning forces ($f_p = 0$):

$$\frac{n_s h}{2}(\mathbf{v}_\Phi - \mathbf{v}_s) \times \mathbf{z} = 0 \rightarrow \mathbf{v}_\Phi = \mathbf{v}_s. \tag{4.15}$$

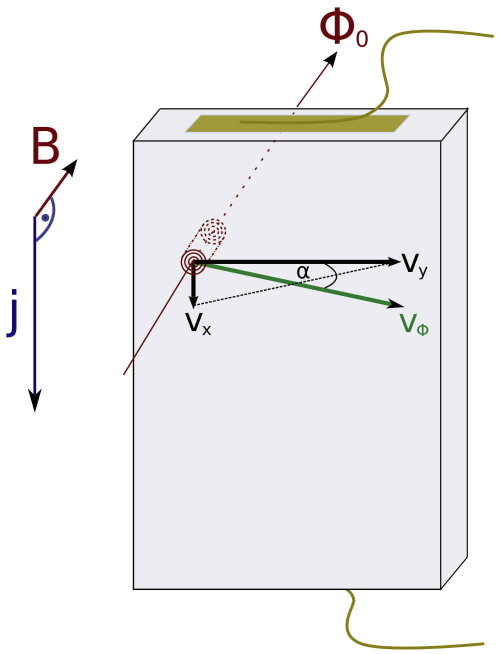

Figure 4.7: Scheme of the direction of vortex movement under the influence of a transport current j. This current is injected through the symbolized electrical contacts and the wiring on top and bottom of the sample. Φ_0 is the amount of magnetic field that penetrates one vortex. The Hall angle is given by $\tan\alpha = v_x/v_y$ and determines the direction the moving vortex, v_Φ. As determined from experiment, its is known that the vortex moves nearly at right angles with respect to the transport current. Typically values of i.e $\tan\alpha \approx 10^{-3}$ are veryfied by several groups [94–96].

A steady state is reached, when the vortex just moves with the applied supercurrent. The lift force on a plane can help visualizing the situation: When the engines, the gravity and friction forces would be turned off, the plane would be left to flow in the direction of the wind. If the vortex is first held by an imaginary force and is then suddenly released, it would have an initial impulse transverse to the applied current but then gains more and more curvature until it will finally move with the current. This scenario would result only in a measurable Hall voltage. The ratio of the Hall resistivity (ρ_{xy}) and the resistivity (ρ_{xx}) determines the electrical Hall angle and provides an experimental determination for the direction of vortex movement,

$$\tan\alpha = \rho_{xy}/\rho_{xx}. \tag{4.16}$$

Assuming now that the damping coefficient is non-zero. Then the Lorentz force acts on the vortex in a direction transverse to the superconducting charge current. The effective Magnus force tends to move the vortex perpendicular to its own direction of movement. The sum of the velocity dependent parts of the forces, namely the damping force and the effective Magnus force are balanced by the Lorentz force. If the force that acts perpendicular to the vortex velocity is of comparable magnitude to the Lorentz force, the vortex would be driven at angles of $\approx 45°$. But, many experiments determine this Hall angle to be very small, i.e. $\tan\alpha \approx 10^{-3}$ [94–96] in the reversible regime of high-T$_c$'s ($T < T_c$). This means that the flux flow resistivity is larger than the flux flow Hall effect by a factor $\sim 10^3$. Thus, the vortex moves nearly perpendicular to the applied current, a situation that is sketched in Fig. 4.7. This implicates that the effective Magnus force must be subject to a severe attenuation.

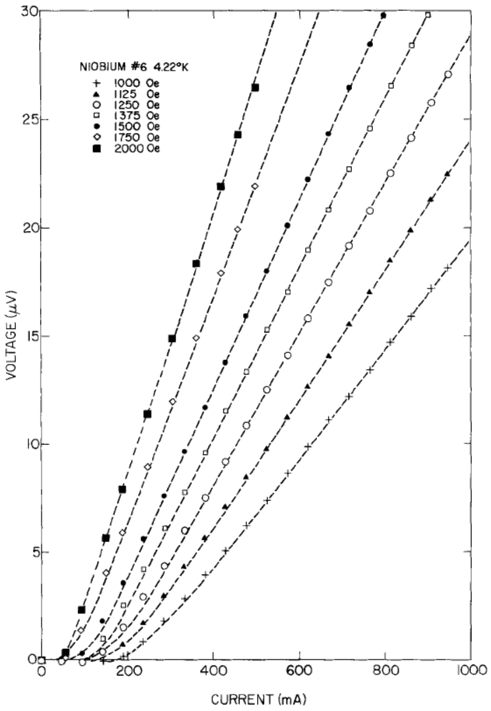

Figure 4.8: Resistive Voltage in Niobium. The superconductor is in a state where flux movement leads to dissipation of energy. Shown here is the current dependent voltage in several magnetic fields. A certain current threshold has to be exceeded in order to depin vortices [97].

Now let me postpone this issue until the origin of the Peltier effect is discussed. It will turn out that implementing a new force on the vortex will sufficiently explain the small Hall angle and the Peltier effect.

Ettingshausen and Peltier effect

The core of a flux line is not superconducting. The entropy density within the vortex core is thereby higher than in the surrounding superconducting phase. The entropy carried by a moving vortex (per unit length) is denoted by s_Φ and a moving vortex is then connected with a heat current density $\mathbf{j}_h = nTs_\Phi \mathbf{v}_\Phi$, with n being the density of flux lines, T the temperature and $\mathbf{v}_\Phi$ the vectorial velocity of the vortex [73, 98, 99]. Separating this expression into components parallel and perpendicular to the transport current (x- and y-directions), we get

$$\mathbf{j}_h^y = nTs_\Phi v_y = -\kappa_{yy}\frac{\partial T}{\partial y} \quad \text{and} \tag{4.17}$$

$$\mathbf{j}_h^x = nTs_\Phi v_x = -\kappa_{xx}\frac{\partial T}{\partial x}, \tag{4.18}$$

with κ being the heat conductivity. Together with Eq. (4.11) we derive for the temperature gradient in transverse direction that is caused by the entropy carried by the vortices (see also Fig. 4.9):

$$\left| \frac{\partial T}{\partial y} \right| = \frac{T}{\kappa_{yy}} \frac{s_\Phi}{\Phi} \left| \frac{\partial V_x}{\partial x} \right| . \tag{4.19}$$

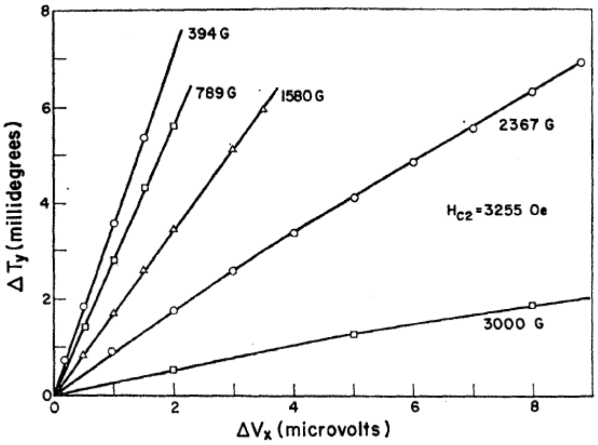

Figure 4.9: Applying a current in x direction of the sample sets up an electric field which in turn leads to the development of a transverse temperature gradient. This effect is referred to as Ettingshausen effect. Shown here is the transverse temperature gradient vs. longitudinal voltage for a type-II alloy of In +at.%Pb, taken from [100].

The same expression applies for the temperature gradient caused by the vortex entropy in longitudinal direction. This would mean $v_x = v_y$. However, since we know already that vortices move almost perpendicular to the applied current, the ratio of transverse to longitudinal temperature gradients due to the vortex contribution alone is only of order $\sim 10^3$. This consideration would lead to a very small expected Peltier effect. It turns out, however, that a considerably large Peltier coefficient can be resolved for $Bi_{1.76}Pb_{0.24}Sr_2Ca_2Cu_3O_\delta$ far below T_c, with $T_c \approx 110\,\mathrm{K}$. Measurements are depicted in Fig. 4.10, in magnetic fields ranging from 0 (blue) to 5T (red). This Peltier effect is too large by a factor 10^3 for being caused by the vortex carried entropy. This means that the measured longitudinal and transverse temperature gradients are of comparable magnitude but definitely not of the same origin.

Now let me briefly summarize the situation in a current driven vortex motion as determined from the experiments described so far: $U_x \gg U_y$ because $v_{\Phi,y} \gg v_{\Phi,x}$. Additionally, we have $\nabla_x T \approx \nabla_y T$, this time not *because*, but *although* $v_{\Phi,y} \gg v_{\Phi,x}$. This rises the question: How can the velocity dependent part of the Magnus force be almost cancelled while a substantial heat current flow along the applied transport current persists?

The most feasible scenario accounting for this ostensible contradiction includes the introduction of a new force called "spectral flow" force. This force arises from the "spectral flow" effect that will be introduced in somewhat more detail now.

4.2.4 Spectral flow

Before details are discussed, i will forestall a more qualitative understanding of this effect: The spectral flow can be thought of as a flow of quasiparticles (QP) that are able to leave the vortex core at right angles with respect to the vortex velocity. Since these QP carry

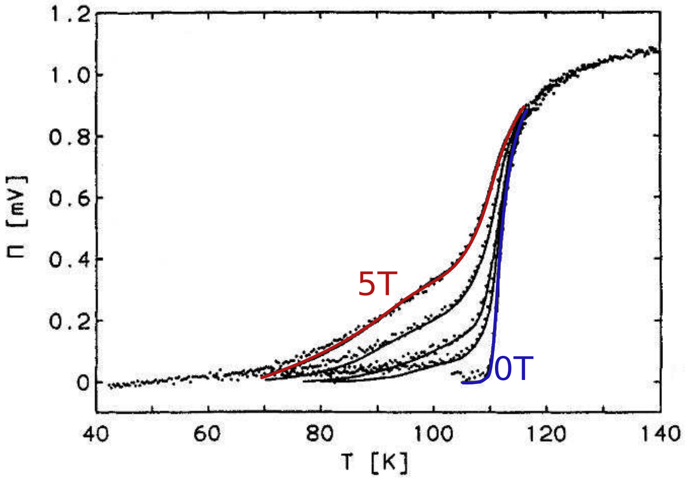

Figure 4.10: Peltier effect in $Bi_{1.76}Pb_{0.24}Sr_2Ca_2Cu_3O_\delta$ in magnetic fields $B = 0, 0.5, 1, 2.5, 5\,T$. The measured Peltier effect is indicated by the scattered black data points. Continuous lines are the calculated Peltier coefficients as expected from the Kelvin relation, $TS = \Pi$. S is the termopower, also determined from experiment. Taken from [101].

momentum, a force ($\mathbf{f_S}$) is exerted back on the vortex. If the $\mathbf{v_\Phi}$-dependent parts of $\mathbf{f_S}$ and the Magnus force, $\mathbf{f_M}$, are of opposite sign and nearly equal in magnitude, it becomes intuitively clear that vortices move in right angles with respect to the applied supercurrent. This immediately explains the small Hall angle. Furthermore, the heat carrying QP, that leave the vortex core, are directed parallel to the supercurrent. This directly accounts for the large Peltier coefficient. The spectral flow, so to say, kills two birds with one stone.

For a more detailed understanding of the origin of this new force, the excitation spectrum in the presence of vortices has to be discussed first.

Excitation spectrum in the presence of vortices

Since the superfluid condensate does not carry heat, it is necessary to discuss the excitation spectrum of a superconductor in the presence of vortices. Following the discussion on an s-wave superconductor, this section will give an overview of the origin of forces that arise from specific types of the excitation spectra in vortex cores. For the mathematical derivation and formula notation, please refer to publications [82, 102–104]. Implications on forces in d-wave superconductors, such as the high-T_c's are discussed in [105, 106]. The increase of the order parameter from the center of a vortex core to its equilibrium value Δ_∞ is isotropic for s-wave superconductors. Typical distances are of the order of the coherence length, ξ. Two kinds of excitations form the whole spectrum. Bound excitations which can be thought of as standing waves set up by Andreev reflected QP's [102, 107], localized at the vortex core and unbound excitations, delocalized throughout the bulk of the sample. The low-lying bound states are Landau levels that can be characterized by a discrete radial

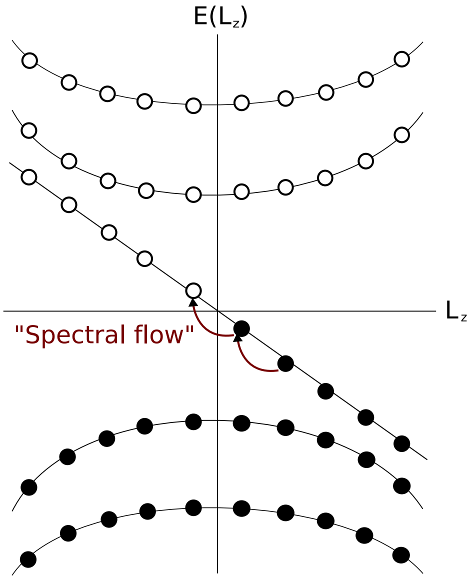

Figure 4.11: Spectrum of particles in the core of vortices in superconductors. The linear crossing from negative to positive energies is referred to as “anomalous chiral branch”, allowing particles to leave the core at right angles with respect to the vortex velocity. After leaving the core, interactions with the normal fluid of the bulk are possible and therefore an additional force is exerted back on the vortex. Adapted from [103].

quantum number n and an angular momentum L_z. This spectrum is shown in Fig. 4.11, indicating the bound states with solid circles and the unbound ones with open symbols. A special feature is the so-called anomalous chiral branch, indicated in Fig. 4.11 as the linear crossing of the L_z axis, which allows a transfer of particles from negative to positive energy levels of the spectrum, or in other words QP's are allowed to leave the core at right angles with respect to the vortex velocity. The interlevel distance of the bound states is given by $\hbar\omega_0 \approx \Delta_\infty/E_F$ which is usually small because $\Delta_\infty \ll E_F$ with E_F being the Fermi energy. A spectral flow is allowed if this spectrum may be regarded as continuous. To sufficiently fulfill this condition, the level widths have to be broadened ($\hbar/\tau$), i.e. due to scattering of core excitations by free excitations outside the core. In fact, it is reasonable to distinguish two limits, the collisionless ($\omega_0\tau \gg 1$) and the hydrodynamic ($\omega_0\tau \ll 1$) limit. According to the discussion above, spectral flow occurs in the hydrodynamic limit. Entering the collisionless limit is hard to acquire from the experimentalist's point of view. First, very low temperatures are required. This leaves only a few unbound QP excitations outside the core. This channel of scattering is therefore attenuated. Additionally, very clean samples are helpful to further enhance the scattering time τ until $\omega_0\tau \gg 1$ is fulfilled. These requirements are not often met in the laboratory, so that one can say that measurements are typically carried out in the hydrodynamic limit. This automatically implicates the existance of the spectral flow in its full strength.

Forces in a transport current

The force resulting from this spectral flow can be formulated as

$$\mathbf{f_S} = -\frac{h}{2}C(\mathbf{v}_\Phi - \mathbf{v}_n) \times \mathbf{z}, \tag{4.20}$$

with v_n being the velocity of the normal fluid outside the core. C is a parameter that determines the regime of the vortex dynamics [108]:

$$\frac{C}{n} = 1 - \frac{\omega_0^2\tau^2}{1+\omega_0^2\tau^2}\tanh\left(\frac{\Delta(T)}{2k_BT}\right), \tag{4.21}$$

with $n = n_s + n_n$ being the sum of the superconducting and normal conducting densities and $\mathbf{v}_n$ denoting the velocity of the normal fluid. $\Delta(T)$ is the superconducting energy gap. As already mentioned, the spectral flow is fully active in the hydrodynamic limit, because $\omega_0\tau \ll 1$ leads to $C/n \approx 1$. Setting $\omega_0\tau \gg 1$, as in the collisionless limit, we get $C/n \to 0$ for $T \to 0$ and the spectral flow force vanishes.

The acting forces on the vortex are:

$$\mathbf{f_M} = \frac{n_s h}{2}(\mathbf{v}_\Phi - \mathbf{v}_s) \times \mathbf{z} \tag{4.22}$$

$$\mathbf{f_I} = \frac{n_n h}{2}(\mathbf{v}_\Phi - \mathbf{v}_n) \times \mathbf{z} \tag{4.23}$$

$$\mathbf{f_S} = -\frac{h}{2}C(\mathbf{v}_\Phi - \mathbf{v}_n) \times \mathbf{z} \tag{4.24}$$

$$\mathbf{f_D} = \frac{h}{2}D(\mathbf{v}_n - \mathbf{v}_\Phi). \tag{4.25}$$

The Magnus ($\mathbf{f_M}$) and spectral flow forces ($\mathbf{f_S}$) are already introduced. The Iordanskii force, $\mathbf{f_I}$ can be thought of as a Magnus force for the normal components of the liquid. For a detailed derivation of $\mathbf{f_I}$, please refer to [84]. It is worth noticing that the Magnus and Iordanskii forces are weighted with the superconducting and the normal conducting densities, respectively. Upon lowering the temperature, QP's condense to Cooper-pairs, reducing n_n in favor of n_s. Thus, in contrast to the Iordanskii force, the Magnus force should increase with decreasing temperature. The damping force, $\mathbf{f_D}$, mainly acts in opposite direction to the vortex velocity, while a small part is caused by the interaction of the vortex with $\mathbf{v}_n$, as well. $\mathbf{f_S}$ and $\mathbf{f_D}$ are controlled by their parameters that include contributions from the excitation spectrum of vortices, as discussed above. D is introduced by Kopnin [109–112] as

$$\frac{D}{n} \approx \frac{\omega_0\tau}{1+\omega_0^2\tau^2}. \tag{4.26}$$

A sketch may help clarifying how these forces influence the movement of vortices. The left panel of Figure 4.12 qualitatively depicts those forces. The Magnus force is split into components $\tilde{\mathbf{f}}_\mathbf{M}$ and $\mathbf{f_L}$, that act normal to the vortex velocity and normal to the supercurrent, respectively. Additionally, the picture is simplified in a way that for $\mathbf{f_I}$ and $\mathbf{f_S}$, only the parts that are normal to $\mathbf{v}_\Phi$ are shown, denoted now by $\tilde{\mathbf{f}}_\mathbf{I}$ and $\tilde{\mathbf{f}}_\mathbf{S}$. The parts of $\mathbf{f_I}$ and $\mathbf{f_S}$ that are directed normal to the velocity of the QP excitations outside the core are left out for better visibility. The precise magnitude of all these forces is hard to determine, anyway. Now, that an estimation for the acting forces is illustrated, we can address the two limits in the picture of Fig. 4.12. In the collisionless limit $\omega_0\tau \gg 1$, a large

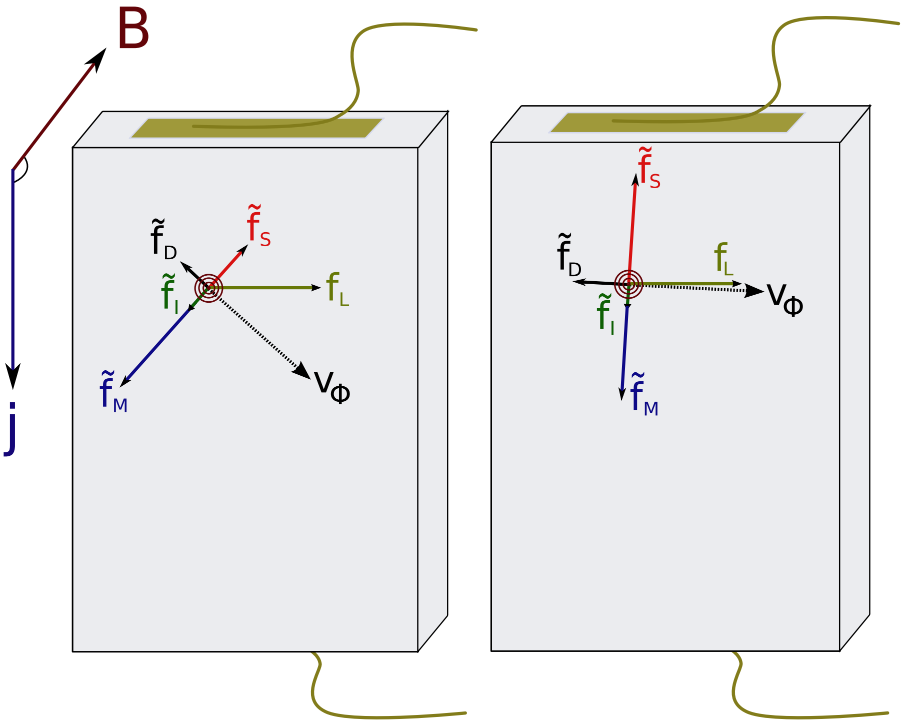

Figure 4.12: Left panel: Simple sketch of forces acting on a vortex in a current driven resistive state. The direction of the vortex movement is adumbrated by the arrow denoted with $\mathbf{v}_\Phi$. Here, $\mathbf{f}_\mathbf{M}$ is decomposed into the Lorentz force, $\mathbf{f}_\mathbf{L} = \frac{n_s h}{2}\mathbf{v}_\mathbf{s} \times \mathbf{z}$ and the effective Magnus force, $\tilde{\mathbf{f}}_\mathbf{M} = \frac{n_s h}{2}\mathbf{v}_\Phi \times \mathbf{z}$ (see text). For all other forces the components that depend on the vortex velocity is drawn, $\tilde{\mathbf{f}}_\mathbf{I}$ denoting the effective Iordanskii force (normal state analogue of the Magnus force), $\tilde{\mathbf{f}}_\mathbf{S}$ the effective spectral flow force and $\tilde{\mathbf{f}}_\mathbf{D}$ being the effective friction force. Right panel: Force balance in the hydrodynamic limit, $\omega_0\tau \ll 1$, which is met in most experimental conditions. $\tilde{\mathbf{f}}_\mathbf{S}$ is now nearly compensating $\tilde{\mathbf{f}}_\mathbf{M}$. This leads to the experimentally verified small Hall angle.

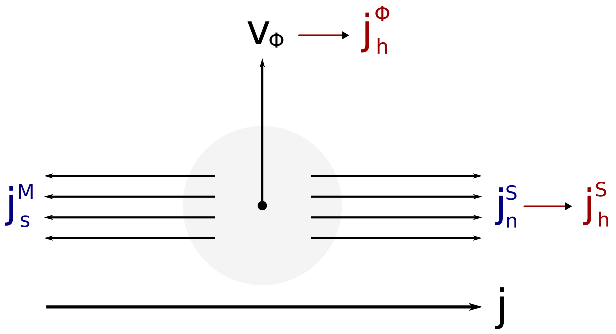

Figure 4.13: Current driven vortex motion, with the additional force due to the spectral flow effect. The spectral flow force is able to almost compensate the Magnus force, immediately explaining the small Hall angles in the hydrodynamic regime. At the same time a current of heat carrying QP's leave the core perpendicular to its velocity giving rise to the Peltier effect. $\mathbf{j_s^M}$ denotes the supercurrent density caused by the Magnus effect, taking off momentum perpendicular to the vortex velocity. Obviously, $\mathbf{j_s^M}$ carries no heat. $\mathbf{j_n^S}$ is the quasiparticle current that is caused by the spectral flow effect and is oriented antiparallel to $\mathbf{j_s^M}$. Thus, $\mathbf{j_n^S}$ balances the momentum of $\mathbf{j_s^M}$, but carries off heat, resulting in a heat current $\mathbf{j_h^S}$ density which gives rise to the enhanced Peltier effect. $\mathbf{j_h^\Phi}$ is the heat current density caused by the finite entropy within the vortex core. For better visibility, heat currents are drawn in red, charge currents in blue. Adapted from [113].

interlevel distance of the bound states in the vortex core and long scattering times lead to a vanishing of $\mathbf{f_S}$. At very low temperatures only a few quasiparticles are left, so that forces interacting with the normal liquid are assumed to be too small to be considered, i.e. the Iordanskii force that is weighted with n_n. $\tilde{\mathbf{f}}_\mathbf{S}$ is now not compensating $\tilde{\mathbf{f}}_\mathbf{M}$ anymore. Thus, $\rho \to 0$ and the vortex basically produces a Hall voltage because it moves with the applied current. This situation is not depicted here. In the hydrodynamic limit, however, the spectral flow force is fully active ($\omega_0\tau \ll 1$). Then, as illustrated in the right panel of Fig. 4.12, $\tilde{\mathbf{f}}_\mathbf{S}$ nearly cancels $\tilde{\mathbf{f}}_\mathbf{M}$ and $\tilde{\mathbf{f}}_\mathbf{I}$ and the vortex moves almost perpendicular to the supercurrent.

Fig. 4.13 illustrates the directions of resulting charge and heat current densities in this limit. The vortex moves with $\mathbf{v}_\Phi$ that is perpendicular to the applied supercurrent $\mathbf{j}$. The small but finite Hall angle is neglected here. The vortex entropy itself can only account for the heat current along its moving direction ($\mathbf{j_h^\Phi}$), giving rise to the Ettingshausen effect. While the supercurrent that is induced by the Magnus effect ($\mathbf{j_s^M}$) is unable to carry heat, the QP current generated by the spectral flow ($\mathbf{j_h^S}$) does. This explains the large Peltier effect.

4.2.5 Vortex motion in a temperature gradient

Now, a temperature gradient is applied over the sample and no overall electrical current is allowed to flow. Since QP's carry heat (at $T > 0$), they also diffuse down the temperature gradient, but in a superconductor a supercurrent counters this QP charge flow, fulfilling $\mathbf{j} = \mathbf{j_n} + \mathbf{j_s} = 0$. So, in contrast to the current-driven vortex motion we have the situation that the supercurrent and the normal current are of opposite directions, $\mathbf{j_n} = -\mathbf{j_s}$. Additionally, a new driving force, namely the thermal force introduced in Eq. (4.13) comes into play [114],

$$\mathbf{f_{th}} = -s_\Phi \nabla T, \tag{4.27}$$

where s_Φ is the transport entropy per unit length of the flux line [73, 95, 115, 116]. Thus, heat can be carried by vortex cores which leads to a diffusion of vortices along the temperature gradient from hot to cold. According to [113] and [82] and again neglecting pinning forces, the equation of motion under the influence of a temperature gradient can be written as

$$0 = \mathbf{f_M} + \mathbf{f_I} + \mathbf{f_S} + \mathbf{f_{th}} + \mathbf{f_d}. \tag{4.28}$$

The forces $\mathbf{f_M}$, $\mathbf{f_I}$, $\mathbf{f_S}$ and $\mathbf{f_d}$ are defined equally to the preceding section in a transport current. Similar to the definition of the electrical Hall angle in the current-driven situation, Eq. (4.16) a thermal Hall angle is defined as the quotient of the Nernst signal and the thermopower or in other words, relates the transverse and longitudinal voltages set up by the vortex movement,

$$\tan \alpha_{th} = \frac{e_N}{S}. \tag{4.29}$$

In contrast to the current driven vortex movement, the situation is distinctly different here. From experiment, it is known that $\tan \alpha_{th} \approx 1$ [96], meaning that the longitudinal and transverse voltages are of comparable magnitude. Again, since the voltage development is determined by the phase slippage process, $\tan \alpha_{th} \approx 1$ implicates that vortices move at angles of $\alpha_{th} \approx 45°$ with respect to the temperature gradient. This situation is sketched in Fig. 4.14. The sketch is shown for illustration purpose only, since the actual magnitudes of the forces are undetermined. Nevertheless, it depicts the pronounced difference that occurs between current- and thermally driven vortex motion. The flow of opposing currents is explicitly shown now, denoted by $\mathbf{v}_s$ and $\mathbf{v}_n$. This opposing flow is directly reflected in the direction of the forces that act on the vortex, leading to the following situation: $\mathbf{f_M}$ acts in a direction normal to $\mathbf{v}_\Phi - \mathbf{v}_s$ while $\mathbf{f_S}$ acts normal to $\mathbf{v}_\Phi - \mathbf{v}_n$. As indicated in the picture, a cancellation is unlikely even if these two forces are of similar magnitude. $\mathbf{f_I}$ is directed antiparallel to $\mathbf{f_S}$ and again is assumed to be a somewhat smaller contribution compared to $\mathbf{f_M}$ and $\mathbf{f_S}$. $\mathbf{f_D}$ is directed antiparallel to $\mathbf{v}_\Phi - \mathbf{v}_n$ and shows some angle to $\mathbf{v}_\Phi$. Finally, the driving force, $\mathbf{f_{th}}$ is acting in direction of the temperature gradient. So, the counterflow of charge currents in a temperature gradient may explain the occurrence of large thermal Hall angles of order 45°. These estimations are in good agreement with the thermal Hall angles that are observed during this work. They will be presented later, in section 7.4.

It is interesting to notice what happens if we now assume the QP's to be of opposite charge. The temperature gradient still diffuses these QP's from hot to cold, which is again

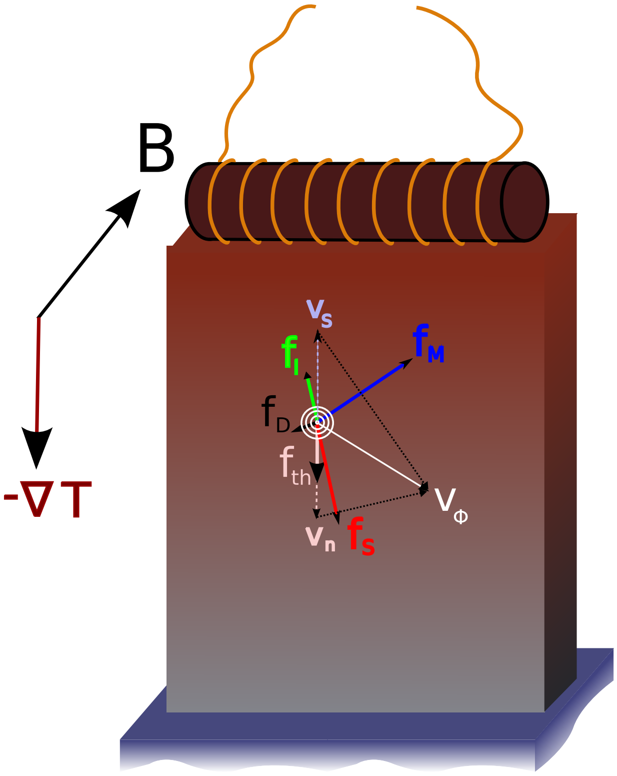

Figure 4.14: Simple sketch of forces acting on a vortex in a temperature gradient. $\mathbf{v_s}$ and $\mathbf{v_n}$ indicate the counterflow of superconducting and normal conducting parts of the fluid, respectively. $\mathbf{f_{th}}$ is the driving force that is directed from hot to cold. All other forces are directed as is denoted in the text.

countered by a Cooper-pair current (also of opposite charge). Only, the rotation direction of the superconducting ring current that is caused by the magnetic field penetrating the bulk of the sample is reversed now. This change in direction, in turn, leads to a reversal of the direction of the Magnus force. We can discuss this situation descriptively again. Let us assume the charge carriers are hole-like in the illustration of Fig. 4.14. Flipping to negative charge would lead to a tilt of the velocity vector around the axis of ∇T. Consequently, the sign of the thermopower, S, in the flux flow regime should be reversed, too. And indeed, as will be shown in one sample with a negative S above T_c, S keeps its negative sign also in the vortex regime below T_c.

To fit this picture into the magnetic field symmetric character of the thermopower, we can estimate the sign of S also by analyzing the electric field generation in the flux flow regime, as of $E_x = v_y B_z$. The thermopower voltage is generated by the v_y-component of the vortex velocity. If the magnetic field is reversed, the direction of the ring current and thereby v_y is reversed. Of course, the field direction is also reversed. Now, we have $E_x = (-v_y)(-B_z)$. The voltage does not change its sign. Flipping the charge would reverse v_y only and so the sign of S changes as well.

Subsequently, the thermal Hall angle is negative if the thermopower is negative, since the positive sign of the vortex-Nernst-voltage is dictated by the diffusion of vortices from the hot to the cold end (v_x never changes its sign).

A detailed mathematical analysis of the equation of motion (Eq. 4.28) in a temperature gradient is given by Freimuth *et al.* [82, 113]. As a result, a rather simple expression for the vortex-Nernst signal is derived:

$$e_N \approx \rho \frac{s_\Phi}{\Phi_0}. \tag{4.30}$$

Thus, the Nernst signal e_N is mainly determined by the flux flow resistivity ρ and the transport entropy s_v. Φ_0 is the elementary flux. Later it will be shown that this contribution to the overall Nernst signal can become extraordinarily large compared to Nernst signals of other origins.

In analogy to the current-driven vortex motion, we can estimate how e_N is expected to develop in the hydrodynamic and collisionless limits. ρ is determined to be large in the hydrodynamic limit, mainly because forces like the spectral flow force and the damping force are active. Thus, because of Eq. 4.30, e_N should be large in this limit, too. Consequently and concomitant with the small ρ in the collisionless limit, e_N is expected to be small in this limit, as also stated in [113].

4.2.6 Summary

In summary, the vortex-Nernst effect can be described by $e_N \approx \rho s_\Phi / \Phi_0$. It will turn out that this contribution is extraordinary large in the vortex liquid phase of high-T_c's in comparison to the signals quasiparticles are able to produce in the normal state. In order to explain a large Peltier effect, the "spectral flow" force was introduced, a force that couples the motion of a vortex to that of the normal excitations above the superconducting gap. To formulate it somewhat loosely, the spectral flow is provided by quasiparticles in the vortex core that, under the conditions stated in this chapter, are able to leave the core at right angles to the vortex velocity. This scenario led to very good agreement with experiments of the longitudinal thermomagnetic effects [113]. To stay descriptive, while in a current driven vortex flow, the Lorentz force determines the flux flow resistivity in the mixed state and the vortex velocity dependent parts of the perpendicular forces (Magnus, Iordanskii and spectral flow) determine the Hall effect. Since they nearly cancel, the Hall effect is very small. In a temperature gradient, $\mathbf{f_{th}}$ alone would lead basically to a large Nernst effect, so that the appearance of a large thermopower, as verified by many flux flow experiments, $\tan \alpha_{th} \approx 1$, requires the existence of an overall perpendicular force on the vortex.

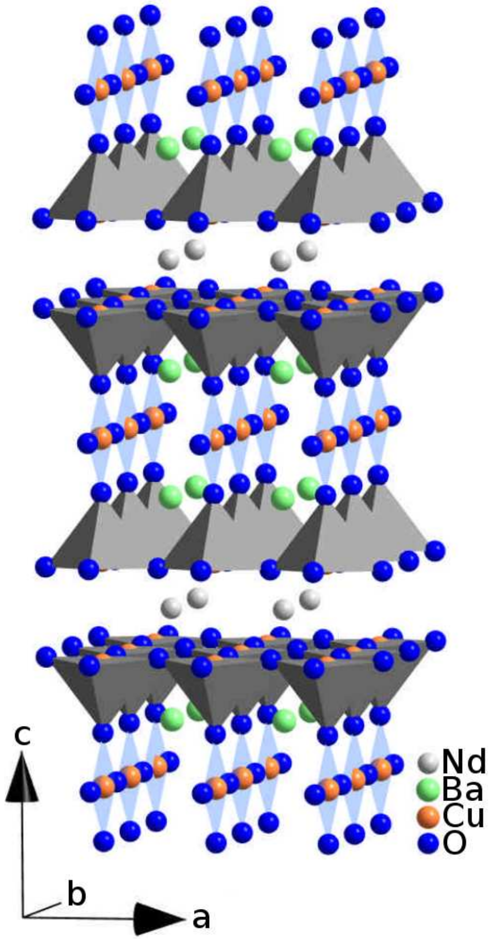

Figure 4.15: Structure of $NdBa_2Cu_3O_7$. CuO planes are intersected by Nd ions. From the ICSD database with structural data of [117].

4.3 The system $NdBa_2\{Cu_{1\text{-}y}Ni_y\}_3O_{7-\delta}$

In this section the system $NdBa_2\{Cu_{1\text{-}y}Ni_y\}_3O_{7-\delta}$ as a model system for high temperature superconductivity will be introduced. The possibilities of probing the physical properties of superconductivity by replacing Cu ions either by magnetic or nonmagnetic ions make this system of particular interest. Investigations are mostly taken out by choosing Ni as the magnetic ion and Zn as the nonmagnetic one. Basic differences to other high-T_c material will also be discussed.

4.3.1 Structure

The class of the high-T_c's can be summarized as oxides that crystallize in a layered Perovskite-like structure. Fig. 4.15 depicts the structure of $NdBa_2Cu_3O_{7-\delta}$ which is similar to the structure of $YBa_2Cu_3O_{7-\delta}$, by far the most examined high-T_c compound. They crystallize in an orthorhombic symmetry with lattice parameters a=3.8643, b=3.9125 and c=11.749 (ICSD crystallographic database [117]). The focus within these structures points

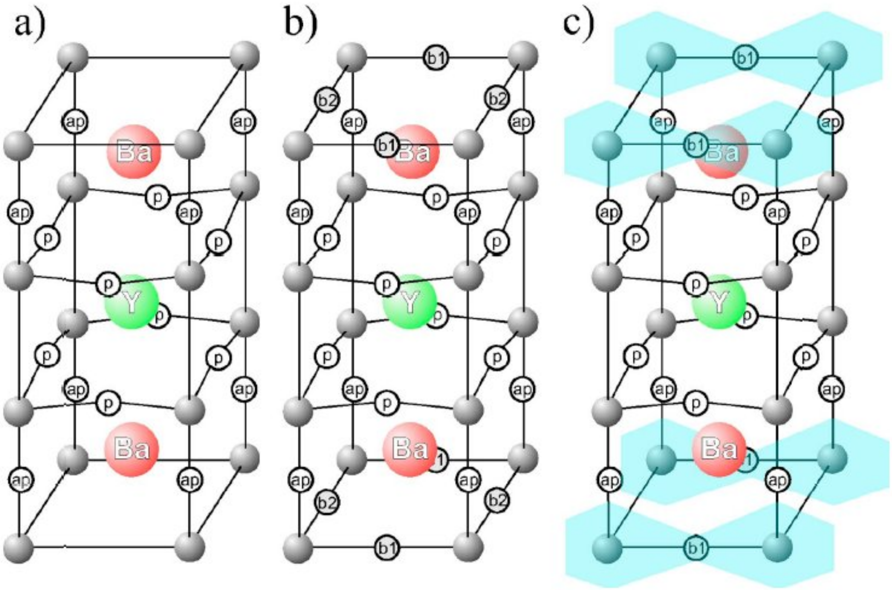

Figure 4.16: Structure development with oxygen doping, from tetragonal (left) to the orthorhombic structure with its characteristic Cu-O chains (right) [118].

to the Cu-O layers since these are held responsible for being the medium superconductivity develops in. Four oxygen atoms surround one copper atom in the layer while the apex oxygen atom builds the top of a pyramidal structure and at the same time bridges to the next Cu-O chain. The Nd or any other rare earth atom separate two adjacent Cu-O layers. Beginning with an oxygen content of O_6, no chains would be present and the structure is tetragonal. Adding oxygen towards the optimal doping of O_7 the chains are build up which leads to an orthorhombic distortion, as shown in Fig. 4.16.

The transport properties go along with this structural anisotropy. Electrical resistivity is found to be two to three orders of magnitude larger perpendicular to the Cu-O layers in the YBaCuO-family and in the LaSrCuO-family and even four to five orders of magnitude larger in the BiSrCaCuO- and TlBaCaCuO-families than parallel to the Cu-O planes [119]. Another measure for the anisotropy in these compounds is defined via the characteristic lengths in superconductors:

$$\Gamma = \lambda_c/\lambda_{ab} = \xi_{ab}/\xi_c = B_{c2}^{ab}/B_{c2}^{c}, \tag{4.31}$$

with Γ being the anisotropy parameter [120]. λ, ξ and B_{c2} being the penetration depth, coherence length and upper critical fields, respectively. NdBaCuO and related materials have $\Gamma \approx 5 - 7$ and the even more two-dimensional compounds like the Bi- or Tl-based superconductors are lying in the range of $\Gamma \approx 50 - 80$ [121, 122].

4.3.2 Doping

The possibility of doping in the high-T_c materials leads to a variety of investigations towards the revelation of the mechanism of superconductivity. The focus in this section will be mainly on the systems R123 (R=Y,Nd) and $La_{2-x}Sr_xCuO_4$.

Substitution on the Cu sites

Small amounts of impurities on the copper sites influence the superconducting state. E.g. potential scattering from nonmagnetic impurities leads to a reduction of T_c caused by pair breaking [123]. Studying the response to these intentionally incorporated impurities can shed light on the symmetry of the order parameter because clear differences are predicted for the variation of experimentally accessible parameters such as T_c or the superconducting condensate density n_s [124–126]. Zn as a nonmagnetic ion has been excessively studied because it suppresses T_c exceptionally fast while the carrier concentration remains unaltered in the CuO_2 sheets [127–130]. Clear signatures of T_c depression due to pair breaking of the Cooper-pairs have been found [127, 128]. The influence of Zn substitution on T_c and the condensate density n_s has been investigated in the underdoped, optimally doped and overdoped regime of $Y_{0.8}Ca_{0.2}Ba_2(Cu_{1-y}Zn_y)_3O_{7-\delta}$ [131]. The resulting rapid depression of n_s even for low Zn contents is a characteristic feature that is expected for systems with $d_{x^2-y^2}$-wave order parameters when nonmagnetic impurities lead to isotropic scattering in the unitarity limit [124–126]. To further clarify whether the underlying mechanism of superconductivity is of magnetic origin, as proposed by [132–136], the influence of Ni substitution is also investigated. Ni is believed to be in the $Ni^{2+}3d^8$ high spin state ($S = 1$) within the CuO_2 planes. Above T_c each Ni atom possesses a strong magnetic moment of around $1.5\mu_B$ [137]. The local density of states at single Ni impurity states were imaged via STM in $Bi_2Sr_2CaCu_2O_{8+\delta}$ [138]. It was found that the reduction of the transition temperatures is mostly dominated by potential scattering. While Zn atoms act like a “magnetic hole” that strongly alter Next-Neighbor exchange correlations and destroy superconductivity locally, Ni atoms retain their magnetic moment and thereby do not perturb the antiferromagnetic correlations of neighboring atoms and superconductivity is not destroyed locally. These findings contrast those for s-wave superconductors. In s-wave superconductors, the magnetic impurities are the ones that destroy superconductivity even in low concentrations while nonmagnetic impurities are not as “aggressive”.

The high-quality single crystals of $NdBa_2\{Cu_{1-y}Ni_y\}_3O_{7-\delta}$ used in our study were grown by a flux method as described in detail in [10] and [139]. Ni substitution does not alter the hole doping content significantly which is confirmed by thermopower measurements. The Ni concentration is related to all Cu places in the crystal. It is estimated that half of the Ni impurities reside within the CuO_2 planes, leaving the other half in the chains. The influence of substituting magnetic Ni ions or nonmagnetic Zn ions in the CuO_2 planes has been investigated by several groups [138, 140, 141]. In $YBa_2Cu_3O_{7-\delta}$ (YBCO) a linear depression of T_c is found for both impurities [140], but with different slopes.

Changing the carrier content, Phase diagram

While in $La_{2-x}Sr_xCuO_4$ each trivalent La atom that is substituted by a divalent Sr atom leads to an additional hole as charge carrier, Y123 and Nd123 are charge carrier controlled via the oxygen content ranging from O_6 to O_7. The relation between the oxygen content and the hole concentration p per Cu in the CuO_2 planes is more complicated and thus determined from transition temperatures using the empirical formula [142]

$$\frac{T_c}{T_c^{max}} = 1 - 82.6(p - 0.16)^2, \tag{4.32}$$

which is a good approximation for many cuprate systems [143]. Their properties include antiferromagnetic insulators with ordering temperatures $T_N \approx 400\,\mathrm{K}$ at low oxygen content ($\delta \geq 0.5$) to superconductivity with T_c exceeding $90\,\mathrm{K}$ close to the composition O_7. Although the removal of oxygen causes vacancies only in the chains, it is the planes that dominate both the antiferromagnetic [144] and superconducting properties. The "parent compound" La_2CuO_4 shows insulating behavior which is well understood by the concept of Mott insulation [145, 146]. The antiferromagnetic ordering temperature $T_N \approx 300\,\mathrm{K}$ in LSCO or $T_N \approx 450\,\mathrm{K}$ in YBCO, (Fig. 4.17 and Fig. 4.18, respectively) is quite low compared to the relevant exchange energy J of order 1500K [147, 148]. This is due to the finite interlayer coupling which is furthermore frustrated in La_2CuO_4 [149]. Increasing the hole concentration leads to a rapid decrease of the antiferromagnetic ordering temperature until complete suppression at $p, x \sim 0.03 - 0.05$. Almost immediately thereafter superconductivity appears in a range of $p, x \sim 0.06 - 0.25$. The dome-shaped superconducting region is common to all substances of the hole-doped family, varying only in the height of T_c^{max} from about $40\,\mathrm{K}$ (LSCO family) to $95\,\mathrm{K}$ and higher in substances like YBCO or Bi-2212 [123]. However, the dome is only completed in direction of high doping concentration in the LSCO-family. The dome for YBCO-like substances is shown in Fig. 4.18 and ends with its highest T_c at O_7, so to say at half the LSCO-dome. The doping concentration leading to T_c^{max} is referred to as "optimally doped", increasing and decreasing concentrations as "overdoped" and "underdoped", respectively. The fast breakdown of antiferromagnetic order with respect to the addition of just a few percent of charge carriers (holes) can be understood within the following picture. As illustrated in Fig. 4.19 a hole is introduced into an antiferromagnetic spin background and would like to hop with amplitude t to lower its kinetic energy. One hop in turn would leave one spin in a ferromagnetic environment which would cost an energy of $3J$. So if $t \gg J$ the hole is strongly delocalized and the system should become a metal with weak residual antiferromagnetic correlation. If $t \leq J$ the behavior is much less predictable because antiferromagnetic correlations are to be maintained while the hole is allowed to move as freely as possible. The highest partially occupied copper d orbital has $x^2 - y^2$ symmetry because the apical oxygens slightly distort the environmental symmetry which leads to splitting of the e_g orbitals. The lobes of the $d_{x^2-y^2}$ now directly point toward the lobes of the oxygen p orbitals and thereby form a strong covalent bond with a large hopping integral t_{pd}. Each unit cell has one copper and two oxygen orbitals and the system can be described by a model including three bands

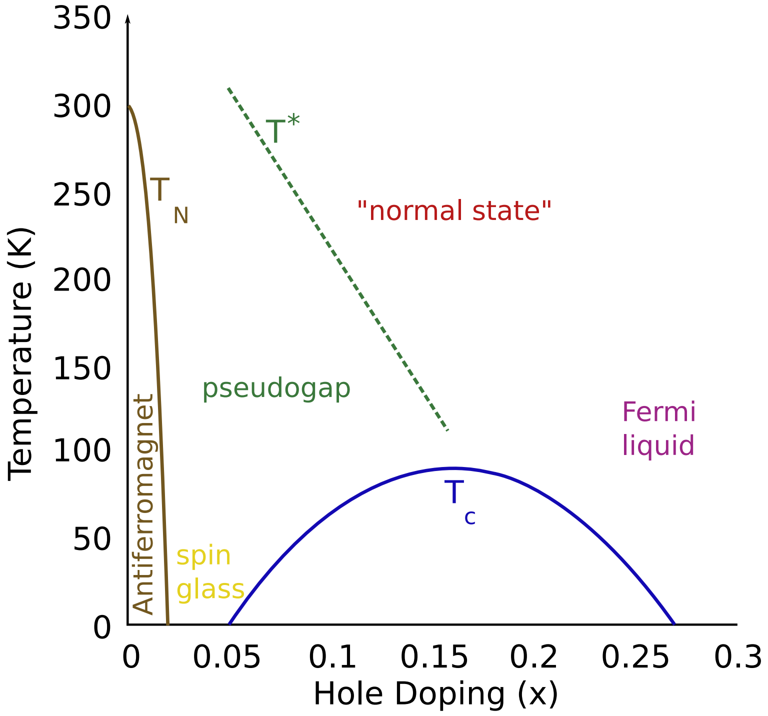

Figure 4.17: Generic phase diagram of the cuprate family [150].

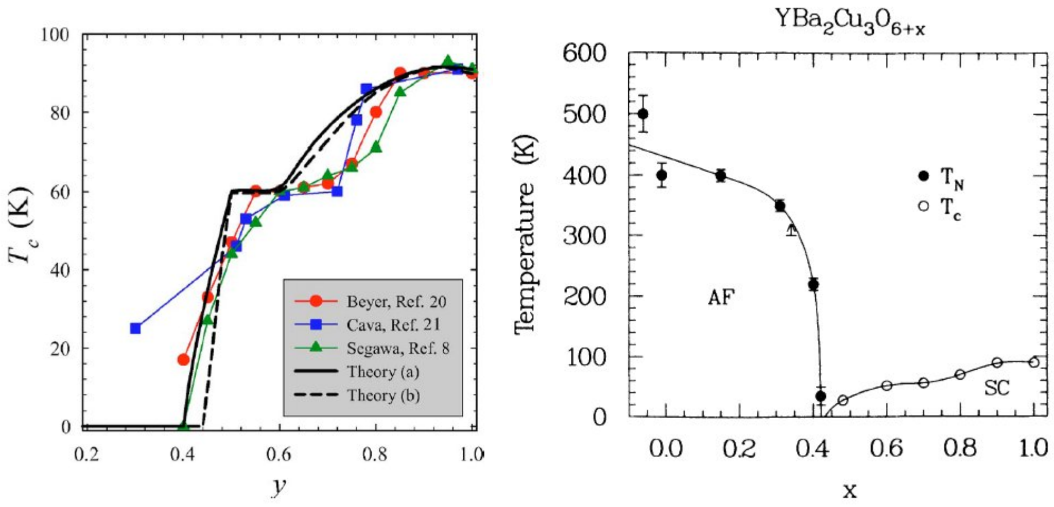

(a) Superconducting dome

(b) Phase diagram YBCO

Figure 4.18: Summary of the measurements of different groups revealing the T_c dependence on oxygen doping in YBCO_{6+x} (a) [118]; Phase diagram YBCO_{6+x} showing the transition from the antiferromagnetic phase into the superconducting one (b) [151].

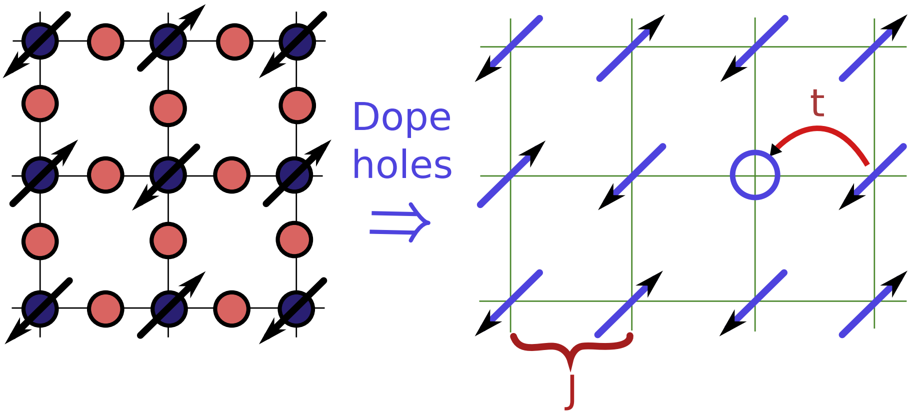

Figure 4.19: Illustration of the change in the copper-oxygen layers with hole doping. J is the antiferromagnetic exchange energy while t stands for the hopping parameter. $t \gg J$ leads to metallic behavior, while $t \ll J$ favors localized states (see text) [123].

[152]. In the hole picture the Cu site with energy E_d is occupied singly and the oxygen orbitals (E_p) are empty. The lowest excitation is a hop from Cu to O with amplitude $-t_{pd}$. The system's behavior is governed by the relation of $E_p - E_d$ and t_{pd} i.e. if $E_p - E_d$ is considerably larger than t_{pd} the system is insulating in the scheme of charge transfer insulators [153] with experimentally observed energy gaps of about 2.0 eV [149]. The local moments on nearest neighbor Cu sites prefer antiparallel alignment because both spins can virtually hop to the intermediate oxygen orbital which is only allowed if not all quantum states are equal (Pauli principle). The exchange integral is then expressed as

$$J = \frac{t_{pd}^4}{(E_p - E_d)^3}, \tag{4.33}$$

which simplifies to $J = 4t^2/U$ in a one-band Mott-Hubbard insulator [154, 155]. J is experimentally found to be about 0.135 eV in La_2CuO_4 [156, 157] and 0.12 eV [158] in YBCO. Since the energy for doubly occupying the Cu $d_{x^2-y^2}$ orbitals is very high, additionally doped holes will reside on the oxygen sites, occupying the p orbitals. The hole now resonates on the four sites surrounding a Cu and the spin of the doped hole combines with the spin on the Cu to form a Zhang-Rice spin singlet [159]. This singlet is able to propagate with an effective nearest neighbor hopping integral of order $\tilde{t}_{pd}^2/(E_p - E_d)$ and with $(E_p - E_d)$ playing the role of a Hubbard U.

4.4 Pseudogap - a brief overview

In conventional superconductors the amplitude of the order parameter $|\Psi|$ [68] vanishes when the system is driven into the normal state. The energy gap collapses and without an amplitude the phase of the order parameter is useless. For the high-T_c's it is believed that at least over some range of doping towards the underdoped side the transition to the normal phase takes place because the phase loses its rigidity. This on the other hand means that the state above superconductivity still has a non-zero value of the amplitude of the order parameter but with a spatially fluctuating phase. This phenomenon has been given the name "pseudogap" phase. The pro and cons that are delivered by a variety of measurements will be introduced and briefly discussed in this section. This exotic state is exhibited in the normal region of the optimally and underdoped high temperature cuprate superconductors, as depicted in Fig. 4.17. It was first discovered in 1989 by studying spin dynamics in YBCO [6] with nuclear spin-lattice relaxation measurements. These measurements indicate the possibility of an onset of spin pairing well above T_c. Similar implications have been proposed after measurements of the optical conductivity probing the charge channel [5]. A good approach towards the understanding of the mechanisms of high-T_c superconductivity seems to be to first understand the normal state from which it arises. In magnetic susceptibility [8] and Knight shift [7] measurements, a significant suppression of the uniform static susceptibility was found at higher temperatures than deduced from the low frequency dynamic spin response [6]. Such a suppression can be found in a classic superconductor where the pair state is a spin singlet. Crossing T_c, the spin response of the condensate is quenched. In high-T_c material this spin singlet formation seems to set in at T^*, the pseudogap temperature, and shows no additional anomaly at T_c.

As mentioned above the c-axis optical conductivity is already suppressed as the temperature is lowered from 295 K to 150 K while the frequency at which the gap sets in is temperature independent. By exciting charge carriers perpendicular to the planes, a tunneling current of electrons is required so that it is argued that the gap is seen directly in the c-axis response [150]. Another supporting tool in the struggle to reveal the features of the pseudogap is the angle resolved photoemission, which directly measures the momentum-resolved electron excitation spectrum of the CuO planes [160]. Probing the underdoped region of $Bi_2Sr_2CaCu_2O_{8+\delta}$ upon cooling the sample, it is found that not only a pseudogap opens up but it opens at different temperatures for different directions in k space [161]. The full evolution of the Fermi surface of the underdoped copper oxides is sketched in Fig. 4.20, where Γ resembles (0,0) and Y is (π, π) of the two dimensional Brillouin zone of the copper oxide planes. The picture is drawn in units of $1/a$, a being the Cu-Cu distance. For d-wave order parameters gapless excitations below T_c are only possible at the nodes of the $d_{x^2-y^2}$ wave functions (left panel in Fig. 4.20). At $T \geq T_c$ the nodal point is expanded to so called '"Fermi-arcs'" until at T^* the full Fermi surface is formed (right panel) [161, 162]. A possible scenario that is consistent with the experiments above is one in which pairs begin to form at T^* but are lacking long range phase coherence. The condensation of these pre-formed pairs in this picture would occur at T_c. This was the starting point for Nernst effect measurements because this kind of thermoelectric response is a very sensitive probe

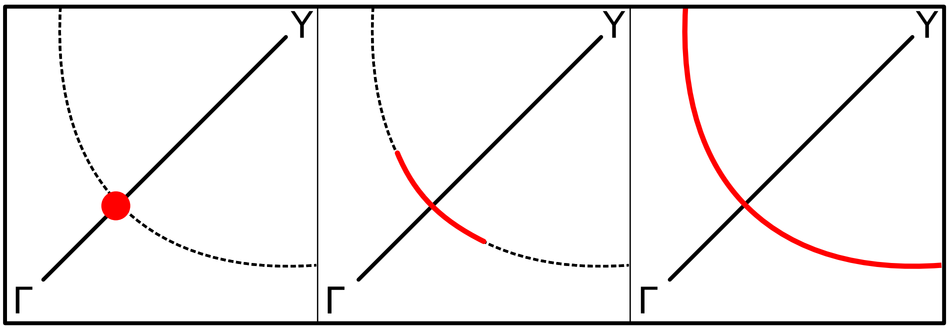

Figure 4.20: Development of the Fermi surface from the superconducting (left) to the normal state. From a nodal state to so called "Fermi arcs" to the fully formed Fermi surface (right panel). $\Gamma = (0{,}0)$ and $Y = (\pi, \pi)$, from [161].

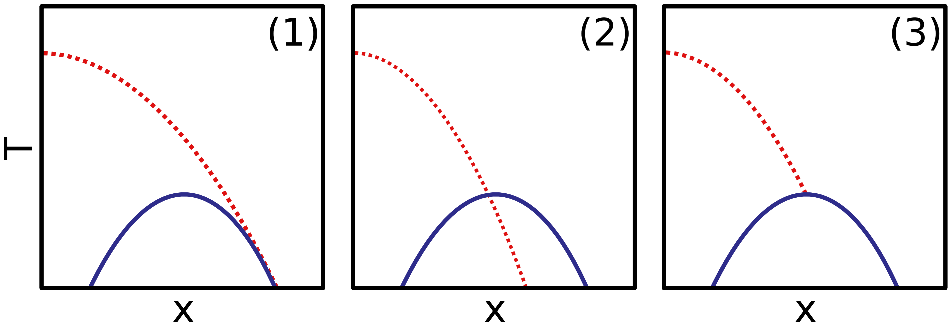

Figure 4.21: Three different relations between PG and SC, [161]. (1) Preformed pair scenario; (2) PG and superconductivity as competing states; (3) The pseudogap state is being replaced by the superconducting gap.

for vortex formation in the superconducting state [4]. Results and implications of Nernst effect measurements are discussed in detail in chapter 7.3.

Complementary to momentum resolved ARPES is the data collected by scanning tunneling microscopy (STM) because it resolves real space. A gap in the spectra but no coherence peak is interpreted as pseudogap here [163, 164]. These features are seen in the same temperature range as the ARPES experiments were performed in. In another STM experiment a coexistence of superconducting regions and pseudogap regions was found. The pseudogap regions grow with reduced doping [165, 166].

Fig. 4.21 illustrates three different scenarios of how the pseudogap will develop while approaching the low temperature regime in the vicinity of superconductivity. The line drawn here is always to be taken as a crossover rather than a strict phase separation line. The sketch to the left corresponds to the scenario of spin singlet formation at T^* but without long range phase coherence [167]. This picture treats the pseudogap phase as one from which either the antiferromagnetic phase at low dopings or the superconducting phase at dopings from ~0.05 to ~0.26 develops [168]. Diagram (2) depicts a scenario which can be interpreted as the pseudogap competing with the superconducting gap. Indications of a T^* line below T_c come from experiments in which impurities suppress superconductivity which in turn uncovers the pseudogap line below. T^* in this model is believed to end at a quantum critical point, an idea that is supported by specific heat measurements which show a peak of the superconducting condensation energy at that doping level [169]. The third picture of Fig. 4.21 sketches a pseudogap that terminates at T_c and is replaced by the superconducting gap below T_c. Spectroscopic methods such as inelastic neutron scattering, which reveals a spin resonance peak below T_c and also shows a precursor signature at T^* [170], in combination with STM might shed light on this picture as resolution is increased in the relevant regions of the phase diagrams.

5 Experimental

In this chapter I will describe the process from sample contacting to detailed data analysis of the galvanomagnetic measurements such as the Nernst effect and the thermopower. The thermocouples used in most setups are Chromel-Au+0.07%Fe which are calibrated and tested in a variety of measurements [148, 171].

5.1 Measurement of transport properties

Measurements on the samples were performed such that the equilibrium state is disturbed by either applying a current through the sample or a temperature gradient. After some time, a steady state develops and the required quantities can be recorded. In this thesis, longitudinal effects such as thermopower, heat conductivity and resistivity as well as transverse effects such as the Nernst effect are measured. Generally, two methods can account for the recording of data of the required quantities. One method is performed by stabilizing the control parameters temperature and magnetic field. The other way is done by stabilizing one of these, e.g. T, and continuously sweeping the other, e.g. B.

5.1.1 Preparing electrical contacts

Sample geometry

The preferable geometry is a cuboid, because two parallel areas are needed to apply a uniform temperature gradient over the sample, which is achieved through the connections of the chip heater to the sample and the connection at the bottom of the sample to the measuring insert. The dimensions should be as large as possible, just because the voltage to pick up is caused by an electric field set up by the relevant thermoelectric effects. The voltage to measure is then linear in contact distance (d), $U = E \cdot d$. Unfortunately, most samples that were available during this work are very tiny, sizes smaller than $1\,\mathrm{mm}\times 1\,\mathrm{mm}\times 0.5\,\mathrm{mm}$ which leads to very small voltages and therefore eventually to resolution problems during the measurement. Unlike the transverse Hall effect, the off-diagonal components of the thermolectric response of the system do not depend on the sample thickness.

Contact resistance

In order to pick up tiny voltages in the range of a few microvolts and less, it is required that the contact resistances between the electrical contacts and the sample are kept low. For the class of $\mathrm{NdBa_2\{Cu_{1\text{-}y}Ni_y\}_3O_{7-\delta}}$ samples the resistance ranges from 1 Ohm to 3

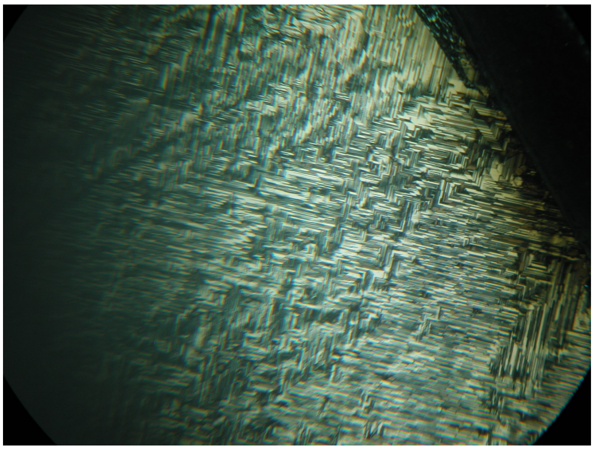

Figure 5.1: Polished surface of a $NdBa_2(Cu_{0.97}Ni_{0.03})O_7$ sample. The twinning of the ab planes is revealed by polarization microscopy as the view is along the *c*-axis. Shown here is a clipping of the sample of approximately 0.7 mm×0.5 mm.

Ohms at room temperature at typical contact distances of ≈ 0.2 mm. Reaching this quality of contact resistances is more a matter of experience than a calculable quantity, since for almost each sample class an individual approach is needed. I will briefly sketch the way for the class of $NdBa_2\{Cu_{1\text{-}y}Ni_y\}_3O_{7-\delta}$. The designated contact area should be polished very accurately (see Fig. 5.1). To pick up the Nernst voltage, thin copper wires of 25 μm to 50 μm are attached either to the sides of the sample or at the sides of the area that is directed perpendicular to the magnetic field and parallel to the temperature gradient (see Fig. 5.2, and photo 5.3). The contacts are glued with a two-component silver epoxy with a characteristic temperature dependent curing time. The most successful method to reduce contact resistances, R, is as follows. The glue is continuously heated up to about 300-350°C while R is measured with a Keithley 2400 Source meter. Measuring R with currents in the range of 100 mA to 700 mA provides an additional heating of the contacts since they are the spots with the highest resistance of the whole path through the sample, so that most of the electrically applied power is transformed into heat at the contacts. By doing so, the measured R drops from several kOhms at the beginning of the heating process to about 0.5-5 Ohms. As the sample cools down after this heating process, the contact resistances can relax back far beyond the desired small values. Then the time that the sample is exposed to heat should be increased carefully until the resistances stay in their typical 1 to 3 Ohm range.

Experimental setup

For the Nernst effect measurements two thin copper wires are attached at the sides of the sample with a two-component silver epoxy in order to pick up a transverse voltage. The sample is then mounted to a copper block which is at the same temperature as the temperature-stabilized surrounding. On the top of the sample a chip heater is thermally connected by an insulating varnish (VGE 7031, Lakeshore). By applying power to the heater a temperature gradient is created over the sample of about 0.5 K/mm which is detected by a AuFe-Chromel thermocouple. Two methods were used to detect the Nernst

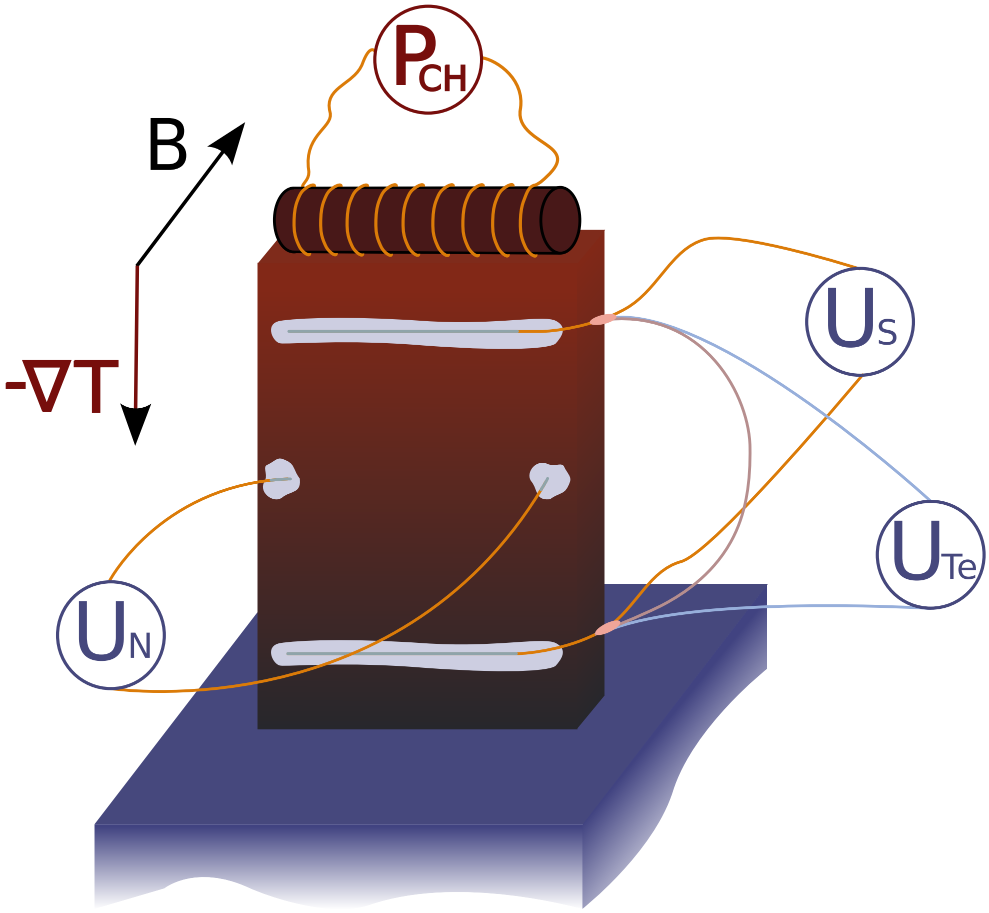

Figure 5.2: Schematic drawing of the contacts on the sample to measure Nernst effect (isothermal), Seebeck effect and heat conductivity. Magnetic field is directed perpendicular to the surface area. $\mathrm{P_{CH}}$ stands symbollically for the power applied to the chip heater. A current of order 0.5 mA leads via $P = I^2 \cdot R$ to the desired heating. The heater is electrically insulated from the sample by a sheet of cigarette paper. $\mathrm{U_N}$ shows how the transverse voltage is picked up and $\mathrm{U_S}$ denotes the wiring of the thermopower measurement. These longitudinal contacts are glued to the sample over some distance. This, on one hand increases the stability of the contact and on the other hand often leads to better contact resistivities. $\mathrm{U_{Te}}$ is the thermocouple that is connected directly to the wiring of the thermopower, glued with an insulating varnish (VGE 7031, Lakeshore). The gray areas symbolize the silver epoxy glue which makes the contact between the sample and the wiring.

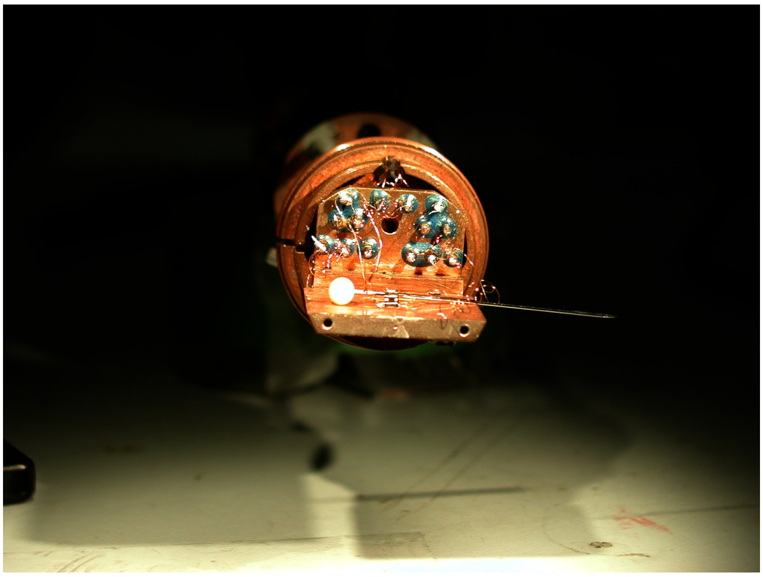

Figure 5.3: A sample prepared for the measurement of the isothermal Nernst effect. A fixing pin lies behind to make length scales comparable. The little black spot in the middle of the copper table is identified as the sample with its chip heater on top and contacts attached as shown in the scheme of Fig. 5.2.

signals. Most of the measurements were performed by stabilizing the temperature (to about 1 mK) and the temperature gradient for each magnetic field (typically in steps of 0.5 T). Then the temperature gradient is removed in order to subtract offset voltages. For the second method the temperature is stabilized again very accurately (1 mK), then the heater power is switched on and the field is continuously swept at a typical rate of 0.3 T/min. A second sweep with the heater switched off is performed at the same temperature in order to determine field-dependent offset voltages. A typical setup of the sample is depicted in Fig. 5.3, in contrast to the dimension of a fixing pin, placed near the sample. The sample is the tiny black cube in the middle of the copper table. The brighter spots on the sample are the electrical contacts as schematically displayed in Fig. 5.2.

5.1.2 Stabilizing temperature and magnetic field

The magnetic field is created within a superconducting coil which is supplied by currents ranging from 0-120 A (Oxford IPS 120). The magnetic field strength is set either manually or by certain bus commands and does not need further attention since the accuracy is limited by the power supply itself. The temperature on the other hand is controlled by a self regulating loop which is realized by a software PID algorithm of a temperature controller, Lakeshore 340. Setting the stabilization criteria for the desired quantities properly is essential for the data acquisition process. By default the continuously taken measurement values are averaged over 150 data points. Then the slope and the standard deviation are calculated, the temperature is additionally controlled by the deviation from the setpoint.

Stabilization criteria for offset, slope and deviation are entered into the appropriate fields of the recording software, KSR [148]. For the temperature stabilization, values of $\sim 1 \cdot 10^{-3}$ are entered. The offset tolerance as well as the standard deviation are then 1 mK. The actual slope in units per time depends on the integration time of the hardware that the data is read from. Typical stabilization criteria for the electrical contacts on the sample that pick up voltages were $\sim 10 \cdot 10^{-9}$ for the standard deviation and $< 10 \cdot 10^{-9}$ for the slope. The values for the slope and deviation of the thermocouple voltages are often not better than 15-20 $\cdot 10^{-9}$. Depending on the quality of the contacts, these values sometimes have to be altered during the measurement, as i.e. high-temperature measurements and magnetic fields may influence the contact noise. If the measured values finally are within the set range of all measured quantities, then the average over the last 150 points is taken as offset signals. After that, the heater is turned on, leading to measurement quantities under the influence of a temperature gradient. The same stabilizing criteria are applied and the offset values are subtracted, leaving the desired quantities. The voltage on the transverse contacts is recorded by a Keithley 2001 voltmeter with preamplifier 1801, which has a better point to point noise ratio than the Keithley 2182 by a factor ~ 25 [1]. The measurement range was always set to "high accuracy" with analog filtering set to "slow".

5.1.3 Sweeping the field or the temperature

Temperature sweeps are basically used only for resistivity measurements because the response time of the sample to a temperature gradient is very sample dependent. A large response time makes the correction of offset values difficult. While the temperature gradient slowly relaxes, the base temperature sweep goes on. The result would be that offset and data point are recorded at different temperatures. Thus, stabilizing the temperature and sweeping the magnetic field is a much more accurate method of data acquisition. Temperature sweeps are not performed in any measurement of this thesis. The need to carry out transport measurements under the influence of a temperature gradient at fixed temperature is due to the desired high accuracies better than 100 nV/KT. Before the field sweep starts, the desired quantities should be stabilized again very accurately, i. e. the temperature should be set as accurate as ±1 mK. Then a field sweep without an applied temperature gradient must be performed to acquire the field dependent offset signal at the stabilized temperature. As is depicted in Fig. 5.4, the offset voltages themselves depend on the direction of the field sweep (the sign of $\partial B/\partial t$). This is due to eddy currents in the metallic parts of the setup and has a magnitude of about 0.1 μV. Now, the stabilization process is repeated, this time with the chip heater current turned on, which leads to the desired temperature gradient over the sample. In order to avoid the offset due to eddy currents, the adjacent field sweep should be performed in the same direction as the offset sweep. Apparently, the noise of offset and data sweeps also increase with increasing magnetic fields.

The temperature gradient applied to the sample is held in the range of 3 K/cm to

---

[1] Model 1801 Nanovolt Preamp Specifications Rev. A

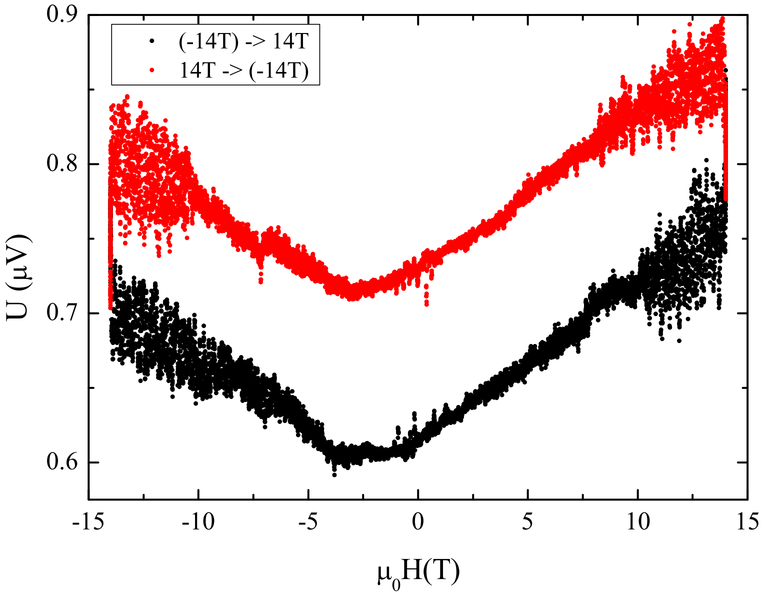

Figure 5.4: Offset voltages at the transverse contacts, while the magnetic field is swept with 0.3 T/min from -14 T to 14 T (lower black curve) and back (upper red curve). The sample (optimally doped $NdBa_2Cu_3O_{7-\delta}$) is measured at stabilized 84 K. ΔU, the difference between the two runs, is caused by eddy currents proportional to $\partial B/\partial t$.

10 K/cm. As can be seen in the theoretical introduction the temperature gradient is proportional to the driving force of the vortex along the temperature gradient. So, vortex velocity, which in turn leads to bigger voltages and therefore to less noise in the signal, is connected to the temperature gradient. The only problem is the heating of the sample itself due to higher temperature gradients. In Fig. 5.5 the raw signal of the vortex induced voltage vs. magnetic field is shown for three different chip heater currents of 1.5 mA, 1.8 mA and 2 mA. The offset to 0 is due to the misalignment of the contacts which automatically leaves a slight temperature difference between the left and the right wire. Then the thermopower of the wires leads to this offset which is symmetric and is got rid of after the antisymmetrisation process. The magnification in the inset reveals a slight shift in the melting field due to a heating of the sample caused by three different chip heater power appliances. Thus, the temperature gradient should be kept as constant as possible during the measurement. The magnetic field dependence of the different temperature gradients that result from three different chip heater currents is shown in Fig. 5.5 in the lower left inset. The temperature difference ΔT is proportional to the applied chip heater power, and thereby $I^2_{Heater} \propto \Delta T$. Furthermore, ΔT is only weakly dependent on magnetic field (and symmetric), but shows a slight tendency of an increasing field dependence for increasing ΔT. Finally, the influence of the sweeping rate of the magnetic field on the signal is also investigated. Fig. 5.6 compares the analyzed Nernst signal of three different sweeping rates, revealing a rather good independence within the shown range between 0.1 T/min

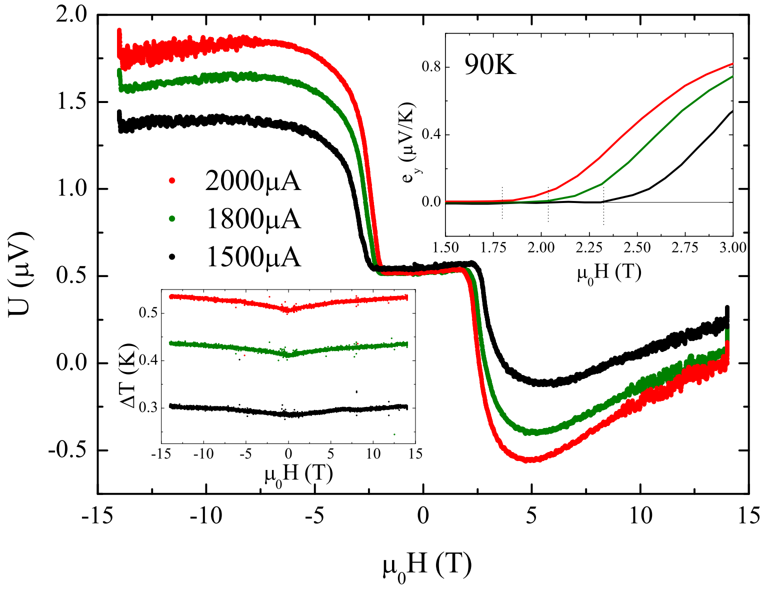

Figure 5.5: Effect of different chip heater currents on the sample temperature at a base temperature of 90 K. The upper right inset shows the result of the sample heating on the Nernst signal causing slightly shifted melting fields. The lower left inset depicts $\Delta T(B)$ for the three denoted currents. $\Delta T(B)$ is symmetric and resembles the field dependence of the thermal conductivity.

and 0.5 T/min.

5.2 Data analysis

5.2.1 Extracting the Nernst signal

The desired quantity to analyze is the Nernst signal, given by

$$e_y = \nu B_z = \frac{E_y}{-\nabla T_x}, \tag{5.1}$$

where ν is the Nernst coefficient and E denotes the electric field. The single steps from the raw signals measured by the voltmeters to the Nernst signal in (5.1) are the following. The outcome of a typical run for the Nernst setup is the raw voltage shown in Fig. 5.7. The Nernst voltage is extracted as the antisymmetric part of the magnetic field dependent transverse voltages ($U_N(-B) = -U_N(B)$) in order to eliminate thermopower voltages due to possible misalignments of the contacts. Of course, the thermopower voltage is field-symmetric, $U_N(-B) = U_N(B)$. Equation (5.1) is written as

$$\nu B_z = \frac{U_y}{-\Delta T_x} \frac{l}{b}, \tag{5.2}$$

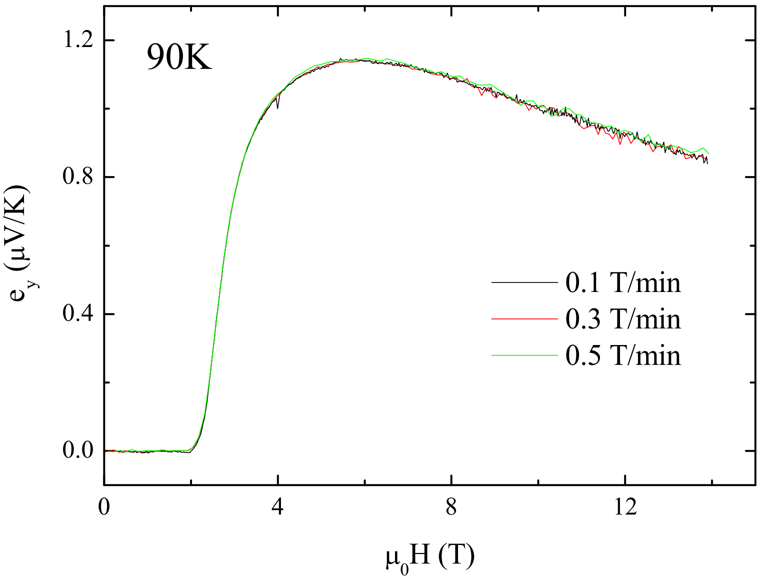

Figure 5.6: Independence of Nernst effect on sweep rate beween 0.1 T/m and 0.5 T/m, shown for three different rates. Measured at 90 K (on an optimally doped $NdBa_2Cu_3O_{7-\delta}$).

with l the distance of the ends of the thermocouple and b the distance between the Nernst contacts. $U_y/\Delta T_x$ is calculated as

$$\frac{U_y}{\Delta T_x} = [\frac{U(-B)}{\Delta T(-B)} - \frac{U(B)}{\Delta T(B)}]/2. \tag{5.3}$$

The black curve in Fig. 5.7 shows that pinning occurs between about -3 and 3 Tesla in this sample ($NdBa_2Cu_3O_7$, at 90 K). The raw voltage of the Nernst contacts is very close to zero in the pinning regime, indicating that the thermopower offset voltage of the wires is small and symmetric. Apparently the Nernst contacts are nearly at the same temperature. Not so with the thermopower contacts. The vortex signal of the thermopower should also be strictly zero at fields lower than the melting field. The offset voltage that is clearly seen in this regime resembles the thermopower of the copper wiring that is temperature and magnetic field dependent. Thus, $S_{wires}(T, B)$ has been calibrated independently [172] and is added to the measured signal. This operation has been performed for every thermopower data shown in this thesis,

$$S_{meas}(T, B) = S_{tp}(T, B) + S_{wires}(T, B). \tag{5.4}$$

Additionally, and depending on the misalignment of the thermopower contacts, a sizable Nernst voltage might add to the measured raw voltage of the thermopower. This situation is presented in Fig. 5.7 by the red curve. One can clearly see that the signal is not symmetric in B. Thus, the signal has to be symmetrizised by

$$\frac{U_{sym}}{\Delta T} = \frac{U(-B) + U(B)}{2\Delta T(B)}, \tag{5.5}$$

This operation is performed on every measurement in temperature regimes where sizable Nernst effects are present. This is usually not the case for $T \gg T_c$ in the high-T_c's presented here, but has to be individually analyzed for each different sample. The outcome for the thermopower is then given by,

$$\frac{U_{sym}}{\Delta T} = S \qquad \text{or} \qquad E = S\nabla T \tag{5.6}$$

The results of the various symmetry operations are presented in Fig. 5.8. The antisymmetric part of the thermopower contacts, which is a Nernst voltage due to misalignment of the thermopower contacts itself can easily be scaled to the voltage of the Nernst contacts. So one can estimate that the two points between which the thermopower develops are not perfectly aligned with the direction of the temperature gradient. They have a horizontal offset of 1/4 of the length of the distance of the Nernst contacts. As mentioned before the thermopower on the Nernst contacts is very small, indicated in Fig. 5.8 by the curve denoted with “Nernst symmetric”.

5.2.2 Sign conventions

The sign of the Nernst signal is not intrinsically related to the sign of the charge carrier. In the simplest case of a one band metal with a spherical Fermi surface the sign of the Hall and the Seebeck effect reveal the sign of the charged carriers involved. They are defined positive for hole-like carriers, as introduced by Gerlach [173]. In such a case, the Nernst voltage is subject to a cancellation described in detail in chapter 3.2. Fortunately, for the vortex Nernst signal a sign convention is provided. Vortices always diffuse down the temperature gradient, from the hot to the cold end. This is due to their finite entropy in the normal state cores. Thus, the Nernst signal is treated as positive if it is consistent with vortex movement [9]. For more complex physical systems, e.g. complicated Fermi surfaces or multiple charge transport channels, the intimate relation between the sign of quantities like the thermopower and the sign of the charge carrier is not defined unambiguously. Sign changes can also occur due to changes of slope of the energy derivative of the conductivity at the Fermi energy, as indicated by the Mott formula (3.3).

5.2.3 Error analysis

General

In this section the sources of errors concerning the measurements of the Nernst effect and the thermopower will be discussed. The typical way of bringing the contacts on the sample is already shown schematically in Fig. 5.2. Systematic errors that mainly concern the heat transfer through all the assembled parts of the sample are described in detail in [171]. In order to avoid a heating of the whole sample while trying to establish a stable temperature gradient, the coupling from the bottom of the sample to the sample platform of the measuring insert is the most sensitive part. If not mentioned otherwise,

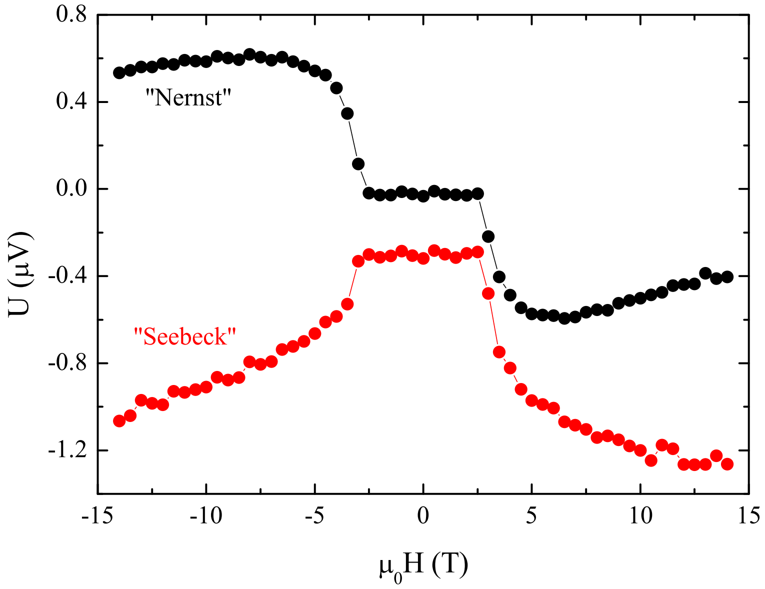

Figure 5.7: Raw voltage of transversal (Nernst, black curve) and longitudinal (Thermopower, red curve) contacts, at 90 K ($NdBa_2Cu_3O_7$). The offset of the thermopower from 0 in the pinnig regime (-3 T to 3 T) comes from the thermopower of the wiring which has to be added (see text). One can clearly see by eye that also the thermopower is not perfectly symmetric because of a superimposed Nernst voltage.

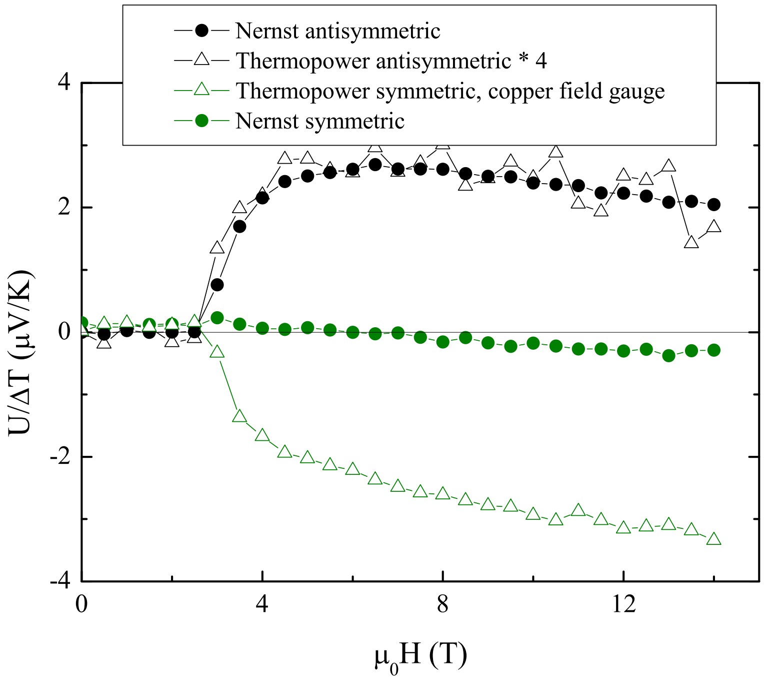

Figure 5.8: Symmetric and antisymmetric parts of the both contacts types, longitudinal (thermopower) and transversal (Nernst). The antisymmetric part of the thermopower can be scaled to the antisymmetric part of the Nernst voltages and vice versa.

all samples prepared in this thesis are glued to the platform via silver epoxy or conductive silver lacquer and are electrically insulated by a small piece of sapphire between sample and table. Sapphire has thermal conductivities of the order of 3000 W/Km at 30 Kelvin, which is comparable to copper.

Misalignments and geometry

Depending on the sample size and therefore the distance of the contacts, an error due to misalignments is by far the biggest source of error to the absolute values of the measured quantities. A misalignment of the contacts itself leads to - at least in the systems that are relevant for this thesis - an additional voltage. That is, a Nernst voltage can be superimposed by a thermopower and vice versa. This problem can easily be overcome by measuring in positive as well as in negative magnetic fields and then to extract the field symmetric part (thermopower) and the antisymmetric part (Nernst voltage) of the signal. What leads to an uncertainty in the absolute values of these quantities is the uncertainty of the exact distance the voltage develops between. As illustrated in Fig. 5.9 the measured distance between the contacts, b, might not be the distance over which the actual voltage develops. The real distance may lie somewhere within the spread of the contact, y and remains indeterminable. Only the ratio of the antisymmetric and the symmetric part can be determined. So whenever the sample size is so small that the dimension of the contact itself is of the order of the distance between the contacts, the maximum possible error already exceeds 100%. A detailed analysis for one of the smallest samples leads to a maximum error of $\simeq$ 160%. Since this estimation resembles the worst case, a comparison of the absolute values derived in this work to those obtained on the same compounds by other groups gives a better feeling of the tolerance of this quantity. As shown in the next paragraph, the difference between two $La_{2-x}Sr_xCuO_4$ (x=0.07) samples (one measured by Wang *et al.,* Fig. 5.11, and one by myself, Fig. 5.10) reveals a tolerance of about 30%.

A similar error estimation applies for the line-like contacts of the thermopower, the maximum distance is also just two times the width of the contacts, x, plus l (Fig. 5.9). In all cases, the geometric error would lead to an overestimation of the electric field strength since the voltage is divided by a length that might be too short.

5.2.4 Nernst effect calibration in $La_{2-x}Sr_xCuO_4$

In this section, Nernst effect and Seebeck measurements in $La_{2-x}Sr_xCuO_4$ for $x = 0.07$ and $x = 0.15$ are presented. The main purpose was to test the methods of measuring transverse thermomagnetic effects in a system that was widely studied mainly by the group of N.P. Ong, [4, 9, 25]. In Fig. 5.10, the temperature and field dependences of the Nernst signal are shown. The upper right panel can be directly compared to measurements published in [9] for a sample with $x = 0.07$ and nominally the same T_c of 11 K. In this sample, the hole concentration is just sufficient to enter the superconducting dome in the phase diagram in the left panel of Fig. 5.11. Despite the difference in the absolute values of the Nernst signals that is well within the error due to contact geometries (see

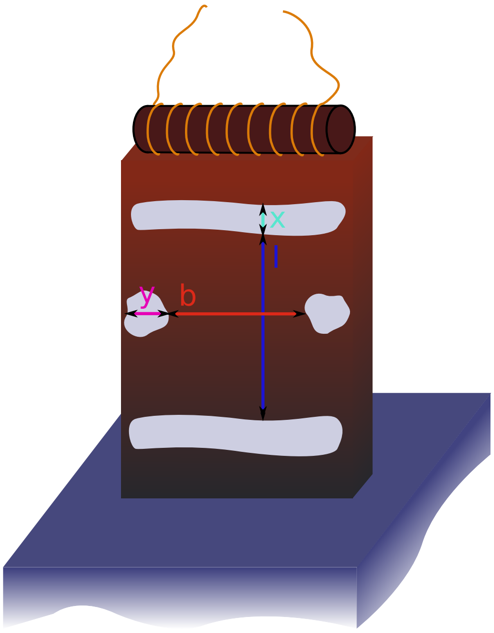

Figure 5.9: Geometry error estimation for the Nernst and the thermopower contacts, mainly caused by the spreading of the silver epoxy glue to some area around the wires. The smaller the samples, the larger the possible maximum error.

section 5.2.3), the results shown in the right panel of Fig. 5.11 and the upper right panel of Fig. 5.10 well agree with each other. Due to the low T_c, pinning is not observed in the temperature range shown here. The Nernst signals of Fig. 5.10 are linear in B until the temperature drops below 30 K. Upon a further reduction of the temperature, $e_N(B)$ gains more and more curvature and the slope at low fields gets steeper. An eye-catching feature is the smooth crossover to temperatures below T_c as also present in the right panel of Fig. 5.11. Turning to the temperature dependence of e_N at fixed fields, a maximum appears around T_c (left panel of Fig. 5.10). Towards lower temperatures, the absolute values of the signals slowly diminish as can also be seen in the field dependence of Fig. 5.11(right panel). Not only the smooth crossover but also the ability to detect those Nernst signals to very high temperatures compared to T_c lead to various investigations whether this behavior is connected to the pseudogap (see also chapter 4.4) or other phase separation scenarios. Although the onset of the Nernst signal is hard to analyze due to cumulative noise in the temperature dependence of e_N (left panel of Fig. 5.10) at higher temperatures, a look at the curve $e_y(T, 14\text{T})$ makes one sense that the signal lasts at least up to 80 K since it is clearly distinguishable from the curves measured at 100 K and 150 K. Compared to the onset line of Fig. 5.11(left panel) at $x = 0.07$, 80 K is roughly the temperature detected as the onset by Wang *et al.* [9].

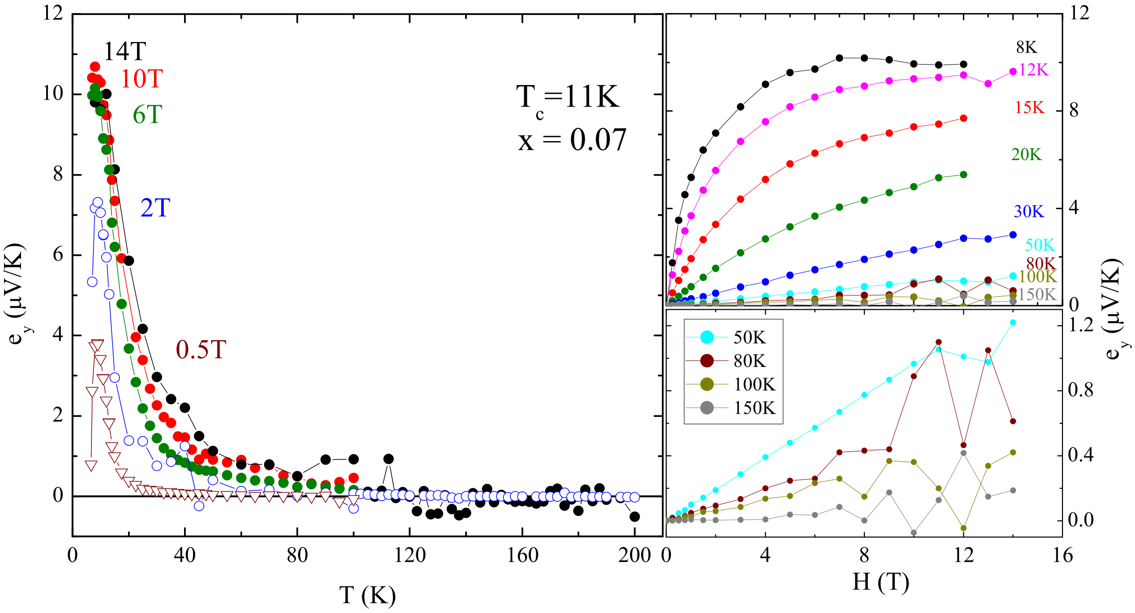

Figure 5.10: Temperature dependence of the Nernst signal in $La_{1.93}Sr_{0.07}CuO_4$ for the denoted magnetic fields. The right upper panel depicts the field dependence of the signal. A magnification is shown in the lower panel for the field dependence of higher temperatures.

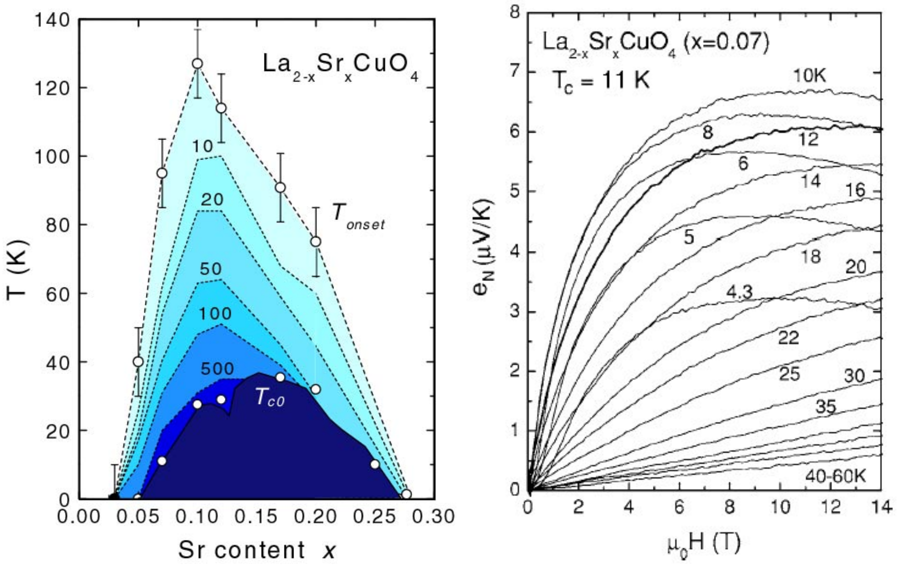

Figure 5.11: Left panel: Phase diagram of $La_{2-x}Sr_xCuO_4$ together with contour lines of the onset of the Nernst signal and several thresholds in units of nV/KT. The right hand side shows the magnetic field dependence of the Nernst signal in $La_{1.93}Sr_{0.07}CuO_4$, take from [9].

6 Motivation

One starting point for the investigations presented here is the question: is the superconducting phase related to the pseudogap phase in high temperature superconductors? And as already mentioned by introducing the method of measuring the Nernst effect, it is one powerful tool to detect vortices or vortex-like excitations because it is very sensitive to the voltage produced by vortex movement. The existence of a vortex on the other hand presupposes the presence of a non-zero superfluid density. Thus, to define a vortex, a substantial superfluid density should be in its vicinity. The search for this vortex Nernst signal over a wide temperature range above T_c was the goal, when systematic investigations in the cuprate superconductor $\mathrm{La}_{2-x}\mathrm{Sr}_x\mathrm{CuO}_4$ [4] began. And indeed the unexpected result was obtained that vortex Nernst signals persist easily up to temperatures as high as twice T_c. One such measurement is shown in Fig. 6.1 in the left panel. The Nernst voltage that corresponds to T_c is marked in red and clearly displays a large, positive and curved signal. The Nernst signal that is taken at 60 K is marked in blue and still shows a considerable $0.5\,\mu$V/K at 14 T. These results suggest that the pairing amplitude of the Cooper-pairs remains up to very high temperatures above T_c. The smooth crossover of the Nernst signal through the superconducting transition is another supportive argument of vortex-like excitations above T_c. This feature is present in nearly all examined high-T_c compounds [9] as well as in some low-T_c superconductors [176]. Early calculations for the cuprates were already pointing towards this direction [177], the results of which being a direct challenge to the conventional BCS scenario. Furthermore, a strong diamagnetic signal in Bi2212 is found to persist at $T > T_c$. This is depicted in Fig. 6.2 in the left panel, denoted with (a) for an underdoped sample (T_c's are indicated by the dashed lines) and denoted with (b) for an optimally doped sample. Magnetization curves are in red. Since these diamagnetic signals scale with the Nernst effect (open symbols in (a) and (b) and additionally shown in the field dependence in (c)), this finding strongly supports the scenario that vortex-like excitations are still found at temperatures high above T_c. The right panel depicts another interesting implication of these high-field magnetization measurements. The upper critical field, which is defined by zero magnetization, is apparently not reduced to zero at T_c. In contrast, as is shown for optimally doped Bi2212 with $T_c = 86$ K, it persists to far above 40 T at T_c and even above [174, 175].

Consequently, the results of the anomalous high-temperature Nernst signals fed the investigations towards possible relations of such a “precursor state” to the pseudogap (see chapter 4.4). The whole doping range of the superconducting dome was scanned for Nernst signals above T_c as shown also in the right panel of Fig. 6.1. Although these signals were found in wide regions of the phase diagram, a direct relevance to the pseudogap is still not compelling. First of all, the onsets of the Nernst signals last only to about half the pseu-

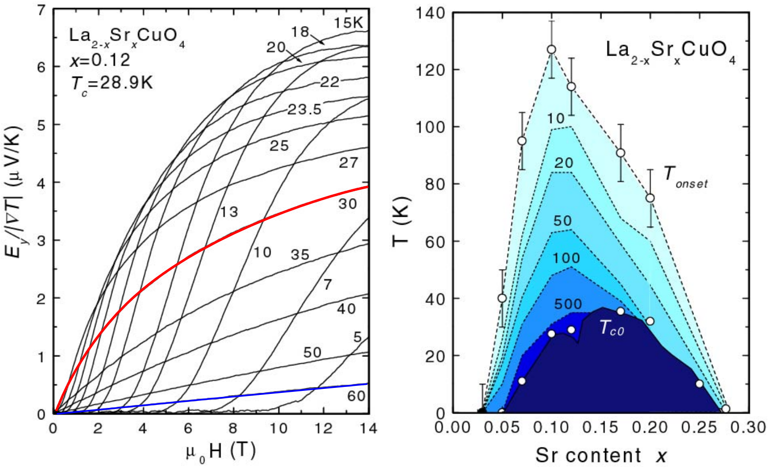

Figure 6.1: Left panel: Nernst signal in LSCO near optimal doping. The magnetic field dependent signal for the critical temperature $T_C \simeq 30\,\mathrm{K}$ is emphasized in red. The right panel displays a contour plot of the temperature (T_{Onset}) that correspond to the onset of a vortex-like Nernst signal. The numbers that denote the contour lines below are the values of the Nernst coefficient (e_N/B), that gradually increase towards T_c [9].

dogap temperature (T^*) in the extremest cases. Second, it is not directly obvious that the Nernst signal scales with T^* when considering all the investigated cuprate superconductors so far, see e.g. [141, 178]. A unique opportunity for further studying these questions is at hand with the system $\mathrm{NdBa_2(Cu_{1-y}Ni_y)_3O_{7-\delta}}$. It could be shown that doping Ni-impurities into the copper-oxygen sheets not only suppresses T_c but at the same time enhances the pseudogap [10]. The corresponding results of measurements of the optical conductivity are shown in Fig. 6.3. The pseudogap energy gradually increases when Ni ions are added into the sample, although the charge carrier concentration is not altered in this process. This was confirmed by thermopower measurements [10]. So the question whether the onset of the Nernst effect is related to either the pseudogap state and thereby unravel its connection to the superconducting phase can be directly addressed with measurements on a series of $\mathrm{NdBa_2(Cu_{1-y}Ni_y)_3O_{7-\delta}}$. Other investigations are mostly restricted to altering the hole content in an attempt to influence the pseudogap temperature. Doing so does not shift the pseudogap crossover line. Altering Ni concentrations in $\mathrm{NdBa_2(Cu_{1-y}Ni_y)_3O_{7-\delta}}$ does [10]. To stress the relevance of the measurements here, one can say we have three dimensional access to the cuprate phase diagram. Besides temperature and doping, the third axis is denoted by Ni-concentrations. Thus, the dome is tilted towards the surface defined by the temperature and Ni axis at 0 K. The pseudogap crossover line turns to a crossover surface with positive slope in direction of increasing Ni concentrations. An illustration of this interesting playground is given in Fig. 6.4.

Presented in this work are three charge carrier concentrations. An underdoped one with

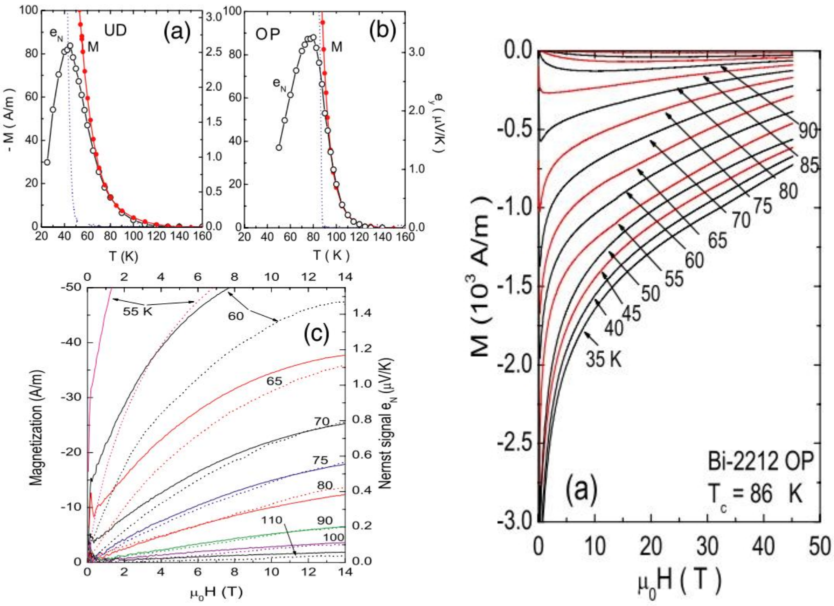

Figure 6.2: Left panel: Scaling of the Nernst signal (open symbols) and the negative magnetization (closed symbols) in underdoped (a) and optimally doped (b) Bi2212 as a function of temperature. (c) Same scaling for the underdoped sample above $T_c = 50\,\mathrm{K}$ as a function of the magnetic field. Right panel: High-field magnetization in the optimally doped Bi2212. From [174, 175].

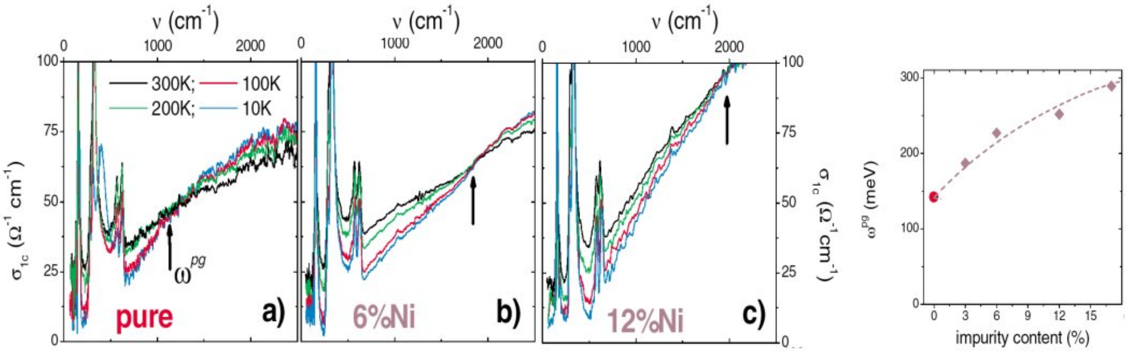

Figure 6.3: Optical conductivity of $\mathrm{NdBa_2\{Cu_{1-y}Ni_y\}_3O_{6.8}}$ for the denoted Ni concentrations. Arrows indicate the energy that is related to the opening of the pseudogap which is found to be enhanced with increasing Ni concentration, from [10].

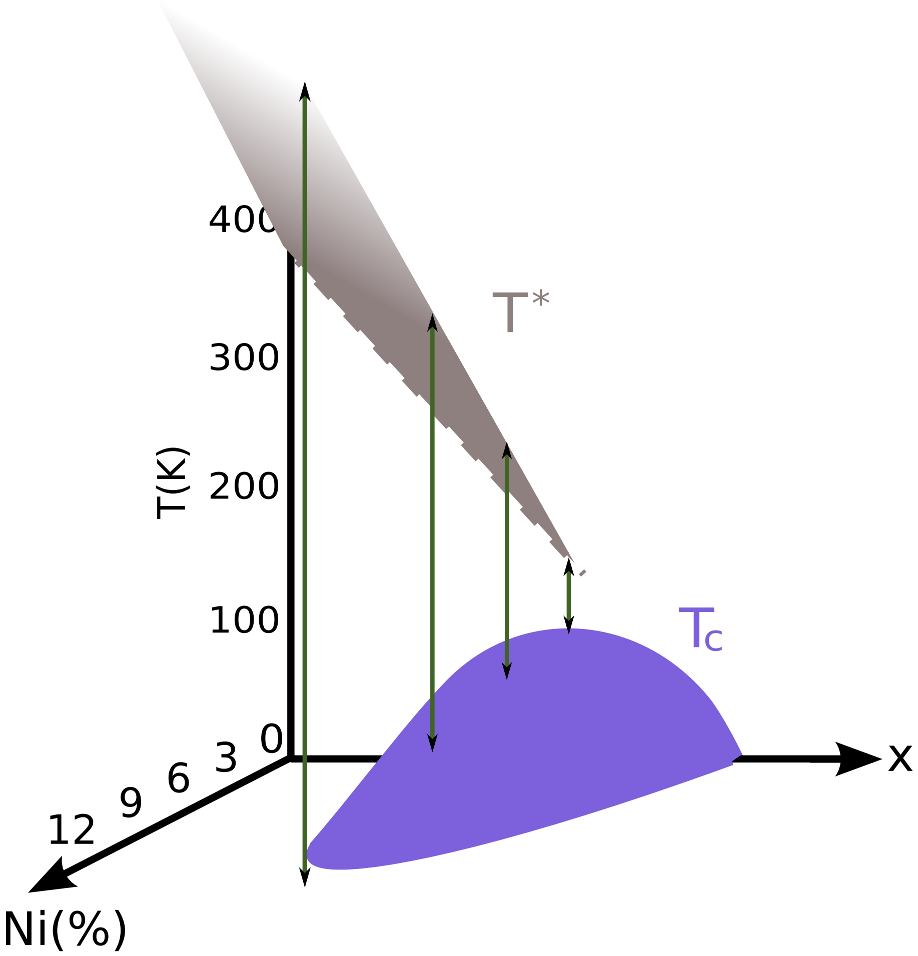

Figure 6.4: 3D sketch that emphasizes the simultaneousness of the T_c depression and the enhancement of the pseudogap, T^*, based on the results of [10]. The T_c depression due to increasing concentrations of Ni-impurities is indicated by the tilted 3D-dome. The pseudogap crossover temperature is indicated by the gray surface. The green arrows exemplary denote the region that is scanned for vortex Nernst voltages between T_c and T^* for the optimally doped sample series.

an oxygen content of $O_{6.8}$, an optimally doped one with an oxygen content of O_7 and one in between, $O_{6.9}$. For each concentration, different Ni amounts have been inserted. These are varied from 0% to 12%. So in total, a profound amount of Nernst effect data that is measured from within the superconducting phase to high above it is presented. These data have strong impact to unravel the relation between the pseudogap and the superconducting phase. It is clear that clarifying this relation is of major importance to reveal the mechanism of high-temperature superconductivity.

7 Nernst Effect and Transport in Ni-doped $NdBa_2Cu_3O_{7-\delta}$

Figure 7.1 again shows the typical setup for a Nernst effect measurement. For the analysis of the Nernst signal, $e_y = -E_y/\nabla T$ the magnitude of the temperature gradient is needed. Therefore, measuring the thermal conductivity is an automatic add-on to the Nernst effect configuration. Just a little bit of additional effort is required to also measure the Seebeck effect: adding the longitudinal electric contacts to the sample. So, since all Nernst effect measurements are taken out in this typical setup, the thermal conductivity and the Seebeck effect were gathered at the same time. Therefore, this chapter presents the investigation of those thermal transport properties on a series of $NdBa_2\{Cu_{1\text{-}y}Ni_y\}_3O_{7-\delta}$ with y=0-0.12 and $\delta = 0{,}0.1{,}0.2$ in wide temperature range and in magnetic fields up to 14 T. Of course, as is made clear in the motivation, the Nernst effect was endowed with the highest priority. So it came to situations in which the longitudinal voltage suffered resolution problems which are mostly caused by "bad" electrical contacts, while the Nernst voltage was intact. In such a case the sample was not subject to the whole contact preparation process (see section 5), again. The contact preparation for the transverse electrical contacts alone was a very challenging task. The results of samples that are presented in this work are the distillate of approximately the threefold amount of tries either on the same or other samples that did not yield the desired quality. Moreover, the temperature and field ranges of the measurements were dictated by the Nernst effect. For example, only few data points were taken in the vortex-lattice region; i.e. at low T and low B, since $e_N = 0$ although κ could be measured in that region.

In order to make the action rising, the order of the presentation of the transport quantities is as follows: First, the thermal conductivity is shown. The second part is represented

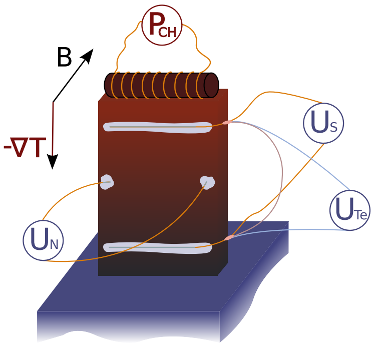

Figure 7.1: Contact scheme:
U_N → Nernst effect,
U_S → Seebeck effect,
U_{Te} → Thermal conductivity.

by the Seebeck effect and finally, as the climax of this chapter the Nernst effect is presented.

The measurements here were carried out on four optimally doped $\mathrm{NdBa_2\{Cu_{1-y}Ni_y\}_3O_7}$ samples. The T_c values and transition widths, ΔT_c are taken as the midpoint of the diamagnetic transition and the 10-90% width of the transition. The width is denoted in brackets. These optimally doped samples are comprised of a pure sample (y=0) with $T_c = 95(\Delta T_c = 1)$ K, and three samples with Ni impurity contents of y = 0.03, 0.06, 0.12. The corresponding critical temperatures are $T_c = 59(8)$ K, 45(10) K and $T_c < 2$ K, respectively. By annealing the identical samples or samples from the same batch in flowing O_2 atmosphere at about 540°C and P=1 bar a series of underdoped ($O_{6.8}$) samples were prepared: y = 0 with $T_c = 53(7)$ K, y = 0.03 with $T_c = 20(14)$ K and y = 0.06 with $T_c < 2$ K. Additionally, a second series of underdoped samples with oxygen contents of $O_{6.9}$ were prepared by annealing two optimally doped crystals again under oxygen atmosphere (1 bar) at 466°C for 160 hours. These two samples (y = 0, 0.03) have transition temperatures of $T_c = 82(5)$ K and 38(8)K, respectively. Detailed information about the chemical preparation process is given in [139]. Typical sample sizes are 1 mm×1 mm×0.5 mm.

7.1 Thermal conductivity

7.1.1 Introduction

A crystal's thermal conductivity can be expressed in general by the equation [69]

$$\kappa = \frac{1}{d} cvl, \tag{7.1}$$

with d the dimensionality, c the specific heat, v the group velocity and l the mean free path of the heat carrying excitations. The relevant channels that can contribute are phonons, electrons and partly magnons, depending on the observed systems. The phononic specific heat contribution can be treated within the Debye model for temperatures below the Debye temperature and is subject to various textbooks [69]. The mean free path of the excitations in the low temperature regime is mostly determined by scattering processes at the crystal surface [148]. So in this limit κ follows the T^3 dependence of the specific heat. Umklapp processes in phonon-phonon interactions dominate the mean free path at higher temperatures and the specific heat approaches the temperature independent Dulong-Petit value. The number of excited phonons is then proportional to the temperature and it follows $l \propto 1/T$ and thereby $\kappa \propto 1/T$.

The electronic contribution to the specific heat is proportional to $k_B T$, leading to an expression for the electronic thermal conductivity of [69]

$$k_{el} = \frac{\pi^2 n k_B^2 T l}{3 m v_f}, \tag{7.2}$$

with m, n, v_f the electron mass, their density and the Fermi velocity, respectively. Because electrons carry heat and charge, in the limits of elastic scattering processes a simple relation

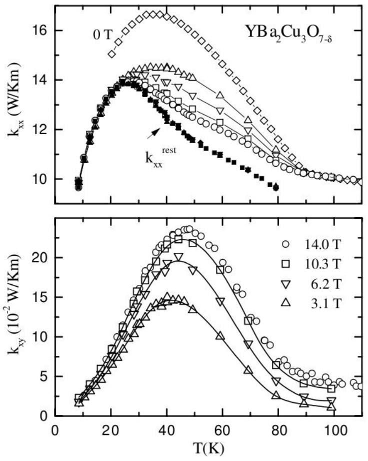

Figure 7.2: Thermal conductivity in $YBa_2Cu_3O_{7-\delta}$. Upper panel: longitudinal thermal conductivity in magnetic fields ranging from 0 to 14 T. κ_{xx}^{rest} is the field independent sum of the phononic contribution and a contribution due to the quasi-one-dimensional CuO-chains. Lower panel: Magnetic field dependence of the transverse thermal conductivity. From [36].

between the thermal and the electronic conductivity exists:

$$\kappa = L_0 \sigma T. \tag{7.3}$$

This is the well known Wiedeman-Franz law. The value of the Lorenz number L_0 is determined from free electron gas theory to $L_0 = 2.45 \cdot 10^{-8}\,\mathrm{W}/\Omega\mathrm{K}^2$.
High temperature superconductors show characteristic features such as the steep rise of the thermal conductivity with increasing temperature for temperatures lower than T_c, reaching a maximum at approximately $T_c/2$ followed by a decrease and a kink at T_c [179]. Within the physics of the Wiedemann-Fraz law, Eq. (7.3) an estimation of the ratio of electronic contributions and phononic contributions in $YBa_2Cu_3O_{7-\delta}$ yields about 50% for each channel within the *ab* planes while the out-of-plane thermal conductivity is four to five times smaller and does not show the sub T_c maximum [180]. The results lead to a microscopic picture where strong in-plane electron-phonon scattering limits the dominating phononic thermal conductivity for $T > T_c$. The distinct characteristics of the electronic and the phononic contributions below T_c are shown in Fig. 7.2. According to Zeini *et al.* [36] the longitudinal thermal conductivity consists of three different channels: $\kappa_{xx} = \kappa_{xx}^{el} + \kappa_{xx}^{ph} + \kappa_{xx}^{ch} = \kappa_{xx}^{el} + \kappa_{xx}^{rest}$. κ_{xx}^{ph} denotes the phononic contribution and κ_{xx}^{ch} is a contribution due to the quasi-one-dimensional CuO-chains. The quasiparticle contribution κ_{xx}^{el} is strongly enhanced below T_c and responsible for the magnetic field dependence of the longitudinal heat conductivity.

7.1.2 Data and analysis

All shown curves in this section are measured along the twinned *ab* planes with magnetic fields ranging from 0 to 14 T applied parallel to the c axis. Measurements in zero field that are shown up to room temperatures are mostly derived from the first cooling down procedure of the whole setup (“top-down” measurement). Those curves are, of course, only shown if they are consistent with the measurements that were performed after the cooling. Since κ_{xy} (Righi-Leduc effect) is roughly of the order of 1% of κ_{xx} [36] for $YBa_2Cu_3O_{7-\delta}$(assuming the same holds for $NdBa_2\{Cu_{1\text{-}y}Ni_y\}_3O_{7-\delta}$), it is not necessary to symmetrizise κ here. κ is then derived by applying electrical power $(U_H \cdot I_H)$ to the heater on top of the sample, heating the cross section A. The resulting temperature difference taken at a distance l is picked up by a thermocouple which produces a corresponding voltage U_{TE}, which is corrected by offset voltages. The voltage is transformed into a temperature gradient by dividing by the temperature- and field-dependent thermopower of the thermocouple, $S(T,B)$ [171]. The thermal conductivity is then calculated as

$$\kappa = \frac{U_H I_H S(T,B)}{U_{TE}} \frac{l}{A}. \tag{7.4}$$

Error sources due to geometric errors are discussed in Section 5.2.3. Additional error sources that mostly affect measurements of thermal conductivities are systematic ones like thermal shortcuts through the wiring or radiation losses at higher temperatures [171]. A detailed analysis of radiation losses through the surfaces of the sample, the heater and the surface of the wires is given in [148]. The larger the ratio l/A, sample length to heated cross section, the more loss due to radiation can be expected. This additional term is proportional to T^3 and adds to real thermal conductivity of the sample so that the measured one is too high, $\kappa_{Measure} = \kappa_{Sample} + \kappa_{Radiation}$. An estimation of radiation losses at room temperature is also given in [148] for several compounds and different conditions. Consequently, a severe loss would be visible in an upturn of κ at high temperatures, which is not the case in the measurements presented here. The characteristics of κ (0% Ni) in

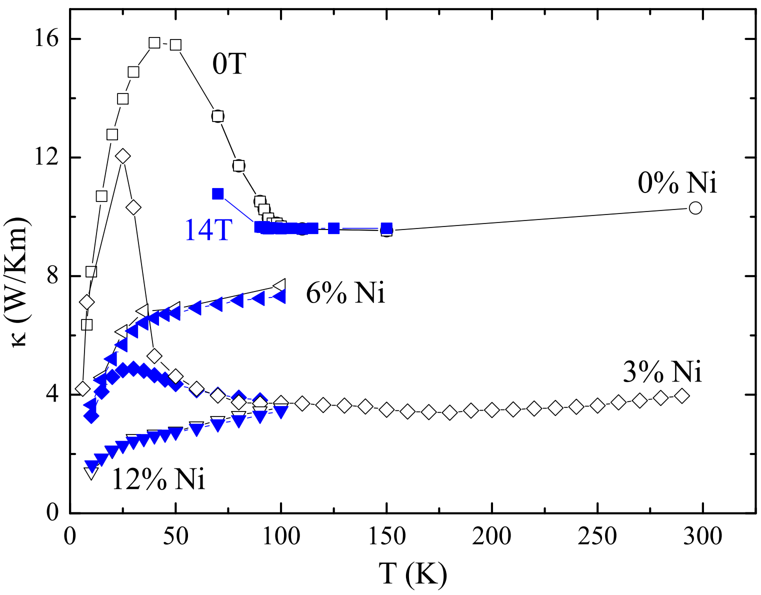

Figure 7.3: Thermal conductivity of $NdBa_2(Cu_{1-y}Ni_y)_3O_7$, for y=0% (open circles and open squares), y=3% (open diamonds), y=6% (triangles left) and y=6% (triangles down). Solid symbols represent the corresponding $\kappa(T, 14T)$.

Figure 7.3 clearly resembles the general trend described above for other high temperature superconductors like $YBa_2Cu_3O_{7-\delta}$. Only a weak temperature dependence of κ measured within the *ab* planes can be detected coming from room temperature to T_c. Here, a kink occurs, the thermal conductivity starts to rise until a maximum is reached at about $T_c/2$. The ratio of the corresponding values of κ is determined to $\kappa(T_{max})/\kappa(T_c) \simeq 1.6$. This is consistent with previous results [36, 181, 182]. Towards lower temperatures, κ is falling steeply into the direction of $\kappa = 0$. The absolute values of the maximum of the thermal conductivity of about 16 W/Km agree with those reported in literature for optimally doped $YBa_2Cu_3O_{7-\delta}$. Values range from 7 W/Km (polycrystalline $YBa_2Cu_3O_{7-\delta}$, [183]) through about 15 W/Km for single crystalline twinned $YBa_2Cu_3O_{7-\delta}$[36, 180, 184] to values exceeding 25 W/Km in detwinned samples along the *a* and *b* directions [181]. The solid symbols in Fig. 7.3 are measurements under the influence of an externally applied magnetic field of 14 T. In the Ni-free sample a magnetic field strongly suppresses the steep rise of the thermal conductivity, as indicated by κ(70K, 14T). Such a suppression of the characteristic maximum is reported in many publications [35, 36, 185, 186]. Assuming that κ can be written as the sum of an electronic and a phononic contribution, the tensor κ_{ph} is assumed to remain diagonal also in the case of $B \neq 0$ and field insensitive [36, 186]. Since no field dependence is observed in the normal state and the electronic longitudinal contribution is found to be very sensitive to magnetic fields, an additional scattering mechanism is discussed, such as the scattering of quasiparticles on vortices [187–189]. An assumption for the corresponding scattering rate, τ_ν^{-1}, would be to scale with the number of vortices and thereby to the magnetic field, as could be shown by Zeini *et al.* [36].

Introducing Nickel into the sample shifts the absolute values of the high temperature part to ~4 W/Km. The maximum for $T < T_c$ is still present but also shifted to lower temperatures according to the drop of T_c from 95 K to 59 K (for 3% of Nickel). A concentration of 6% of Nickel drastically changes the shape of the temperature dependence although the sample is still superconducting with $T_c \approx 45$ K. No peak in the superconducting regime is present anymore and κ turns to zero with a positive slope, roughly beginning at T_c. The field dependence has simultaneously vanished. Similar behavior was reported for Zn doped $YBa_2Cu_3O_{7-\delta}$ [183], giving the assumption that impurities reduce the superconducting energy gap. Adding 12% of Nickel, the change in the slope is further broadened and the overall conductivity is further reduced. As the thermal conductivity has no field dependence in the normal state of all measured samples, the suppression of the superconducting phase also frees the sample $T_c < 2$ K from its field dependence.

Changing the carrier concentration in the direction of the underdoped regime to the sample series $NdBa_2\{Cu_{1\text{-}y}Ni_y\}_3O_{6.9}$, κ qualitatively shows similar features as previously described for the optimally doped sample. Although the data was only recorded down to 60 K ($T_c \approx 82$ K) the change in the slope leading to the maximum at $T_c/2$ is still present as well as the suppression by the magnetic field as pictured in Figure 7.4. Quite similar to the characteristics of κ for 0 and 6% Ni in the optimally doped sample, the peak is nearly suppressed here ($T_c \approx 38$ K). As observed before, the field dependence is strictly connected to the development of this peak in the superconducting phase.

Figure 7.5 presents the data acquired for a sample with the oxygen content further re-

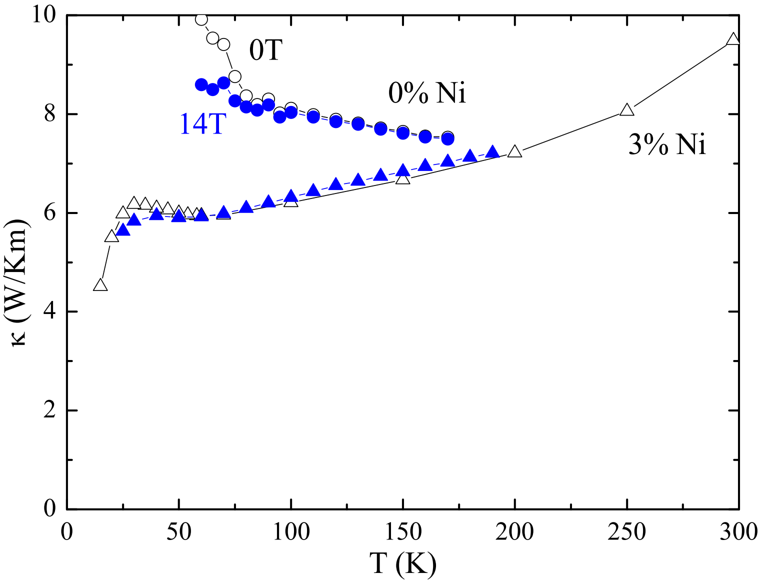

Figure 7.4: Thermal conductivity of $NdBa_2(Cu_{1-y}Ni_y)_3O_{6.9}$, for y=0, 3%. The associated field curves are indicated by solid symbols.

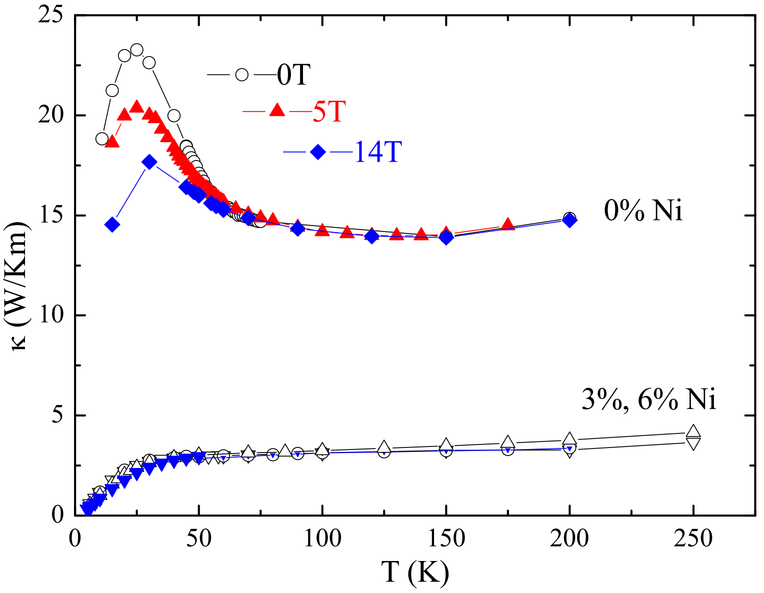

Figure 7.5: Thermal conductivity of $NdBa_2(Cu_{1-y}Ni_y)_3O_{6.8}$, for 0, 3% and 6% of Nickel.

duced to $O_{6.8}$ ($T_c \approx 53\,\mathrm{K}$). This sample shows the highest absolute values of $\kappa \approx 23\,\mathrm{W/Km}$. The typical peak structure at $\sim T_c/2$ is also present. Magnetic fields of 5 and 14 T are able to gradually suppress the magnitude of this peak. The samples prepared with 3% ($T_c \approx 20\,\mathrm{K}$) and 6% ($T_c < 2\,\mathrm{K}$) Nickel are following similar temperature dependences without any peak structure. Consequently, magnetic fields are ineffective.

As an overall tendency, increasing Ni-concentrations lead to a strong suppression of κ. Furthermore, the peak structure, that was present at low Ni-concentrations is suppressed as well. Since this peak is the only feature that shows a pronounced magnetic field dependence, Ni subsequently leads to a suppression of the field dependence.

7.2 Seebeck effect

7.2.1 Introduction

Zero magnetic field

The development of a thermopower in a superconductor differs in some important points from conventional conductors. The experimental setup is the same, of course. A temperature gradient is applied across the sample to which entropy carrying particles react by moving from the hot to the cold end. If these particles also carry charge, the resulting accumulation of opposite charges at opposite ends of the sample leads to an electric field which in turn exerts a force on all charged particles in the reverse direction. These two forces will balance and the resulting electric field is measured under these stationary conditions, called "steady state". In a superconductor, in the regime $T < T_c$, only normal excitations carry heat and diffuse down the temperature gradient. A current density of normal particles is setup by

$$\mathbf{j}_n = \alpha \nabla T, \tag{7.5}$$

with $\alpha = S\sigma$ being the Peltier coefficient as the product of the thermopower and the normal state conductivity. A compensating supercurrent $\mathbf{j}_s$ is set up as immediate response [190, 191]. Since no overall current is allowed to flow through the sample, $\mathbf{j} = \mathbf{j}_s + \mathbf{j}_n = 0$ follows. The compensating supercurrent immediately explains why it was long believed that there are no thermoelectric effects in superconductors. A voltmeter will never be able to pick up voltages as long as they are shunted by the supercurrent [72].

Finite magnetic field

Applying a magnetic field to the sample changes the situation in the way that voltages below T_c can now be measured because moving vortices effect an electric field via $\mathbf{E} = \mathbf{v} \times \mathbf{B}$, as described in sections 4.2.1 and 4.2.5. With increasing field strength the superconducting transition gets broadened similar to the resistive transition due to the energy that is dissipated by the vortex movement. As already discussed in section 4.1.2 regarding the Nernst effect, field dependent measurements of the thermopower also show pinning effects which are manifested as a zero signal until a certain "melting field" is reached.

7.2.2 Data and analysis

Normal state thermopower

Fig. 7.6 shows $S(T)$ of $NdBa_2Cu_3O_{7-\delta}$ in zero magnetic field for different oxygen contents $\delta \sim \{0, 0.1, 0.2\}$. The first striking feature that catches the eye is the sign change between the fully oxygenated sample $\delta \approx 0$ and the next sample that contains some holes less ($\delta \approx 0.1$). A similar behavior is reported for $YBa_2Cu_3O_{7-\delta}$ samples [129, 192–194], shown in Fig. 7.7. Here the sign change is found to coincide with δ corresponding to the maximum of T_c [192]. Cooper *et al.* argue that at least for low δ the high-temperature magnitude

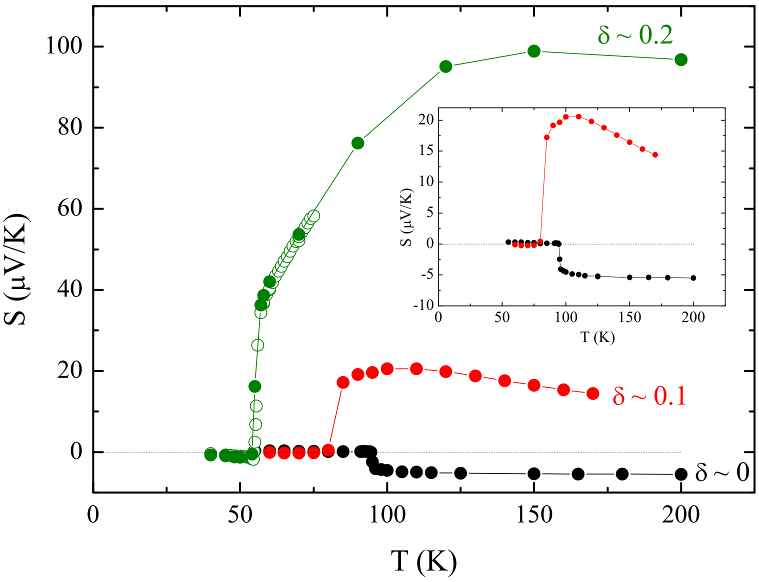

Figure 7.6: Temperature dependence of the thermoelectric power of $NdBa_2Cu_3O_{7-\delta}$ for different values of δ, in the $a-b$ planes. Open symbols are derived by taking the zero field value of several field dependent measurements at stabilized temperatures.

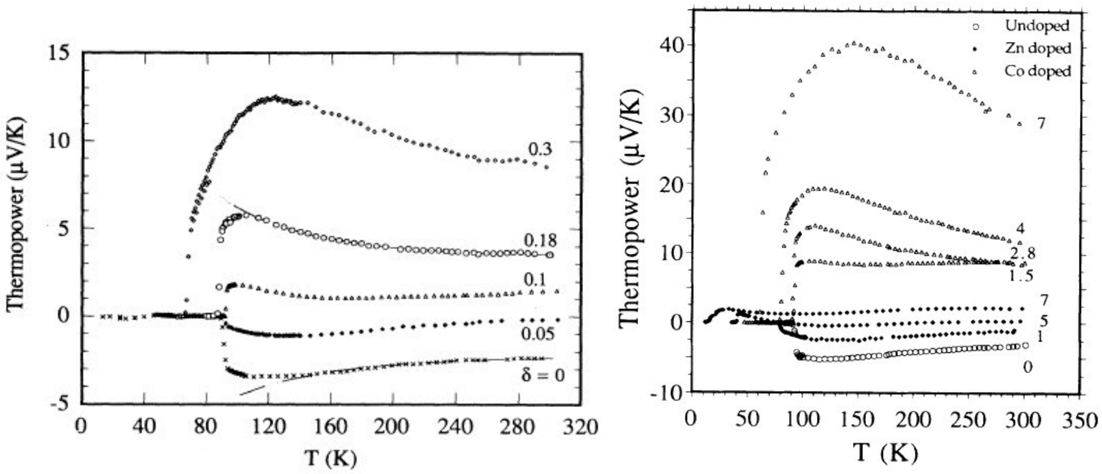

Figure 7.7: Left panel: S(T) of $YBa_2Cu_3O_{7-\delta}$ for several oxygen concentrations, from [192]. Right panel: S(T) of $YBa_2(Cu_{1-x}M_x)_3O_{7-\delta}$, for M=Zn,Co. Various concentrations of x(%) are shown in comparison to pure underdoped samples, from [129].

and the sign of the thermopower are a sensitive empirical guide to the degree of order and purity of the CuO chains. The magnitude in this range is usually very small, i.e. of order $5\,\mu$V/K and is consistent with the observation of the highest electrical conduction at the same oxygen doping. $NdBa_2Cu_3O_7$, represented by the black solid circles of Fig. 7.6 (see magnification in the inset) is in very good agreement with these observations. It shows the negative sign, the same magnitude and a nearly constant high-temperature contribution. The standard explanation for the negative thermopower for very low δ is that the CuO chains contribute negatively to the whole signal and at $\delta = 0$ even dominate. This negative contribution is then more and more suppressed as oxygen is removed from the chains. This picture is supported by thermopower measurements in untwinned single crystals of $YBa_2Cu_3O_{7-\delta}$ along the a and the b axis, where only the thermopower measured along b is found to be negative [195]. However, the sign change has been found also in other systems, $Y_xCa_{1-x}Sr_2(Tl_{0.5}Pb_{0.5})Cu_2O_7$ [196] and $Bi_2Sr_2CaCu_2O_{8+x}$ [129], suggesting that the relation could also be due to the properties of the CuO_2 planes at particular doping levels alone.

Changing δ to 0.1 changes the sign and drastically enhances the magnitude of $S(T)$ as also depicted in the inset of Fig. 7.6. A very high value of about $100\,\mu$V/K is present in the sample with $\delta \sim 0.2$ corresponding to nonmetallic conditions although the superconducting transition takes place at relatively high 53 K. In contrast to $YBa_2Cu_3O_{7-\delta}$, $S(T)$ in $NdBa_2Cu_3O_{7-\delta}$ clearly displays a stronger dependence of T_c on the oxygen content. This is easy to see because $S(T)$ is strictly zero at $T \leq T_c$ in zero magnetic field. In $NdBa_2Cu_3O_{7-\delta}$, T_c is reduced to roughly $0.5 \cdot T_c$ when δ increases from $\delta \sim 0$ to $\delta \sim 0.2$. In $YBa_2Cu_3O_{7-\delta}$, an increase from $\delta \sim 0$ to $\delta \sim 0.18$ just effects a reduction of about $0.1 \cdot T_c$.

Fig. 7.8 depicts the thermopower for the optimally doped samples with different Ni-contents. These results are best analyzed in comparison to the Ni-free curve of Fig. 7.6. For 3% Ni, denoted by the red solid circles, the high-temperature values are still negative but have acquired a slope that changes sign at about 100 K, displaying a minimum. The transition into the superconducting state at $T_c \approx 60$ K is not at all as sharp as in the clean sample. It is rather broad in the vicinity of T_c and reaches zero at about 45 K. The absolute value of $S_{max}(T)$ has increased to $\sim -7\,\mu$V/K. Green curves represent a Ni-content of 6%. The solid green circles represent values that are derived from the zero field values of magnetic field dependent measurements at several fixed temperatures. Open green circles are values from a "top-down" measurement while open triangles represent the influence of a magnetic field of 14 T. From room to lower temperature, $S(T)$ is initially positive, crosses zero at about 200 K and reaches a minimum at 100 K as did $S(T, 3\%)$. It is flashy that these minima temperatures roughly correspond to T_c in the pure sample. $S(T, 6\%)$ then crosses zero again at about 60 K, rises to values $S_{max}(T, 0\,\mathrm{T}) \simeq 5\,\mu$V/K and falls abruptly to zero in the superconducting phase. Applying 14 T leads to an enhancement of $S_{max}(T, 14\,\mathrm{T}) \simeq 7\,\mu$V/K and smoothes the transition. Adding 12% Ni makes the sample reach its highest thermopower values of about $10\,\mu$V/K but with a very weak temperature dependence. No signs of superconductivity are left.

The broadening of the signal together with a slight increase in magnitude from 0 to 3%

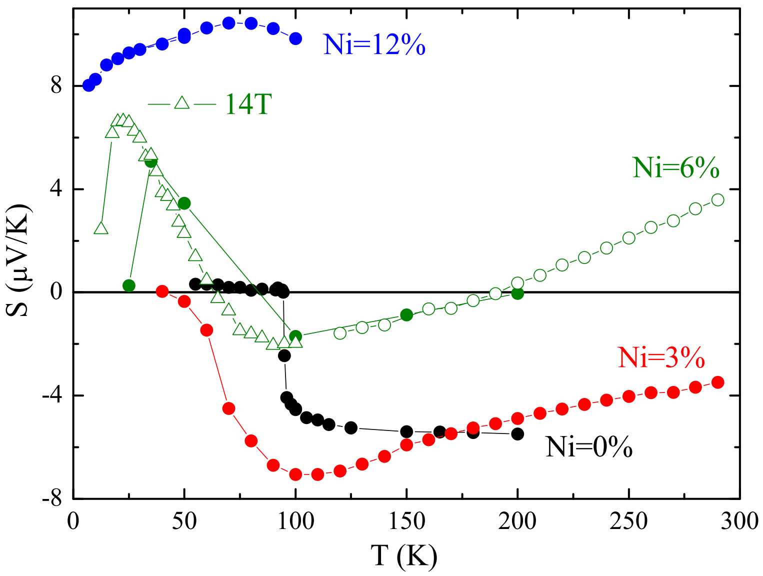

Figure 7.8: Temperature dependence of the thermoelectric power of $NdBa_2(Cu_{1-y}Ni_y)_3O_7$ for different amounts of Ni.

of Ni content is also present in a sample series with altered charge carrier concentration, $O_{6.9}$. This is shown in Fig. 7.9 in zero field only. Below $T_c \approx 38\,\mathrm{K}$ (3%), the signal should be rigorously zero, which is not the case. Possible reasons for this behavior remain speculative, the likeliest being that the stabilization criteria were set too loosely while measuring “top-down”.

The sample on the underdoped side, $O_{6.8}$ shows the highest value of all samples with $S_{max}(T, 0\,\mathrm{T}) \simeq 100\,\mu\mathrm{V/K}$. The sharp transition (solid black circles) is readily broadened in $H = 2\,\mathrm{T}$ as expected due to flux motion. Adding 3%Ni now drastically suppresses $S(T)$ to about $30\,\mu\mathrm{V/K}$ and again smoothes the transition into the superconducting state. 6% shows nearly the same temperature dependence, is slightly higher in absolute values and does not display any sign of superconductivity. It just decreases slowly and continuously from ∼120 K to 0.

Magnetic field dependence of the thermopower

As already discussed in section 4.2.5, moving vortices cause a voltage perpendicular to its direction of movement. Thus, if the vortex moves at angles to the applied temperature gradient, it produces a voltage that has parts in direction of the temperature gradient. This is the vortex-thermopower. Of course, a magnetic field is needed. The magnetic field dependent thermopower of the optimally doped and Ni-free sample is shown in Fig. 7.11. From 80 K to 94 K,[1] the magnetic field first needs to overcome the pinning field. This melting field, $B_m(T)$, gradually decreases with increasing temperature, as is shown in Fig. 4.5 in section 4.1.2. For $B > B_m(T)$ vortices are free to move. This leads to a steep

---

[1] Open diamonds are derived by field-sweep measurements.

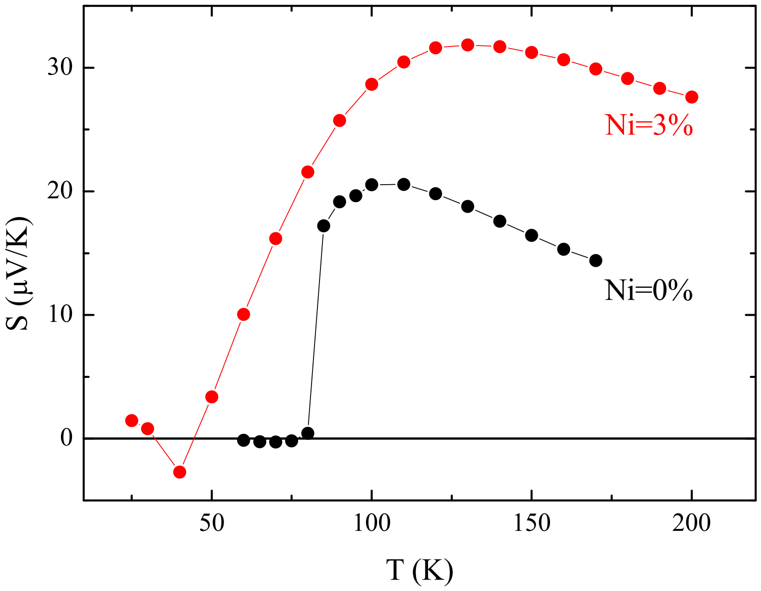

Figure 7.9: Temperature dependence of the thermoelectric power of NdBa$_2$(Cu$_{1-y}$Ni$_y$)$_3$O$_{6.9}$ for different amounts of Ni.

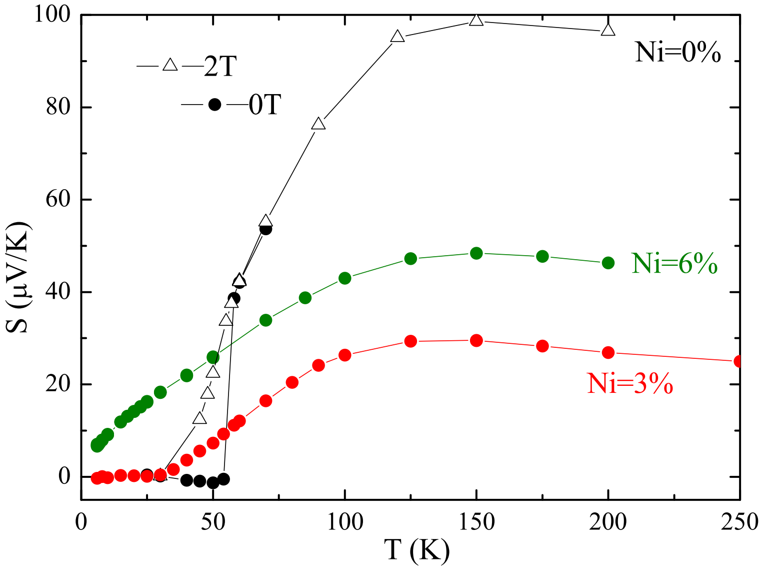

Figure 7.10: Temperature dependence of the thermoelectric power of NdBa$_2$(Cu$_{1-y}$Ni$_y$)$_3$O$_{6.8}$ for different amounts of Ni.

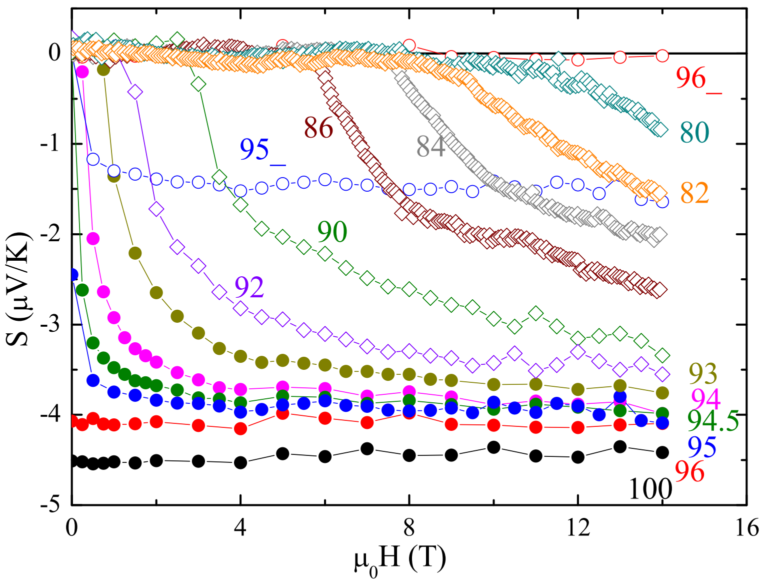

Figure 7.11: $S(B)$ of $NdBa_2Cu_3O_7$ measured in various temperatures from $T < T_c$ to $T > T_c$.

increase of the magnitude of the signal until it saturates at high fields. At $T \geq 96\,K$, the field dependence is gone. In this temperature regime above T_c, the supercurrent that opposed the QP current below T_c is gone. Thus, the thermopower above T_c is again determined by the steady state of the “thermally driven” and the “electric field” driven QP charge currents as depicted in Fig. 3.1. This signal is obviously field independent. In order to separate the field dependence in the vicinity of T_c, it seems to be a good approximation to subtract the zero field value $S(T, 0\mathrm{T})$ from $S(T, B)$. The corresponding curves are denoted by an underline beneath the temperature notion. Only $S(95\mathrm{K}, B)$ has a zero field value of $S = -2.5\,\mu\mathrm{V/K}$ (solid blue) that is non-zero and lower than S(95K, 14T). After subtraction, the curve is denoted by 95_ and represented by open blue symbols. The “vortex contribution” at 96 K is already zero, $S(96\_\,\mathrm{K}, B) = 0$. The temperature dependence of this contribution is depicted in Fig. 7.12, clearly showing an immediate abruption of the magnetic field dependence after crossing T_c from below. The “onset” temperature of the magnetic-field-dependent thermopower is at $T^S \simeq 96\,\mathrm{K}$. Let us keep in mind that the transition into the superconducting state itself has a certain transition width. Those width are determined as temperature difference of 10% to 90% of the diamagnetic transition. T_c is taken as the midpoint. In the sample discussed above, this width is about 1 K so that one can safely say that T^S is not out of the range of the transition. Thus, no anomalous thermopower is detectable above T_c in this sample.

The underdoped sample is analyzed similarly. The data is presented in Fig. 7.13 and is qualitatively comparable to the data in Fig. 7.11, but the sign changes. With $T_c \approx 53\,\mathrm{K}$, some curvature remains in the development of $S(B)$ at least up to 57 K. The curves, from which the quasiparticle contribution is subtracted, $S(B) - S(0)$ are displayed by the open

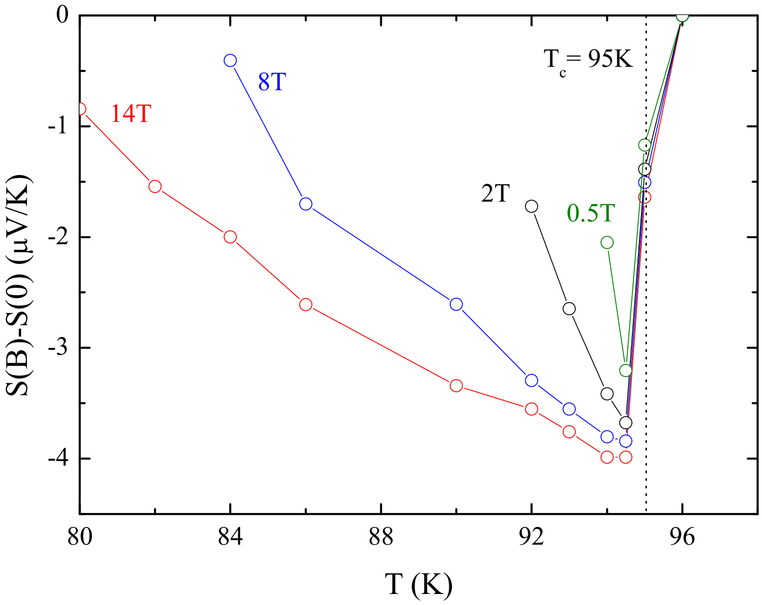

Figure 7.12: Onset of the "vortex thermopower" $S(B) - S(0)$ in $NdBa_2Cu_3O_7$.

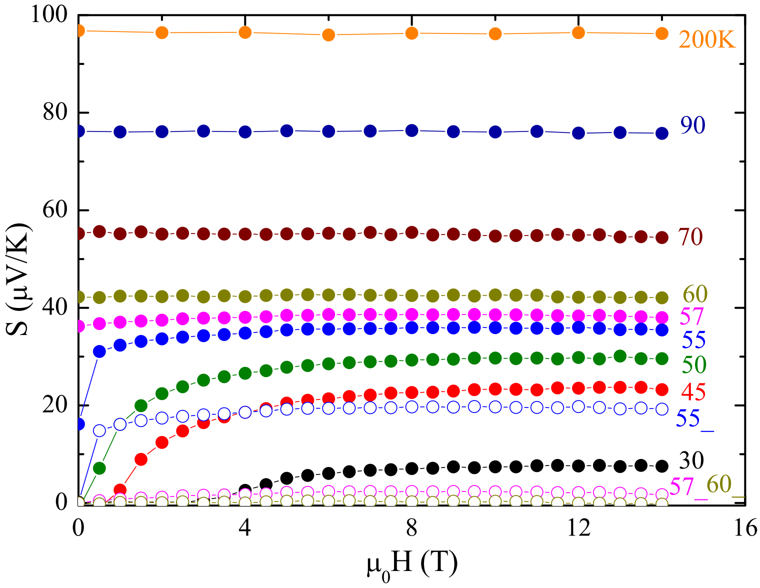

Figure 7.13: $S(B)$ of $NdBa_2Cu_3O_{6.8}$ measured in various temperatures from $T < T_c$ to $T > T_c$.

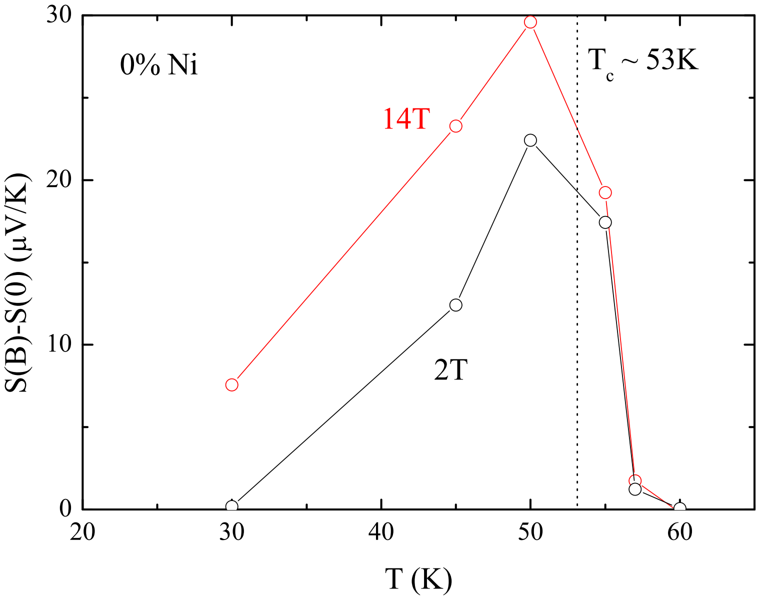

Figure 7.14: Onset of the "vortex thermopower" $S(B) - S(0)$ for 2 T and 14 T.

symbols. Their temperature dependence is depicted in Fig. 7.14 for 2 T and 14 T. This Figure also gives the impression that the vortex-thermopower dies out quite fast above T_c with an "onset" temperature of $T^S \simeq 60\,\mathrm{K}$. At first sight, this seems to be significantly higher than T_c but after considering the transition width again, which is 7 K in this sample, we are still in the vicinity of the superconducting phase transition itself. Thus, for the $NdBa_2Cu_3O_7$ and $NdBa_2Cu_3O_{6.8}$ samples, it is noticed that the magnetic field dependence of the thermopower basically does not survive the transition into the normal phase.

7.3 Nernst effect

Finally, we come to the Nernst effect. This part resembles the heart of this work. The motivation for these measurements is connected to the goal of unraveling the relation between high-temperature superconductivity and the pseudogap phase, as motivated in chapter 6. Now that all propaedeutic explanations are given, the desired data can be presented.

7.3.1 Data and analysis

Figure 7.15 shows measurements of the optimally doped samples for Ni contents of 0, 3, 6 and 12.%. At low T, the signal is zero until a typical temperature-dependent melting field is reached. At that field the density of vortices is sufficiently high to overcome pinning forces. In the adjacent "vortex-liquid" phase the vortices are free to move towards the cold end of the sample and thereby are able to produce the phase-slip voltage that gives the

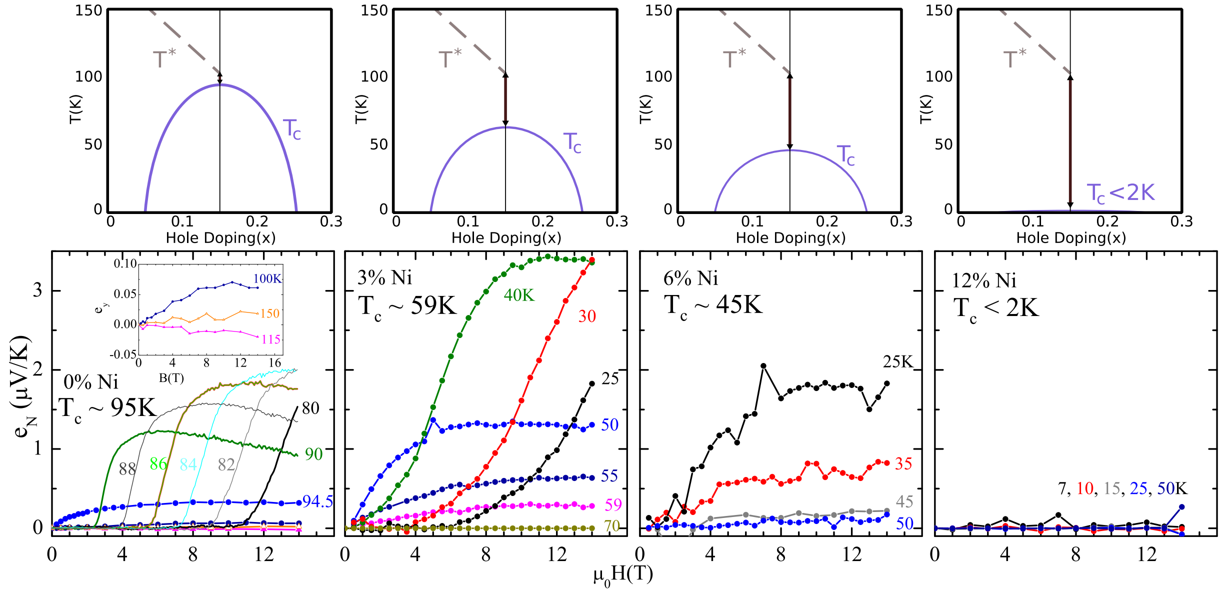

Figure 7.15: Nernst signal vs. magnetic field of optimally doped $NdBa_2\{Cu_{1-x}Ni_x\}_3O_7$ for x=0,.03,.06,.12. Atop on each Ni concentration a sketch of the expected behavior of the relation of T_c and T^* as was stated in [10].

anomalously enhanced Nernst signal. This causes the steep increase in the Nernst signal. When the field is further increased, the signal saturates until it slowly diminishes towards the upper critical field B_{c2}. This results in the characteristic "tilted-hill" profile of the Nernst signal in high-T_c cuprate superconductors [197]. Now increasing the temperature and approaching T_c the melting field begins to weaken until the signal rises immediately at $B = 0$. Above T_c the signal drops very sharply until it becomes very small, negative and linear in field.

The linear and negative contribution in the normal state that can be identified with the quasi-particle (QP) background [25, 198] which is very small in this optimally doped compound. This small background seems to be a common feature of the optimally doped [Y,Nd]-BCO samples [9, 141, 178], independent of the impurity-content. Increasing the Ni content to 3%, the absolute values of the signals increase while T_c drops to 59(8) K. In contrast to the sharp increase of the signal after exceeding the melting field in the pure sample, the signal rises more smoothly in the 3% Ni-doped compound. By further increasing the Ni-content to 6%, the absolute values of the Nernst signal decrease again until the signal can not be distinguished from the background at 12% Ni. In the entire series of the optimally doped samples the Nernst signal above T_c drops quickly. As mentioned above the QP contribution is very small. This finding already contrasts the expectations for the idea of an enhanced Nernst effect as a consequence of the enhanced pseudogap, as sketched in the upper panel of Fig. 7.15. The sketch of the pseudogap temperature T^* is not to be confused with the pseudogap energies determined from optical conductivity in Fig. 6.3. The temperature T^* is to be taken as a broader interval or crossover that

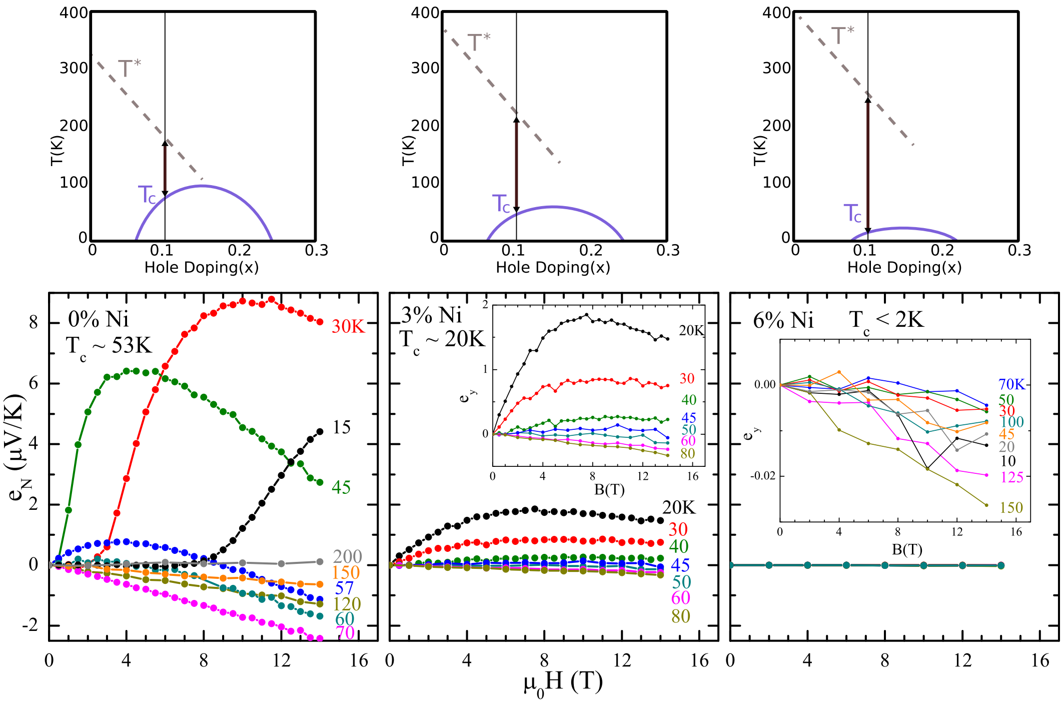

Figure 7.16: Nernst signal vs. magnetic field of underdoped NdBa$_2$\{Cu$_{1-x}$Ni$_x$\}$_3$O$_{6.8}$ for x=0,.03,.06. The sketches on top explicitly show the simultaneous suppression of superconductivity and the enhancement of T^*

guidelines the temperature and dopand (Ni, O$_{7-\delta}$) dependent trend of the opening of the pseudogap.

Next, we consider the behavior of the underdoped (O$_{6.8}$) compounds at Ni-impurity levels of 0, 3 and 6% (Fig. 7.16). The pure sample clearly shows vortex contributions to the Nernst signal. In addition, a very large negative QP signal is present at 70 K which is about 25% of the maximum vortex signal in the shown temperature range. Adding 3% Ni, the anomalous Nernst signal as well as the QP contribution decrease very sharply. For 6% Ni, the signal is further diminished and no systematic temperature dependence of the negative background can be deduced.

Now, we change the oxygen content again, this time to O$_{6.9}$, resembling a charge carrier concentration between the two aforementioned sample series. Ni-concentrations of 0% and 3% are presented in Fig. 7.17. The magnetic field dependence of the Nernst signal for 3% Ni behaves quite similar to its underdoped equivalent O$_{6.8}$, also showing smoother curves than the optimally doped sample and a large negative quasiparticle contribution of $e_N \simeq -2\,\mu$V/K. From 85 K downwards, the anomalous non-linear vortex signal becomes visible in this diagram. Below T_c, it again shows the characteristic "tilted hill" profile that is observed in the other Ni-free compounds. Towards higher temperatures, the linear signals approach zero. Adding 3% Ni leads to a rounder evolution of the vortex signal than in the pure sample.

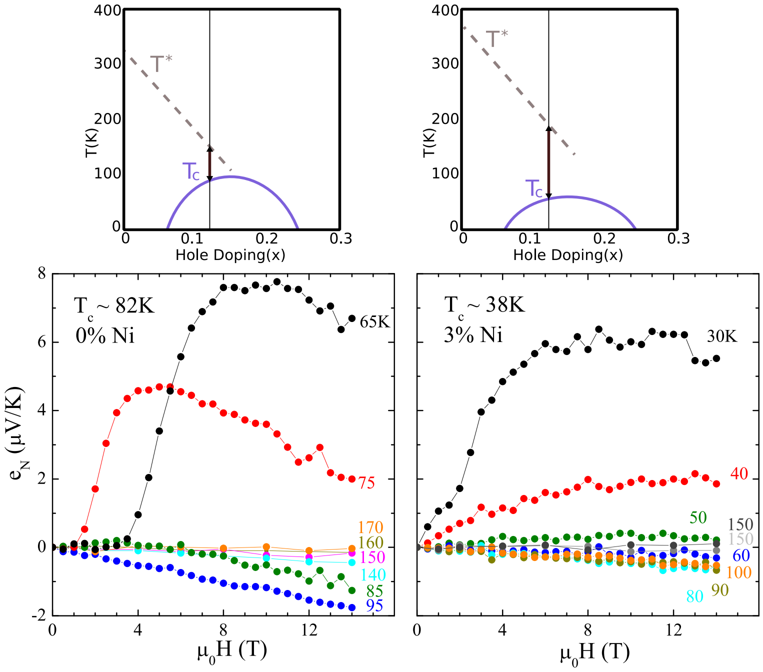

Figure 7.17: Field dependent Nernst signal of underdoped $NdBa_2\{Cu_{1-x}Ni_x\}_3O_{6.9}$ for x=0,.03.

Figure 7.18 (left panel) shows the Nernst coefficient, $\nu = e_N/B_z$, of the optimally doped sample series. Dividing by the field yields a field independent value only for the linear contributions of the Nernst signals produced by the QP background. At lower T, a voltage due to vortex movement adds to the QP contribution which leads to a strong field dependence of $\nu = \nu(B)$. In Figure 7.18 the open symbols are derived by linearly fitting the initial slope of e_N. The onset of the Nernst signal is then defined as the most negative value of ν. In Ref. [10] it is reported that the pseudogap can be restored or even enhanced by adding Ni-impurities to the optimally doped (or slightly overdoped) samples (as sketched in the upper panel of Fig. 7.15. This enhanced pseudogap can now be compared to the onset of the Nernst signals. The onset temperature, T^ν of Fig. 7.18 (indicated by arrows) shifts to lower temperatures as the Ni content is increased. If there was a scaling of T^ν with the pseudogap temperature one would expect the opposite behavior since the sample with 12% Ni is identified with the highest pseudogap temperature [10]. Here the decrease of T^ν is, however, closely connected to the decrease of T_c.

Surprisingly, the onset temperatures of both underdoped samples do not change with the Ni content (Fig. 7.18 (right panel)). This result differs from the onsets of the optimally doped series.

Let us compare the onsets of all samples as a function of doping. Figures 7.19 (left panel) and 7.19 (right panel) collect these onsets (again indicated by arrows) without Nickel and with 3% Nickel, respectively. Astonishingly, the samples with 3% Nickel seem to be unaffected by oxygen doping in their onset temperatures, while the onsets of the pure samples clearly follow the trend of T_c. In other words, keeping the oxygen content at $O_{6.8}$ and adding Nickel is qualitatively comparable to the scenario in which Nickel is held constant at 3% and the oxygen content is varied. Both onset behaviors show no dependence on T_c in the shown range. The latter described feature is yet to be understood.

7.3.2 Phasediagram, conclusion and outlook

Phasediagram

All onset temperatures (T^ν) are collected in the left panel of Fig. 7.20 as a function of T_c. These onsets can now be compared to the pseudogap data of [10]. Let me stress here that the onset of the anomalous Nernst signal, T^ν, is considerably higher than the width of the superconducting transition. This transition width is indicated by the error bars parallel to the T_c axis in Fig. 7.20.

The fluctuation regime is found to be narrow in our pure samples, e.g., the onsets are determined to be about 20 K higher than T_c. The scaling behavior of T^ν changes from the O_7 to the $O_{6.8}$ compounds. Although T^ν of the optimally doped samples clearly follow T_c, the onsets of the underdoped ones are essentially independent of the Ni content. Clearly no scaling to the reported enhanced pseudogap can be established for both series since it is shown that the pseudogap and the pseudogap temperature increase with increasing Ni-content [10]. As a more strict criterion for unambiguously verifying the vortex-Nernst-signal is a temperature which matches a positive Nernst coefficient. A value of $\nu = 10\,\mathrm{nV/KT}$ was chosen because the use of this threshold in other publications eases comparability [9, 178]. T($\nu = 10\,\mathrm{nV/KT}$) (open circles) scales downward from T^ν and is thereby proportional to T_c in the optimally doped compounds. Compared to the onset temperatures T^ν of the underdoped compounds, T($\nu = 10\,\mathrm{nV/KT}$)(open squares) develops a slope that tilts towards the slope of T_c but is still clearly distinguishable from the optimally doped ones. The slope of T($\nu = 10\,\mathrm{nV/KT}$) for the $O_{6.9}$ series finds itself again between the two aforementioned samples. A sharp decay of the Nernst signal above T_c is predicted by Ref. [199] whose calculations yield a proportionality $T^\nu \sim T_c$. This result is in agreement with our findings from the optimally doped samples. The high onset with respect to T_c in the underdoped phase (3% Ni) is comparable to the high onsets found in electron-irradiated $YBCO_{6.6}$ samples [178] as well as in $Y_{1-x}Pr_xBa_2Cu_3O_{7-\delta}$ [200]. These can be interpreted in terms of an unchanged T^ν while T_c is suppressed due to the impurity-induced disorder. The onset temperatures of electron-irradiated $YBCO_{6.6}$ can be compared in Fig. 7.21. Recent calculations connect the onset of the Nernst signal to the onset of superconductivity in spatially disordered systems [201]. This onset is then found to be at temperatures that represent the onset of superconducting islands, which percolate at T_c. This implies $T^\nu \ll T^*$, which coincides with our findings as well as with recent measurements of T^ν and T^* in oxygen depleted $SmBa_2Cu_3O_{6+x}$[202].

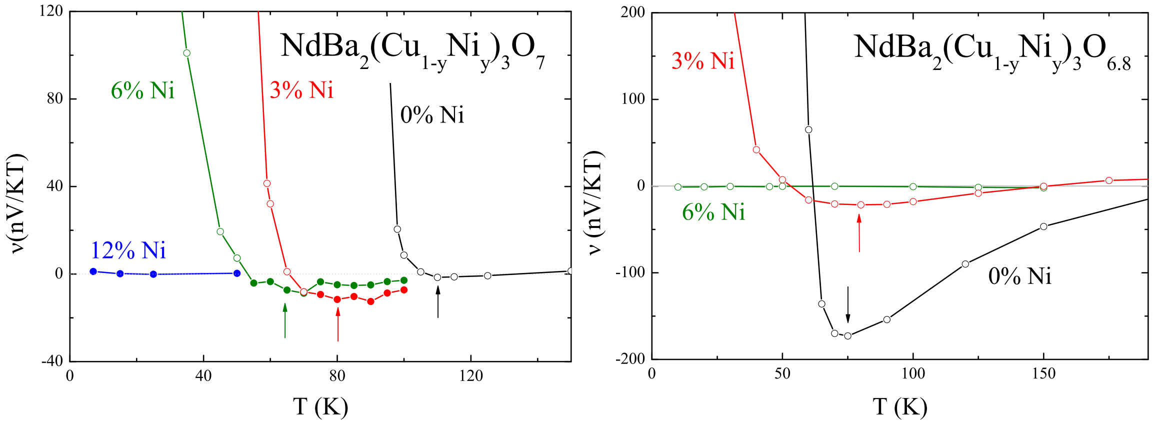

Figure 7.18: Temperature dependence of the Nernst coefficient for the denoted Ni contents and two oxygen doping levels, O_7 (left panel) and $O_{6.8}$ (right panel). The onset of the vortex Nernst signal is marked by arrows and determined by the temperature at which the Nernst signal deviates from field linearity.

Conclusion and outlook

Let me summarize the impact that Nernst effect experiments had on the investigation of the relation of superconductivity and the pseudogap phase, so far. A brief phenomenology of this state is given in section 4.4. As already mentioned in the first part of this thesis, there is no doubt that the Nernst effect is one of the most sensitive tools for the detection of vortex movement or vortex-like excitations. The onset of the anomalously enhanced Nernst signal due to vortex motion is easily to be distinguished from the quasiparticle background. The so won onset temperatures T^{ν} (Fig. 7.20) can be compared to the pseudogap temperatures derived by other experimental methods (compare with chapter 4.4). Nearly all measurements revealed an onset of the Nernst effect far above T_c with T^{ν} up to eight times T_c in heavily underdoped samples of the more two-dimensional compounds as the LaSrCuO-family [4, 9] and up to four times in the more three-dimensional compounds of the(Nd,Y)BaCuO-family [24, 178, 202]. However, these onset temperatures are far away from the pseudogap temperatures, T^*, as could be shown also in the studies of this work. New or altered theories now propose to subdivide the pseudogap into two phases: An upper pseudogap phase separation line (UPP), equivalent to T^* and a lower pseudogap temperature, LPP or T^{**} [201, 203], below which the systems display a Nernst effect and a strong diamagnetic response [9]. An approach by Dias *et al.* [201] takes T^* as a phase separation line. Upon doping the antiferromagnet a situation can be imagined in which the doped holes may become localized in spatially separated regions. This means the starting point is not spatially homogeneous. These holes may form ferromagnetic islands which leaves the rest of the sample in an antiferromagnetic environment. Such a scenario is referred to as “phase-separated” [205–207]. As the temperature goes down, charge segregation in-

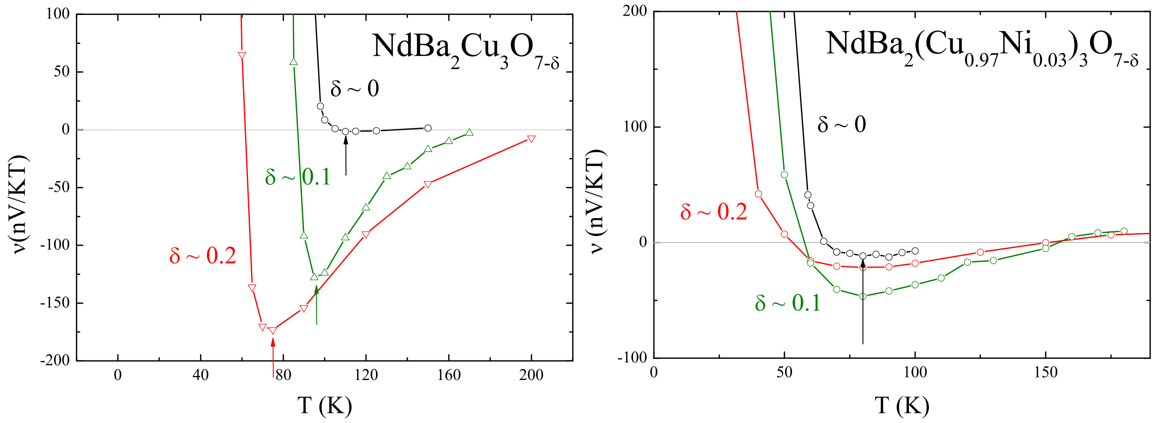

Figure 7.19: Onset determination in dependence of the oxygen content for a pure sample series (left panel) and with Ni = 3% (right panel). Onset temperatures are indicated by arrows.

creases. Each charge domain is characterized by a local pairing amplitude which arises at its own superconducting temperature. The maximum local values of these superconducting "islands" are then related to T^ν. In this picture, the bulk superconducting transition takes place when the isolated superconducting regions percolate. This scenario seems to be in agreement with the findings of a more or less constant T^ν in case T_c is suppressed by inducing disorder through impurities as found in this work [24] and in the work of Rullier-Albenque *et al.* [178].

In a semi-phenomenological approach Tsvelik *et al.* [203] identify the strongest coupling at (π,0) and (0,π) (depicted in Fig. 7.22, right panel) implying that fermions with these momenta form a 1D spin liquid (SL). It is stated that such 1D interactions open up quasiparticle gaps near these points in k-space below the crossover temperature T^*. Superconductivity is then prevented by strong 1D quantum phase fluctuations[2]. The relative phase of the two distinct order parameters at (π,0) and (0,π) gets locked at T^{**}, assuming a Josephson-type coupling between them. This implies another crossover to a 2D fluctuational regime now displaying a Nernst effect and a diamagnetic response. Here superconductivity cannot set in because long range phase coherence is disturbed by the thermally induced unbinding of vortex-antivortex loops, resembling the three dimensional cousins of the Kosterlitz-Thouless vortices [210]. Recent measurements by Hetel *et al.* [211] of the Cooper-pair density $n_s(T)$ in heavily underdoped Ca-substituted YBa$_2$Cu$_3$O$_{7-\delta}$ samples that were grown as thin as two monolayers displayed the characteristic jump at T_c that was predicted from KT-theory [212]. This unambiguous jump can be rounded by increasing the number of monolayers and thereby driving the system from 2D-KT behavior to the 3D-XY phase-disordering equivalent. These measurements as well as the smooth

---

[2] Contradictions to measurements that implicate 2D physics up to T^* such as the "stripe" scenario [208, 209] are also dealt with in [203].

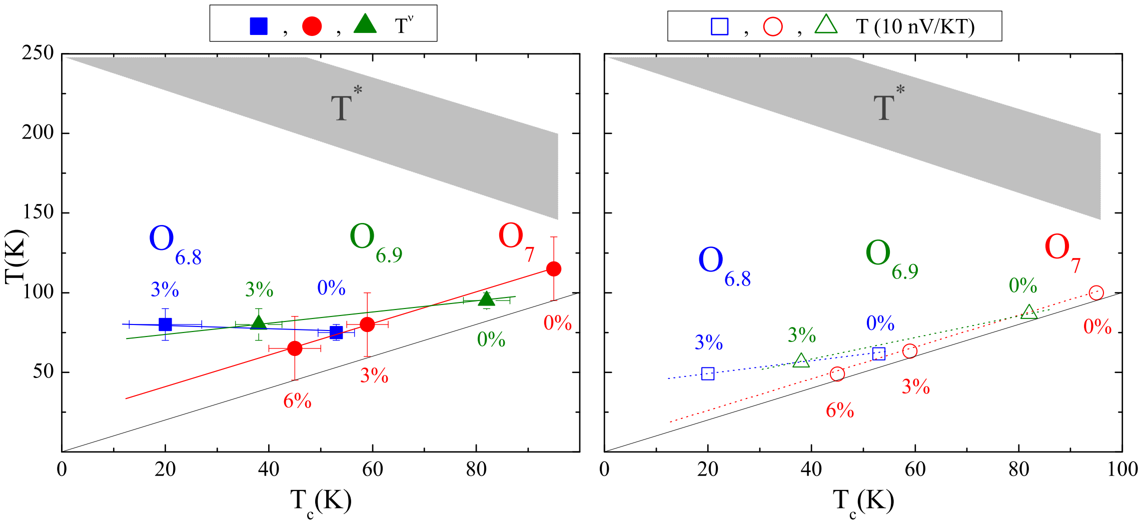

Figure 7.20: Onset temperatures of all measured samples versus T_c, represented by the full symbols in the left panel. Error bars in x direction represent the transition width of the superconducting transition. Error bars in y direction indicate the uncertainty in the onset determination. Open symbols (right panel) represent a threshold of 10 nV/KT (see text). This threshold is solely associated with a vortex Nernst signal. The T^* band sketches the pseudogap opening temperatures as estimated from the results of [10].

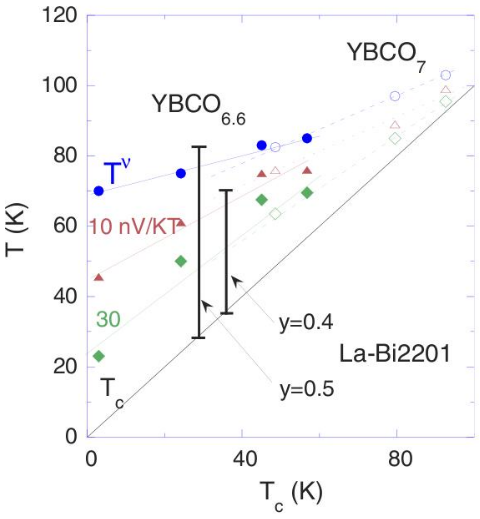

Figure 7.21: This related phase diagram for two YBCO samples with different oxygen contents can favorably be compared to ours. Open symbols represent YBCO$_7$, solid symbols YBCO$_{6.6}$. Circles and triangles are the onset temperature T^ν and $T(\nu = 10\,\mathrm{nV/KT})$, respectively. Taken from [178].

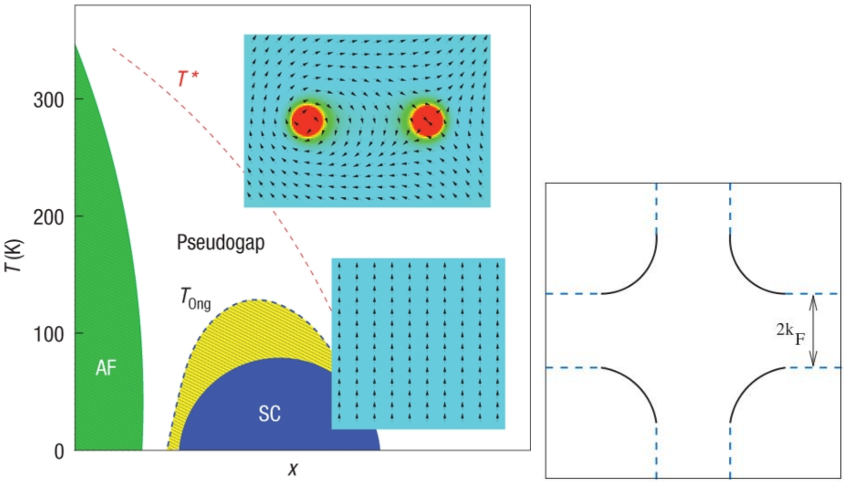

Figure 7.22: Left panel: The known generic phase diagram of the cuprates is extended by the onset temperature line of the anomalous Nernst effect T_{Ong}, as was found by the group of Ong. Depicted is an interpretation in favor of the "preformed pair" scenario, as given by [204]. The two insets to the right depict the ordered phase in the superconducting state (SC) and the disordered phase due to vortex-like excitations (red circles). Assuming a 3D system, this scenario would be the equivalent of the 2D Kosterlitz-Thouless (KT) model. Right panel: Scheme of the two dimensional Fermi surface in the cuprates. (0,0) is the center and the upper right corner is (π,π) [203].

evolution of Nernst signals across T_c [9] (depicted in Fig. 7.22) support the scenario of a "phase-disordered superconductor" replacing the pseudogap phase at least up to T^{**} [204].

7.4 Thermal Hall angle

As introduced in section 4.2.5, in analogy to the electrical Hall angle, $\tan\alpha = \rho_{xy}/\rho$, the thermal Hall angle is defined by $\tan\alpha_{th} = e_N/S$ for vortex movement in a temperature gradient. This relation gives the direction of vortex movement, because voltages are caused by $\mathbf{E} = \mathbf{v}\times\mathbf{B}$, with $\mathbf{v}$ being the vortex velocity. For the optimally doped sample $NdBa_2Cu_3O_7$, this angle is depicted in Fig. 7.23 for temperatures deep within the superconducting phase. The two left panels represent the measurements of the vortex-Nernst signal (top panel) and the vortex-thermopower (lower panel). The field dependent thermopower is negative, as is the corresponding zero field thermopower in Fig. 7.6. In the denoted temperature regime both quantities clearly display a zero signal below the melting field, B_m. For $B > B_m$ both signals rise steeply, the slope of e_n being even larger, but then follow a very distinct field dependence. While e_N develops negative curvature as the temperature increases (for $B \gg B_m$), S continues to increase in magnitude. The lower the temperature, the steeper the initial increase of e_N, in relation to S. The quotient of both is illustrated in the right panel. The characteristics just described are reflected in $\tan\alpha_{th}$. The difference in the slope of the initial increases shows up as a steep increase in the magnitude of $\tan\alpha_{th}$ right after exceeding B_m. This feature is pronounced only at 80 K and 82 K. At 80 K and 14 T, the ratio is about -2, which means the vortex velocity component along the temperature gradient is twice as high as the perpendicular component. As the temperature increases towards T_c (still observed at 14 T), the vortex velocity gradually gains components perpendicular to ∇T. At 84 K the vortex movement equally contributes to both quantities. $\tan\alpha_{th}$ continues to shrink as the temperature rises.

The same relation is displayed again in Fig. 7.24 for temperatures around T_c, showing a continuation of this relation. Both participating quantities, e_N and S are smoothly evolving across T_c with the difference that the QP thermopower above T_c does not show any field dependence while some curvature is still visible in $e_N(B)$. If T_c is crossed from above, the QP currents (with velocity $\mathbf{v_n}$) far from the vortex core are shunted by the Cooper-pair current (with velocity $\mathbf{v_s}$). This is the two fluid model that the analysis of vortex motion was based upon in section 4.2.5. Thus, the QP's still influence the direction of vortex movement below T_c, since the forces that act on the vortex depend on the magnitudes of the velocities and the densities of both, QP's and Cooper-pairs. I.e. the Iordanskii and the Magnus force are weighted with the QP density and the Cooper-pair density, respectively. Thus, as the temperature is lowered, the Magnus force should become stronger as the Iordanskii force becomes weaker and vice versa. Furthermore, the magnitude of the spectral flow force also depends on the physical regime and is believed to vanish to zero as $T \rightarrow 0$. It is the interplay of these forces that determine the temperature dependence of the thermal Hall angle below T_c. As the temperature is lowered, the overall perpendicular force on the vortex gets smaller since $\tan\alpha_{th}$ gets larger. The opposite is the case if the temperature

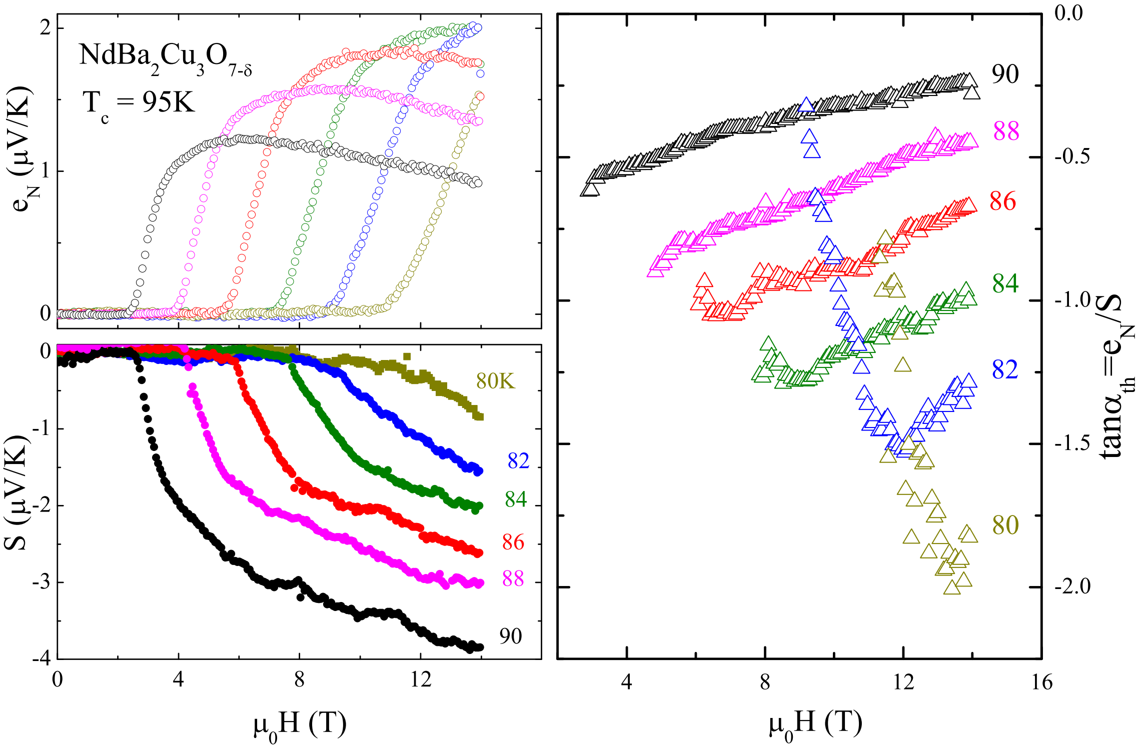

Figure 7.23: Thermal Hall angle for $NdBa_2Cu_3O_7$, $T < T_c$ and $B > B_m$.

approaches T_c from below. A pronounced perpendicular force drives the vortex mainly perpendicular to the applied temperature gradient. One may speculate that the Iordanskii force is now one of the main participants. In Fig. 7.24, $S(B)$ displays a smooth approach to the field-independent QP signal above T_c already at temperatures below T_c (e.g. 93 K) at high fields. It is not likely that B_{c2} is crossed already at 14 T, since recent insights about the temperature dependence of B_{c2} indicate that it is still as large as $\approx$ 100 T at T_c [175]. Equal characteristics of the high-field curves at temperatures slightly below and above T_c merely reflect the inseparability of votex motion from the QP influence in the superconducting phase.

In the underdoped sample, depicted in Fig. 7.25, the sign of the thermopower is positive in the whole temperature range and therefore, $\tan\alpha_{th}$ is positive as well. As discussed in section 4.2.5, the thermopower can change its sign also for vortex generated voltages. Keeping in mind, that the voltage is always generated perpendicular to the moving direction, a tilting of the angle of $\mathbf{v_\Phi}$ across the direction of the temperature gradient already explains this feature. At 30 K vortices move at angles of 45° with respect to the temperature gradient. With increasing temperature the trend is again to tilt towards larger angles.

The data of the $NdBa_2\{Cu_{1\text{-}y}Ni_y\}_3O_{7-\delta}$ samples presented so far can additionally be compared to the thermal Hall angle of the more two-dimensional high-T_c compound $La_{1.85}Sr_{0.15}CuO_4$ with $T_c \approx 32$ K, shown in Fig. 7.26. In contrast to the Nernst effect data

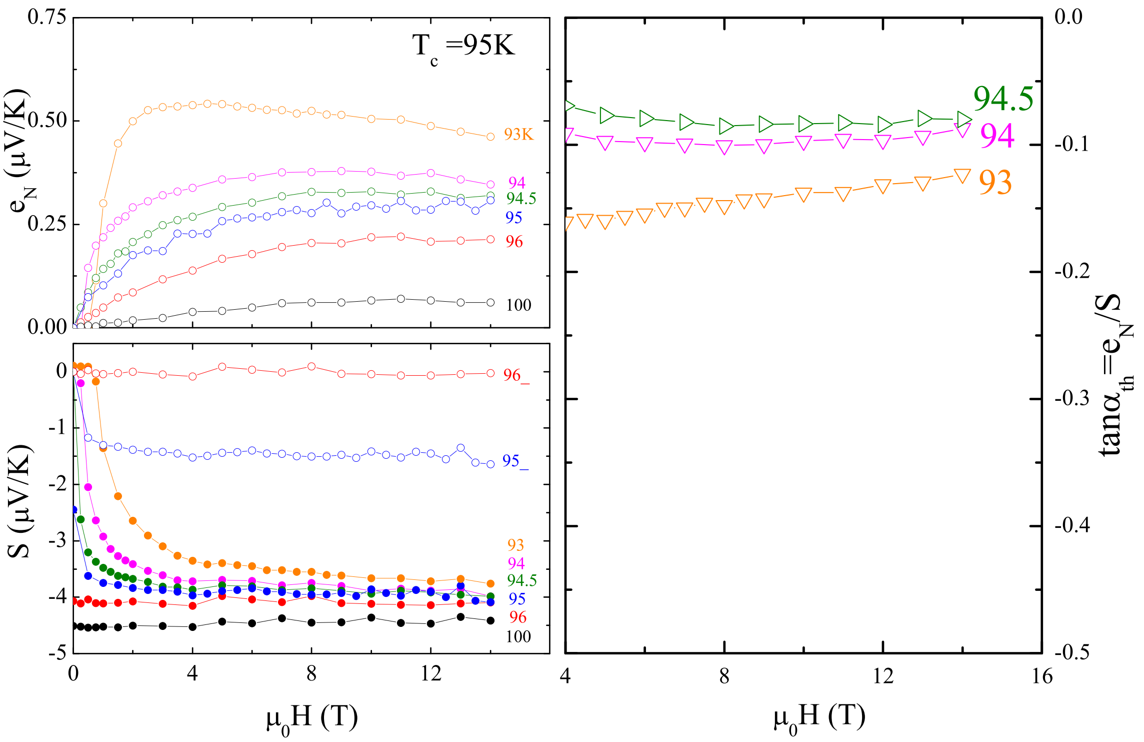

Figure 7.24: Thermal Hall angle for $NdBa_2Cu_3O_7$, $T \approx T_c$.

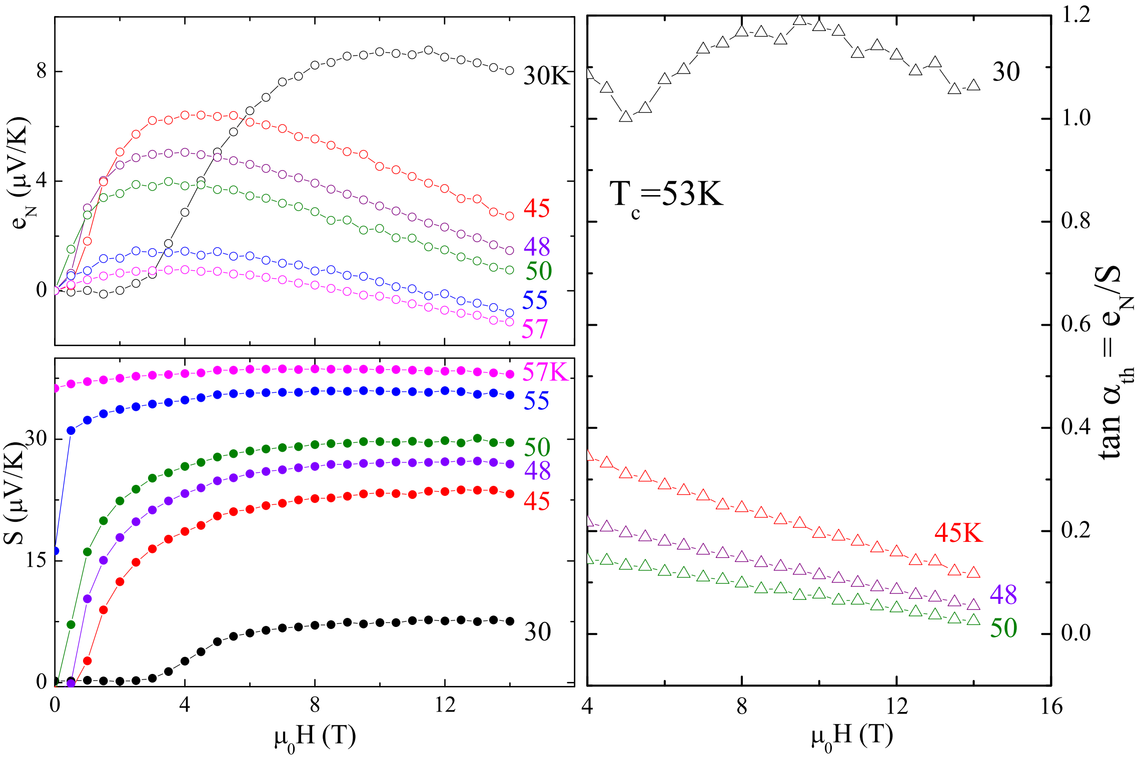

Figure 7.25: Thermal Hall angle of $NdBa_2Cu_3O_{6.8}$.

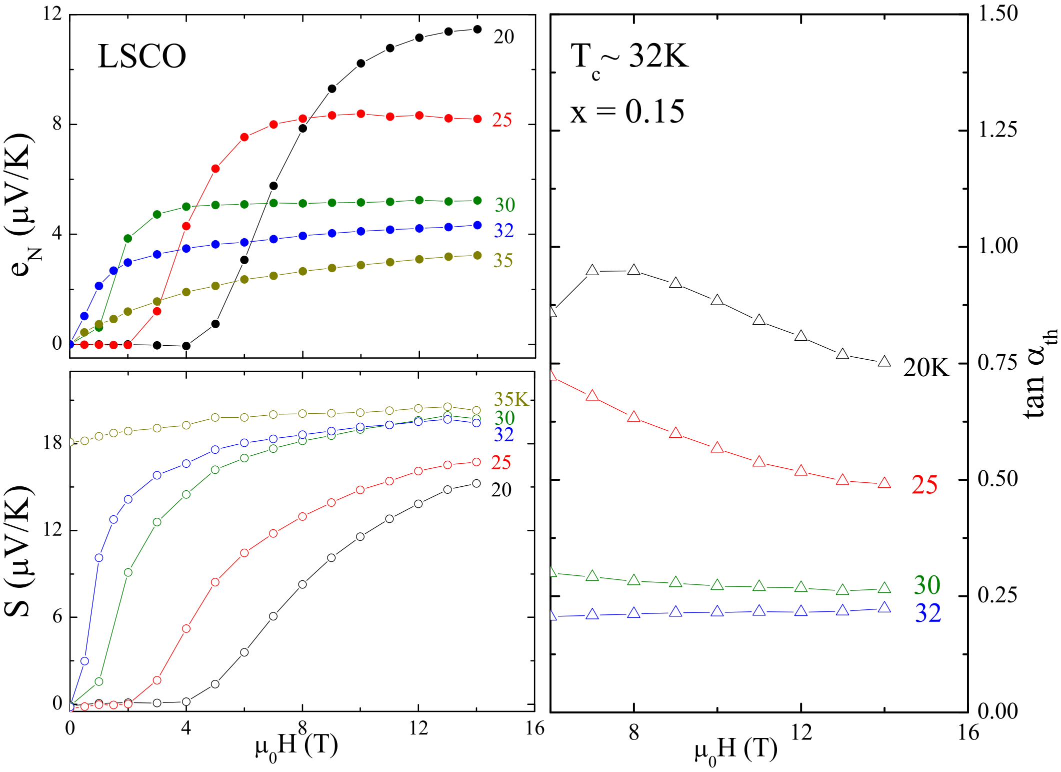

Figure 7.26: Comparison of e_N(B) and S(B) and their ratio, the thermal Hall angle $\tan\alpha_{th}$ in $La_{1.85}Sr_{0.15}CuO_4$ with $T_c \approx 32$ K. The ratio is only shown for $B > B_m$.

of the $NdBa_2\{Cu_{1-y}Ni_y\}_3O_{7-\delta}$ compounds, e_N displays a rather weak magnetic field dependence for $B \gg B_m$. The thermopower shows a smoother increase after exceeding the melting field. This increase is not saturated up to $B \leq 14$ T. The temperature dependence of the thermal Hall angle shows the same trend that was present in $NdBa_2Cu_3O_{7-\delta}$. $\tan\alpha_{th}$ clearly decreases for temperatures approaching T_c from below. The field dependence also shows similarities. It is more pronounced for lower temperatures. The loss of the field dependence around T_c has also been reported earlier in polycrystalline $Bi_{2-x}Pb_xSr_2Ca_2Cu_3O_\delta$ [96].

As a summary, a clear trend in $\tan\alpha_{th}(B,T)$ is present. The lower the temperature, the stronger is the Nernst signal in relation to the thermopower. This can be assigned to moving vortices as follows: Since a moving vortex effects a voltage perpendicular to its moving direction, its tilts more and more in direction of the applied temperature gradient as the temperature is lowered.

For temperatures above T_c, the following consideration stands to reason: The field dependence of the thermopower is vanishing basically within the width of T_c. This temperature was denoted with T^S in the section 7.2.2. The deviation from the field-linear QP background in the Nernst signal extends to much higher temperatures, T^ν, as presented in the preceding section. As an example, in $NdBa_2Cu_3O_{6.8}$, $T^S \simeq 60$ K while $T^\nu \simeq 75$ K. The high onset of the Nernst effect is predominantly interpreted as being caused by vortices or vortex-like excitations in the literature [4, 9, 174]. Consequently, if the developing voltage is being caused by the phase-slippage process, these excitations may also be assigned to a velocity. Thus, since from 60 K to 75 K only anomalous Nernst voltages and no anomalous thermopower voltages are detected in $NdBa_2Cu_3O_{6.8}$, one may speculate that these excitations “move” in direction of the temperature gradient. However, this feature of a far more pronouced anomalous Nernst voltage above T_c (compared to S), as well as a microscopic modelling of the smooth transition from QP voltages above T_c to the vortex-voltages below T_c is not intuitively obvious.

8 Nernst Effect and Transport in UPt_2Si_2

8.1 Motivation

The mysterious nature of the “hidden-order” (HO) phase in URu_2Si_2, discovered more than 20 years ago, is still unresolved [45, 213, 214]. Initially, HO was associated with a weak antiferromagnetic order setting in at $T_{HO} \simeq 17.5\,\mathrm{K}$ [46, 215]. However, recent experiments have shown that this transition is essentially non-magnetic [216]. Transport properties such as the Seebeck effect or the Nernst and Hall effects are very sensitive in detecting slight changes in the charge carrier spectrum at the Fermi energy. The appearance of a giant Nernst effect [11] emerging with the onset of the HO impelled the investigation of these transport properties in the related system UPt_2Si_2 which forms a local-moment antiferromagnetic ground state [12].

While for the high-temperature superconductors [4, 9, 24], the anomalous part of the Nernst effect is caused by moving flux lines, other mechanisms have to be held responsible for systems comprising the various classes of heavy fermions [11, 57, 217], semimetals [39], ferromagnetic metals [58, 61, 168] or organic compounds [218, 219]. Among these are anomalous scattering mechanisms like “side jump” [65] or “skew scattering” [64]. They are driven by magnetic order and are sources to the anomalous components of the Hall effect. Furthermore in some systems, Nernst effects can arise due to a combination of unusual physical properties. According to Oganesyan and Ussishkin [198], a large Nernst signal can arise in systems that combine lightweight charge carriers, long scattering lifetimes and reduced Fermi energies. Not only the latter but also a gap or a partial gapping of the Fermi surface (FS) has been identified as the source of anomalies in the Nernst effect [14] and the thermoelectric power [13] in antiferromagnets. These calculations consider the presence of a superzone gap in addition to phonon and spin scattering mechanisms.

8.2 Physical background

Imagine a situation in which an ordinary metal is polluted by impurities that contain magnetic moments due to partially filled inner shells. In general, the magnetic moment of the impurities is preserved. That is when the energy level of the impurities lie deep below the Fermi energy or in other words if the hybridization between localized and conduction electrons is small. A large Coulomb interaction of those localized electrons also facilitates the preservation of the magnetic moment [205]. If the level of the impurities overlap with

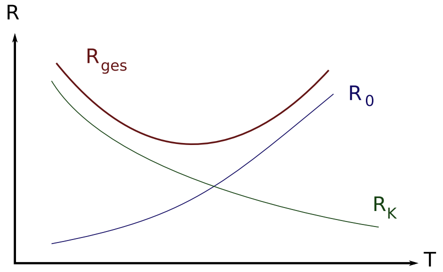

Figure 8.1: Illustration of the definition of the Kondo temperature as of Eq. (8.1).

the continuous spectrum, this electron of a certain spin orientation can escape into the conduction band and another one of arbitrary spin orientation takes its place. As a consequence the moment is reduced or completely quenched. This situation has been treated by Anderson, resulting in the Anderson model that successfully separates magnetic from nonmagnetic solutions in a mean-field approach [220]. If one also takes into account antiferromagnetic exchange interactions (J) between the localized moment and the conduction electrons, a process which can be pictured as virtual transitions from the impurity level to the conduction band and vice versa, the impurity spin is subject to being effectively screened out as the system is cooled towards absolute zero. This is the Kondo effect [221]. A direct consequence of the exchange interaction is the scattering of conduction electrons at the localized site. Potential scattering and spin flip scattering are the two relevant mechanisms resulting in a resistive behavior of type

$$R(T) = R_0(T) + R_K(1 - 2JD(\epsilon_F)\ln\frac{k_B\epsilon_F}{T}), \tag{8.1}$$

implicating a certain characteristic (Kondo) temperature where $R(T)$ displays a minimum, as depicted in Fig. 8.1,

$$k_B T_K = \epsilon_F e^{-\frac{1}{JD}}. \tag{8.2}$$

$D(\epsilon_F)$ denotes the density of states at the Fermi energy. The "screening" of the impurity spin can be visualized as a cloud of conduction electrons surrounding the localized moment.

If the restrictions to the case of one or only few impurities that furthermore lie deep below the Fermi energy is lifted, the variety of properties is even richer than in the impurity case. Now the overall numbers of impurities and conduction electrons are of the same order. Two competing regimes can be compared. One is a magnetic ordering at $T_c \sim J_{RKKY}$ caused by the exchange interaction of the f-electrons mediated by the conduction ones (RKKY interaction [222–224]). The opposing tendency tends to screen the magnetic moment, leading to a nonmagnetic ground state. The scale of this Kondo effect at each site is given again approximately by Eq. (8.2). So that if $T_c > T_K$ the ground stated is magnetically ordered and if $T_c < T_K$ the order is suppressed and the conduction electrons acquire a high effective mass m^* of the order of 10^2-10^3 electron masses, giving rise to an anomalously enhanced electronic specific heat coefficient γ of the same factor. In this context the name "heavy Fermion" indeed is related to the renormalized mass of the charge carriers.

In contrast to Eq. 8.1 the characteristics of the resistivity is different for the many impurity problem. The system now enters the Fermi liquid regime below some $T^* < T_K$ where the resistivity is mainly determined by electron-electron scattering, leading to $R(T) \sim (T/T^*)^2$.

The class of UT_2M_2 compounds, with T representing a transition metal and M mostly being a semiconducing element (i.e. Si or Ge), shows a large variety of exotic physical properties at low temperatures. Among them are ferromagnetic ordering (UCu_2Si_2 [225]), antiferromagnetic ordering (UCo_2Ge_2, UNi_2Ge_2, UCo_2Si_2, UPd_2Si_2 [225–227] and URu_2Si_2 (see introduction above)) and Pauli paramagnetism (URe_2Si_2 [227]). One substance out of that group, UPt_2Si_2, is subject to the transport measurements presented here. This substance hosts an antiferromagnetic ground state with a transition temperature of $\sim 32\,\mathrm{K}$ [228] and will be introduced in the next paragraph.

8.3 Magnetic properties and structure of UPt_2Si_2

The lattice is of type $CaBe_2Ge_2$ with space group $P4/mmm$. By means of neutron diffraction and susceptibility measurements the magnetic properties were resolved to effective magnetic moments μ_{eff} of $2.87\,\mu_B$/mole for $B||a$ and $3.39\,\mu_B$/mole for $B||c$ in the range of 200 to 300 K. The corresponding Curie-Weiss temperatures are $-31\,\mathrm{K}$ and $-98\,\mathrm{K}$ for the two field directions, respectively [228–230]. A modeling of the data has been carried out calculating crystalline electric field levels within molecular field approximation [230]. A more detailed discussion of the magnetic properties can be found in [231]. The structure is tetragonal with lattice constants $a = 4.186\,\mathrm{Å}$ and $c = 9.630\,\mathrm{Å}$. Neutron diffraction studies revealed the antiferromagnetic order as moments pointing in c direction with ferromagnetic coupling within the $a-a$ planes and antiferromagnetic coupling on adjacent planes along the c axis [12]. This is schematically depicted in Fig. 8.2, which was produced from ICSD data of ref. [228]. The results of a refinement for single crystal neutron diffraction data in annealed UPt_2Si_2 is given in [231]. Electronic specific heat values of $\gamma \approx 32\,\mathrm{mJ\,mol^{-1}K^{-2}}$ at low temperatures and $\gamma \approx 122\,\mathrm{mJ\,mol^{-1}K^{-2}}$ at 180 K are reported in [228]. The susceptibility, measured in a small magnetic field of 0.1 T along the c axis is shown in Fig. 8.2. The peak coincides with the transition into the antiferromagnetic phase. The adjacent steep decrease indicates that the moments are basically aligned along the field direction.

8.4 Measurements and analysis

The measurements presented in this section have been carried out on two annealed samples of UPt_2Si_2. As described in detail in [231] as-cast samples were annealed approximately for one week at a temperature of $T = 900°\mathrm{C}$. One sample was cut such that the appliance of either a temperature gradient or a transport current was easiest parallel to the a axis with the magnetic field applied along the c axis. The other sample was oriented and cut such that the temperature gradient is applied along c, which leaves the magnetic field and the transverse transport properties components in the $a-a$ plane. Temperature gradients

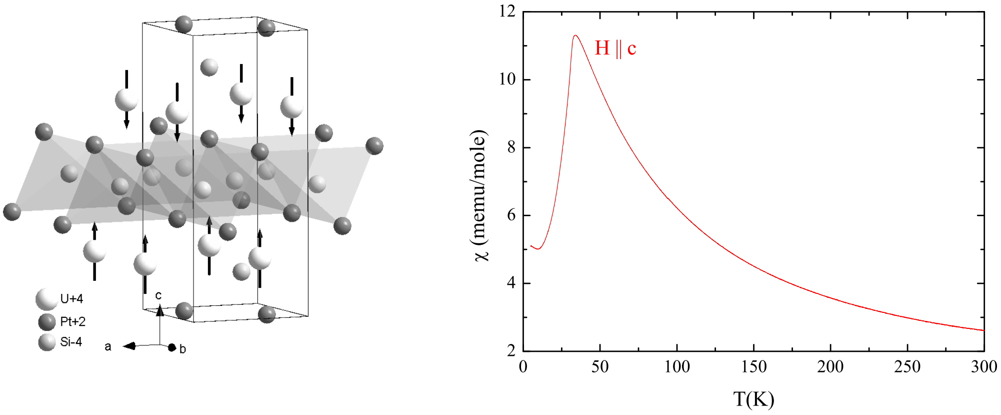

Figure 8.2: Left panel: Structure of UPt$_2$Si$_2$, ICSD data parameters from [228]. The orientation of the magnetic moments is indicated by arrows as described in [12]. Right panel: Suszeptibility of UPt$_2$Si$_2$, $H||c$.

have been applied using a chip heater glued to the top of the sample and were picked up by AuFe-Chromel thermocouples as described in section 5.

8.4.1 Configuration $(\nabla T, j) \parallel a$, $B \parallel c$

Electric and thermal conductivities

Figure 8.3 shows the temperature dependence of the resistivity of UPt$_2$Si$_2$ along the a axis. The magnetic field is applied along c. Coming from high temperatures, $\rho(T)$ shows a very weak temperature dependence with a broad maximum of $\rho(T) \approx 120\,\mu\Omega$cm at 200 K. At $T_N \simeq 31.5$ K (determined from the maximum of $d\rho/dT$ in Fig. 8.4) the transition into the antiferromagnetic phase shows up as a kink in ρ. This knee-like reduction of $\rho(T)$ can be modeled within a scenario in which magnetic excitations freeze out due to the opening of a spin wave gap [12, 232]:

$$\rho(T) = \rho_0 + AT^2 + \frac{DT}{\Delta}\left[1 + \frac{2T}{\Delta}\right] exp\left(-\frac{\Delta}{T}\right). \qquad (8.3)$$

A fit up to 22 K gives values of $\Delta = 44$ K, $A = 1.318 \cdot 10^{-3}\,\mu\Omega\text{cm}/\text{K}^2$, $D = 103\,\mu\Omega$cm and for the residual resistivity $\rho_0 = 25.3\,\mu\Omega$cm. Electronic transport shows localized behavior along the c axis which near T_N exhibits a clear dip in $d\rho/dT$, denoting the opening of a superzone gap in the charge channel (see Fig. 8 of Ref [12]). Above the transition, nearly no magnetic field dependence can be observed while it becomes quite strong in the ordered phase. The right panel of Fig. 8.4 displays the temperature dependence of the normalized

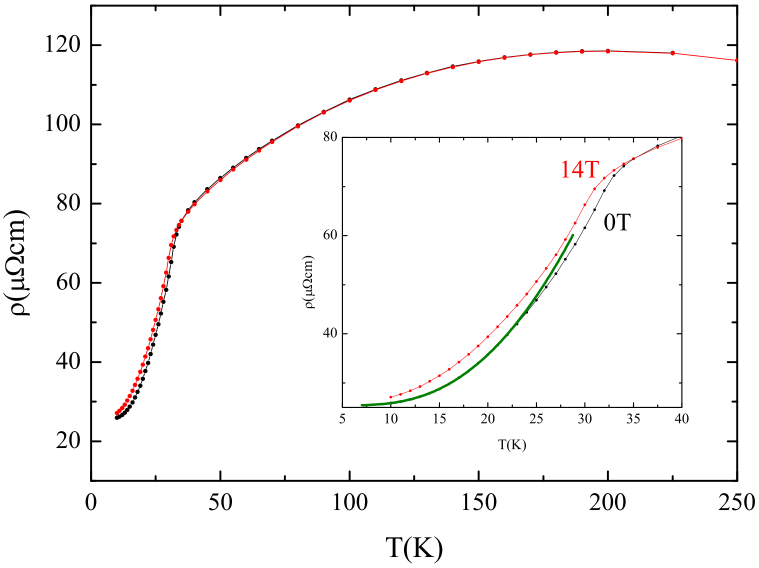

Figure 8.3: Resistivity of UPt_2Si_2 for 0 and 14T along the *a* axis. Magnetic Field is applied along *c*. Inset shows an empirical fit (after [232]) below the ordering temperature and up to 22 K, resembling the opening of a spin excitation gap of $\Delta \approx 44$K.

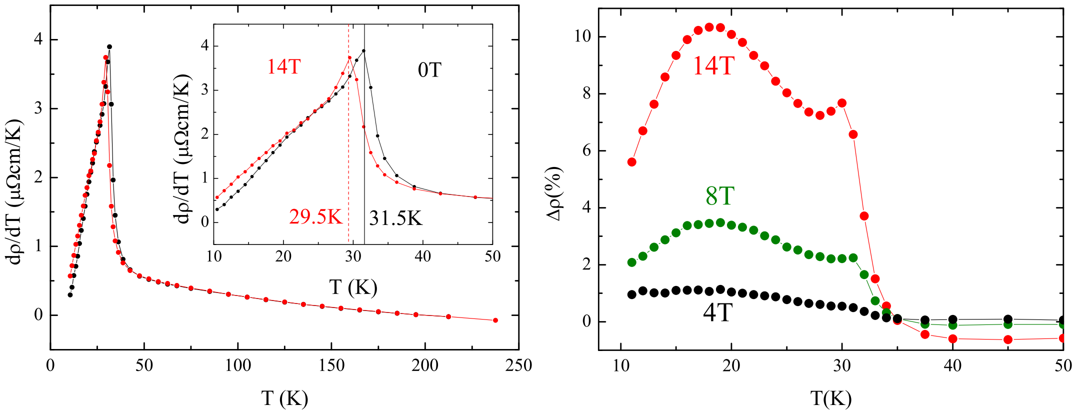

Figure 8.4: Left panel: Temperature derivative of the resistivity of UPt_2Si_2 for 0 and 14 T. As best seen in the magnification (inset) the transition into the antiferromagnetic phase is accompanied by a sharp peak at 31.5 K which is shifted to 29.5 K under the influence of 14 T. Right panel: Temperature dependence of the normalized magnetoresistivity for the three denoted fields.

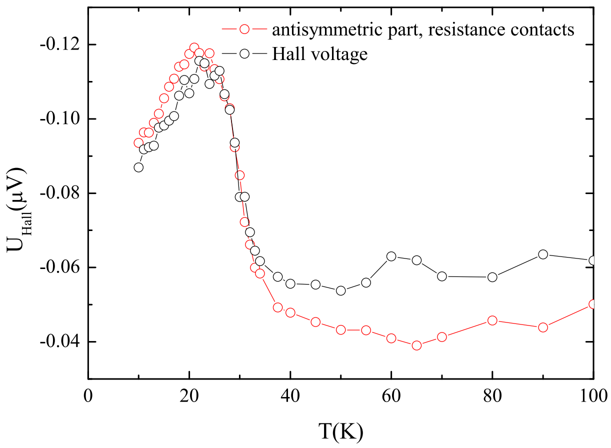

Figure 8.5: Comparison of the antisymmetric raw voltages of longitudinal and transversal electric contacts in 14 T, with $I = 12$ mA. The antisymmetric part of the transversal contacts are scaled to the antisymmetric part of the longitudinal contacts by a factor of 3, indicating quite a large misalignment of the longitudinal contacts, but still neglectable when analyzing the symmetric contribution (Fig. 8.3) because $U_{antisym}/U_{sym} < 1\,\%$.

magnetoresistivity, defined as

$$\Delta\rho = \frac{\rho(H) - \rho(0)}{\rho(0)}. \tag{8.4}$$

The magnetoresistivity is adjusted by Hall voltages that might add due to possible misalignments of the contacts. These Hall voltages are displayed in Fig. 8.5, scaled with the voltages picked up by the transverse contacts. Thus, in order to exclude transverse contributions, quantities are measured in positive and negative magnetic fields and are then symmetrizised. The quantitative behavior of $\Delta\rho$ exhibits some interesting features. Coming from the high temperature side and at a field strength of 14 T, $\Delta\rho$ is negative and nearly constant with small absolute values. Then a steep increase with a zero crossing at 35 K towards positive values sets in, forming a first sharp peak at $\sim T_N$ which is then followed by a small dent. A further lowering of the temperature leads again to an upturn followed by a broader peak which also hosts the maximum value of $\Delta\rho \approx 10\%$ at 18 K. The pronounced characteristics of $\Delta\rho(14\,\mathrm{T})$ are readily weakened for $\Delta\rho(8\,\mathrm{T})$. The low temperature broad maximum gets broader while the sharp peak at $\sim T_N$ tends to form a step until for $\Delta\rho(4\,\mathrm{T})$ a slow increase from the beginning of the antiferromagnetic transition towards the broad maximum of $\Delta\rho \approx 1\%$ at 18 K is left. These rather complicated features are speculated to being caused by either crystal field effects, the field dependence of the antiferromagnetic phase transition temperature or a metallic magnetoresistive component [231].

Figure 8.6 displays the temperature dependence of the thermal conductivity in zero field, 8 T, and 14 T. For $H = 0$, $\kappa(T)$ demonstrates a weak temperature dependence at

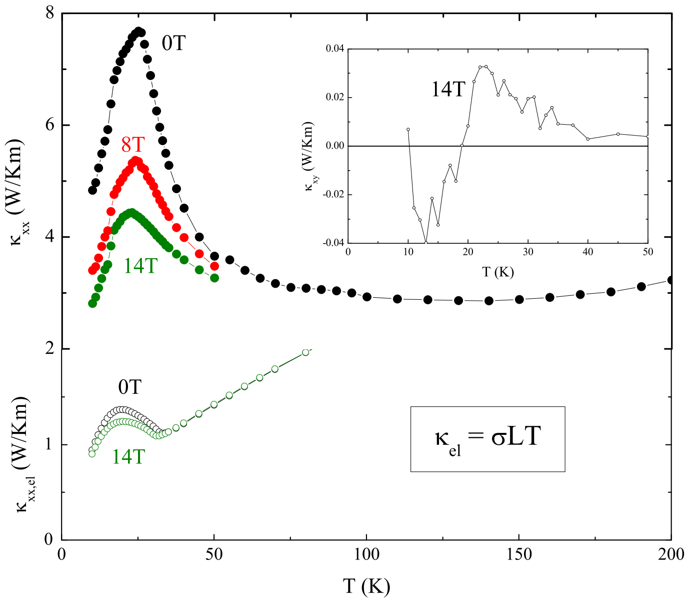

Figure 8.6: Thermal conductivity of UPt_2Si_2 for the denoted fields along the a axis. The magnetic Field is applied along c. The inset shows the off-diagonal component of κ which is of the order of 1% of κ_{xx}. The open symbols give an upper-limit estimation of the electronic contribution to the thermal conductivity as calculated by the Wiedemann-Franz law with $L_0 = 2.45 \cdot 10^{-8} \mathrm{W}/\Omega\mathrm{K}^2$.

high temperatures, with a shallow minimum at $T \approx 125\,\mathrm{K}$. With decreasing temperature, $\kappa(T)$ develops a peak around 25 K. The height of the peak is strongly B-dependent, while its position changes with B only very weakly. The inset of Fig. 8.6 displays the off-diagonal component of the thermal conductivity, κ_{xy}, also referred to as Righi-Leduc effect. The absolute values of κ_{xy} are more than two orders of magnitude smaller than the corresponding κ_{xx} values. The open symbols of Fig. 8.6 present an estimation of the upper limit of the electronic thermal conductivity, κ_{el}, calculated from the experimental data of $\rho(T)$ using the Wiedemann-Franz law, $\kappa_{\mathrm{el}} = L_0 T/\rho$ with $L_0 = 2.45 \cdot 10^{-8}\,\mathrm{W}/\Omega\mathrm{K}^2$ being the Lorenz number. At low T, the calculated κ_{el} is much smaller than the total measured κ; besides, it does not account for the strong suppression of κ by magnetic field. This indicates that the thermal conductivity in UPt_2Si_2 is predominantly phononic. The strong sensitivity of the thermal conductivity to the magnetic field in a broad temperature region, both above and below T_N, suggests that spin fluctuations play an important role as scatterers of phonons. It is surprising, however, that no clear anomaly of $\kappa(T)$ is observed at the magnetic ordering transition, see e.g. [233].

Seebeck and Nernst effects

The onset of the antiferromagnetic ordering is accompanied with an enhancement of the thermopower (Fig. 8.7), which furthermore becomes field dependent such that increasing

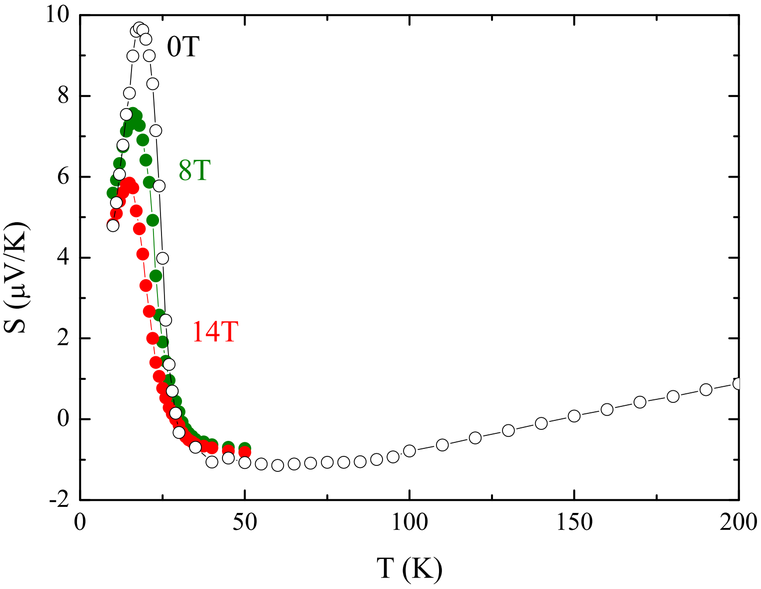

Figure 8.7: Thermopower of UPt_2Si_2 for magnetic fields of 0, 8 T, and 14 T ($\nabla T||a$, $B||c$).

fields suppress $S(T, H)$. The zero-field thermopower exhibits a steep increase in the vicinity of the antiferromagnetic ordering and peaks at about half T_N. Applying a magnetic field leads to a gradual suppression of the absolute values of $S(T \leq T_N)$ and slightly shifts its maximum to lower T. A large Nernst signal emerges below the antiferromagnetic transition temperature of $T_N \simeq 32$ K as depicted in Fig. 8.8. The signal is not anomalous in a way that it deviates from a field-linear quasiparticle background as is the case in many high-temperature superconductors. The signal here just rises below the temperature of the antiferromagnetic ordering and displays a linear field dependence. Upon lowering the temperature, e_N gradually increases until a maximum at ≈15 K is reached. Further cooling causes a decrease of the signal. The raw signal of the Nernst voltage is displayed in Fig. 8.8 in the inset for two exemplary temperatures. The curvature is mainly due to the magnetic field dependence of the thermal conductivity, which is eliminated in the antisymmetrization process.

In order to fully analyze the various contributions that the adiabatic Nernst signal may be composed of [57], the Seebeck effect, Hall effect and Righi-Leduc effect have been additionally measured,

$$e_N = \rho\alpha_{xy} - S\left[\frac{\sigma_{xy}}{\sigma} + \frac{\kappa_{xy}}{\kappa}\right]. \tag{8.5}$$

Here, α and $\sigma = \rho^{-1}$ denote the Peltier and conductivity tensor, respectively. To detect tiny transverse temperature gradients, an AuFe-Chromel thermocouple has been attached directly to the wires that pick up transverse voltages. The difference between the isothermal and the adiabatic Nernst signal is given by the product of the thermopower and κ_{xy}/κ and is shown in Fig. 8.8 (lower panel) at 14 T. It becomes clear that the magnitude of the thermopower that might add to the transverse voltages due to a transverse temperature

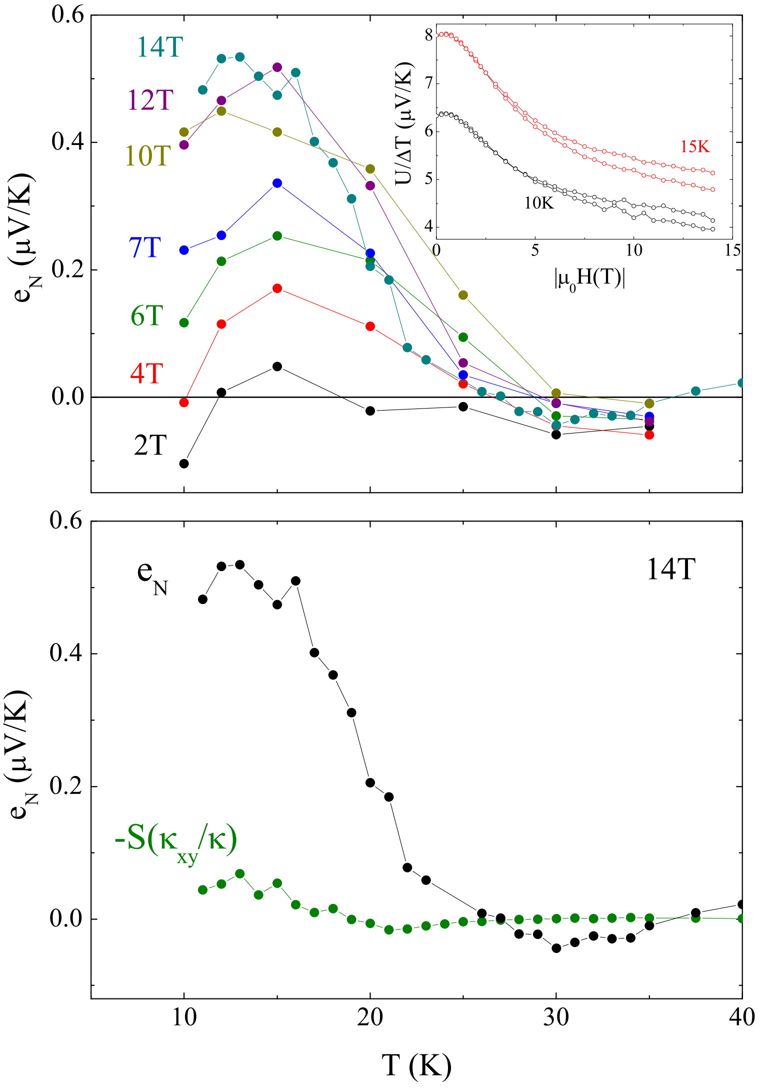

Figure 8.8: Upper panel: Temperature dependence of the Nernst signal of UPt_2Si_2 in various magnetic fields. Inset: Raw voltage of the Nernst contacts with $|\mu_0 H|$ along c. The splitting in the curves resembles the difference in raw voltage that is picked up when the magnetic field is reversed. The antisymmetric part is half of this difference for each temperature run. Lower panel: Comparison of the temperature dependent thermal Hall contribution to the measured Nernst signal, in $B = 14\,\mathrm{T}$ ($\nabla T || a$, $B || c$).

gradient is much smaller than the measured e_N. In 14 T, κ_{xy}/κ_{xx} is of the order of 1% so that its product with the thermopower $S(T, 14\mathrm{T})$ results in a contribution of less than 10% of the measured $e_N(T, B)$. Thus, we can safely discuss the Nernst signal as being essentially isothermal.

Analysis and discussion

Let me discuss the data by opposing two ways of interpretation: the first (I) is based on the argumentation by Bel *et al.,* [11], introducing an interrelation between the electronic specific heat and the thermopower in the related system URu_2Si_2. The second (II) is based on calculations taken out already in 1972, relating the appearance of enhanced Nernst and Seebeck effects with the opening of a charge gap in generic antiferromagnets [13, 14].

(I) In URu_2Si_2, the onset of the hidden order at T_0 is accompanied with an enhancement of the magnetic field dependent thermopower while the electronic specific heat drops from $\gamma = 180\,\mathrm{mJ\,mol^{-1}K^{-2}}$ above T_0 to $\gamma = 60\,\mathrm{mJ\,mol^{-1}K^{-2}}$ below. A dimensionless ratio relating the Seebeck coefficient and the electronic specific heat was introduced in [234],

$$q = \frac{S}{T}\frac{N_A \cdot e}{\gamma}, \tag{8.6}$$

with $N_A \cdot e$ being the product of the Avogadronumber and the elementary charge, also known as Faraday number ($9.6 \cdot 10^4\mathrm{C/mol}$). Eq. (8.6) is derived by relating the density of states which governs the temperature dependence of S/T for free electrons in Eq. (3.8) with the electronic specific heat, $C_{el}/T \propto D(\epsilon_F)$. In the regime of very low temperatures together with the assumptions made above, the thermopower can be said to probe the specific heat per electron [30]. Now, the simultaneousness of the increase in S/T and the decrease in C_{el} were argued to be in sharp contrast to the expectations for URu_2Si_2 [45, 214, 235]. Bel *et al.* propose to solve this contradiction by assuming a drastic increase of entropy per electron at the onset of the HO.

In order to fit the enhanced Nernst signal into this picture, it can be analyzed by a formula relating the Nernst signal to the energy derivative of the Hall angle at the Fermi energy as recently put forward by Oganesyan and Ussishkin [198],

$$e_N = N = \frac{\pi^2}{3}\frac{k_B^2 T}{e}\frac{\partial \theta_H}{\partial \epsilon}|_{\epsilon_F}. \tag{8.7}$$

In a further approximation, the energy dependence of the Hall angle is replaced by θ_H/ϵ_F. Thus, in order to prove the validity of the assumptions for the free-electron model in URu_2Si_2, N/T and θ_H should display a scaling behavior. Both quantities are depicted in Fig. 8.9 (a) with the left scale for N/T and the right scale for $\theta_H = \rho_{xy}/\rho$. This attempt reveals that this scenario is somewhat oversimplified: the Hall angle saturates towards low temperatures while N/T continuously grows. To test whether such a simple relation is applicable for the related compound UPt_2Si_2, an equal scaling is attempted in Fig. 8.9 (b). Again without success: The Hall angle behaves more step-like while e_N/T starts to rise

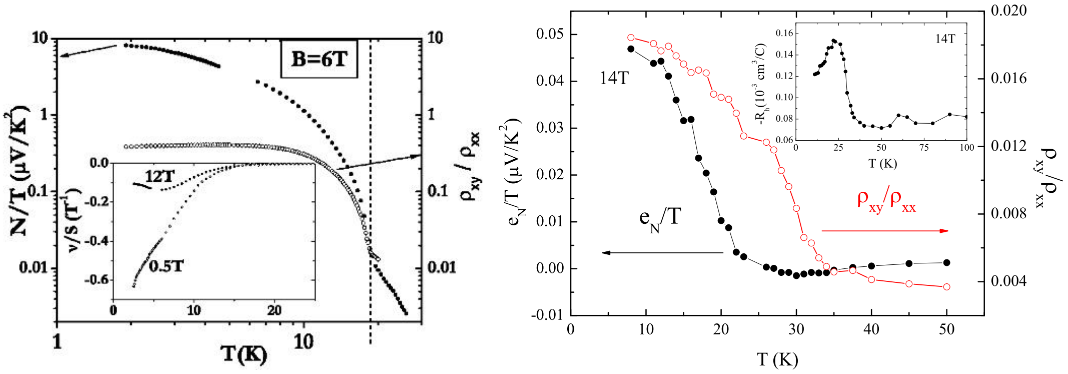

(a) URu_2Si_2 (b) UPt_2Si_2

Figure 8.9: $N/T = e_N/T$ vs Hall angle in URu_2Si_2[11] (a) and UPt_2Si_2 (b). Shown is the Nernst signal divided by temperature (left scale) and the Hall angle (right scale) as a function of temperature, representing a crude approximation which disregards the energy dependence of the Hall angle at the Fermi energy. The inset in (b) depicts the temperature dependence of the Hall coefficient of UPt_2Si_2 in 14 T with its pronouced increase below T_N.

more smoothly and at a lower temperature. This behavior immediately indicates that the scattering time, $\tau = \theta_H/\omega_c$, is more strongly dependent on energy at the Fermi energy. Thus, the energy dependence of τ in Eq. (8.7) cannot be replaced by τ/ϵ_F.

In summary, there are some reasons that make this model too crude an approximation for UPt_2Si_2: The derivation of Eq. (8.6) is based on a free electron model as is the simplification of Eq. (8.7). Strictly speaking, these derivations only hold in the low temperature limit, $T \rightarrow 0$, where a constant mean free path can be assumed (see also chapter 3). The attempted scaling in Fig. 8.9(b) based on these assumptions is not convincing.

(II) Using a free-electron relaxation time model, Abelskii *et al.* [13, 14] have calculated the Nernst and Seebeck effects for generic ferro- and antiferromagnetic materials. The antiferromagnets possess a superzone gap due to the doubling of the lattice periodicity. This charge gap when combined with spin and phonon scattering causes a large contribution to the Nernst and Seebeck signals below T_N while the resistivity shows a much smaller effect. The calculations predict a maximum of the thermopower between 0.4 and $0.6 \cdot T_N$ [13]. The Nernst coefficient is calculated in a similar manner, and is found to display also a maximum at about half T_N [14]. Within these calculations the Hall coefficient is subjected to a steep increase after crossing into the antiferromagnetic phase. A further prediction of the calculation is a scaling of the Nernst effect with the product of the thermopower and the Hall coefficient [14].

Let me compare these predictions with our measurements, starting with the thermopower in Fig. 8.7. The characteristics of $S(T)$ clearly displays the calculated features, a steep increase below T_N with the maximum value appearing at about half T_N. In addition, a sign

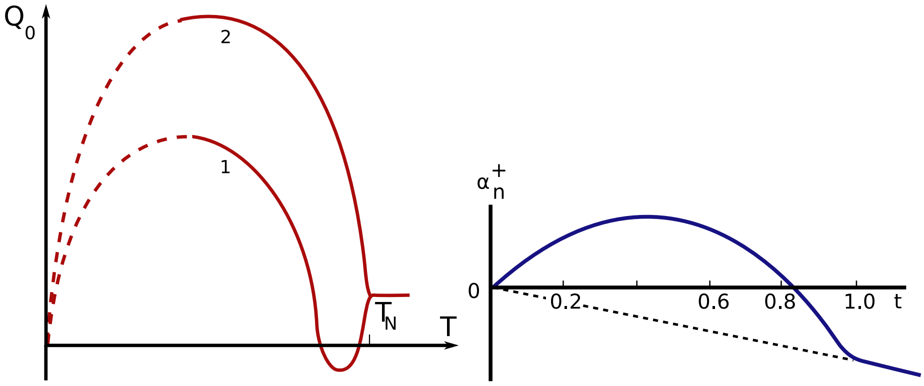

(a) Nernst effect (b) Thermopower

Figure 8.10: (a) Calculated temperature dependence of the Nernst coefficient for antiferromagnetic metals. This models is based on the assumption of a gap opening in the carrier spectrum due to a doubling of the magnetic unit cell. It further includes scattering mechanisms on phonon and spin excitations. Curve (1) corresponds to $l > k_F$ while (2) resembles $l < k_F$ with l being the quasimomentum and k_F the Fermi wavenumber [14]. (b) The same model applied for the thermopower, with $t = T/T_N$ and electron conduction. For hole conduction the curve would be mirrored on the t axis [13].

change at $0.85 \cdot T_N$ is proposed by Abelskii [13], a feature that is shared by the measured thermopower in Fig. 8.7. The Nernst effect is shown in Fig. 8.8 displaying a pronounced increase just below T_N which ends in a maximum formation at about half T_N. This very nicely meets the calculated prognoses as shown in Fig. 8.10 (a) that also shows an increase just below T_N which reaches its maximum at $\simeq 0.5 \cdot T_N$. According to the calculations, the Hall coefficient should be increasing below T_N. This behavior is verified by experiment once more, as depicted in the inset of Fig. 8.9 (b). The thermopower and the Hall effect are predicted to scale with the Nernst effect within the framework of the theory. As shown in Fig. 8.11 (lower panel), the theory is once again nicely verified with respect to the scaling behavior, since the experimental data clearly display this proportionality $e_N \propto (S \cdot R_H)$.

Figure 8.11 (upper panel) displays such a scaling of e_N and $(S \cdot R_H)$ for the related system URu$_2$Si$_2$ ($T_{HO} = 17.5\,\mathrm{K}$). The scaling is vastly disturbed between $0.4 \cdot T_{HO}$ and T_{HO}. Obviously, this scaling is not fulfilled. Thus, it becomes evident that the underlying physics of both substances cannot be completely of the same origin. The differences between these two systems are obviously caused by the complicated behavior of the thermopower in that temperature region [11]. Furthermore, the positions of the maxima at $\approx 0.2 \cdot T_{HO}$ of e_N and S are shifted to lower values than the expected $0.5 \cdot T_{Order}$. One may speculate here that the HO phase is responsible for additional features besides those calculated for a generic antiferromagnet [13, 14]. Nevertheless, the Nernst signal of UPt$_2$Si$_2$ shown in Fig. 8.8 qualitatively resembles the Nernst signal found in URu$_2$Si$_2$ ($e_{N,max}(12\,\mathrm{T}) \approx 30\,\mu\mathrm{V/K}$) where it develops just below the HO ordering temperature [11], although $e_{N,max}(12\,\mathrm{T})$ is much lower in $\mathrm{UPt_2Si_2}$ ($\approx 0.5\,\mu\mathrm{V/K}$).

In summary, we find the emergence of a large Nernst signal in $\mathrm{UPt_2Si_2}$ below T_N which is accompanied by anomalies in the thermopower and the Hall coefficient. These features very well agree to predictions of Refs. [13, 14] for antiferromagnets under the assumption of a gapping of the Fermi surface below T_N. Our transport measurements suggest that the gap evolving in the charge channel has to be attributed to only a portion of the Fermi surface, otherwise a metal-to-insulator transition in the resistivity was observable (Fig. 8.3). This partial gapping of the Fermi surface are common features in both related substances, $\mathrm{URu_2Si_2}$ and $\mathrm{UPt_2Si_2}$, but the model used for $\mathrm{UPt_2Si_2}$ is not completely suitable for $\mathrm{URu_2Si_2}$, indicating the influence of the itinerant character of the hidden-order phase. Nevertheless, the behavior of the Nernst effects in both systems may be connected to the gapped regions of the Fermi surface.

8.4.2 Configuration $\nabla T \parallel c$, $B \parallel a$

In the configuration $\nabla T \parallel c$, $B \parallel a$, no Nernst signal could be resolved. Strong differences to the a-axis transport (last section) are already expected from electronic transport measurements along c, showing localized behavior in this direction [12, 231]. The resistivity is reported with residual values $\rho_0 > 200\mu\Omega\mathrm{cm}$ [12] and being dominated by a non-metallic contribution $d\rho/dT < 0$. Applying a temperature gradient along c with the magnetic field in the $a-a$ plane reveals a very weak magnetic field dependence of all measured transport properties. This is in clear difference to the measurements with $H \parallel c$. $\kappa_c(T,B)$ that is depicted in Fig.8.12 shows an even smaller magnitude than $\kappa_a(T,B)$ (Fig. 8.6). The shape of $\kappa_c(T,B)$ supports the non-metallic character since $d\kappa_c/dT > 0$ is typical for amorphous and glass-like structures that do not show the usual phononic thermal conductivity. Additionally, the magnetic field dependence of κ_c is very weak.

The thermopower is displayed in Fig. 8.13. A pronounced magnetic field dependences is absent as well. Although the characteristics of the curve are related to that along the a direction (Fig. 8.7), the sign of $S_c(T,B)$ is reversed and the magnitude is nearly twice as large as for $S_a(T,B)$. This increase in magnitude well agrees with the much more localized behavior along c, since in the simplest picture the magnitude of the diffusion thermopower is inversely proportional to the charge carrier concentration, see Eq. (3.8). A pronounced kink in the slope of $S(T)$ is present at the phase transition to the antiferromagnetic phase at $T_N = 31.5\,\mathrm{K}$. This is best seen in the temperature derivative dS/dT, depicted in zero-field in the inset of Fig. 8.7. As none of the above quantities are showing pronounced reactions to magnetic fields up to 14 T, one may anticipate that resolving a Nernst voltage will be difficult. So it is. The raw voltage, divided by the temperature difference at both thermocouple ends is shown in Fig. 8.14. One can see by eye that no antisymmetric contribution other than noise can be resolved here, since a magnetic field dependence is nearly absent in the raw voltage.

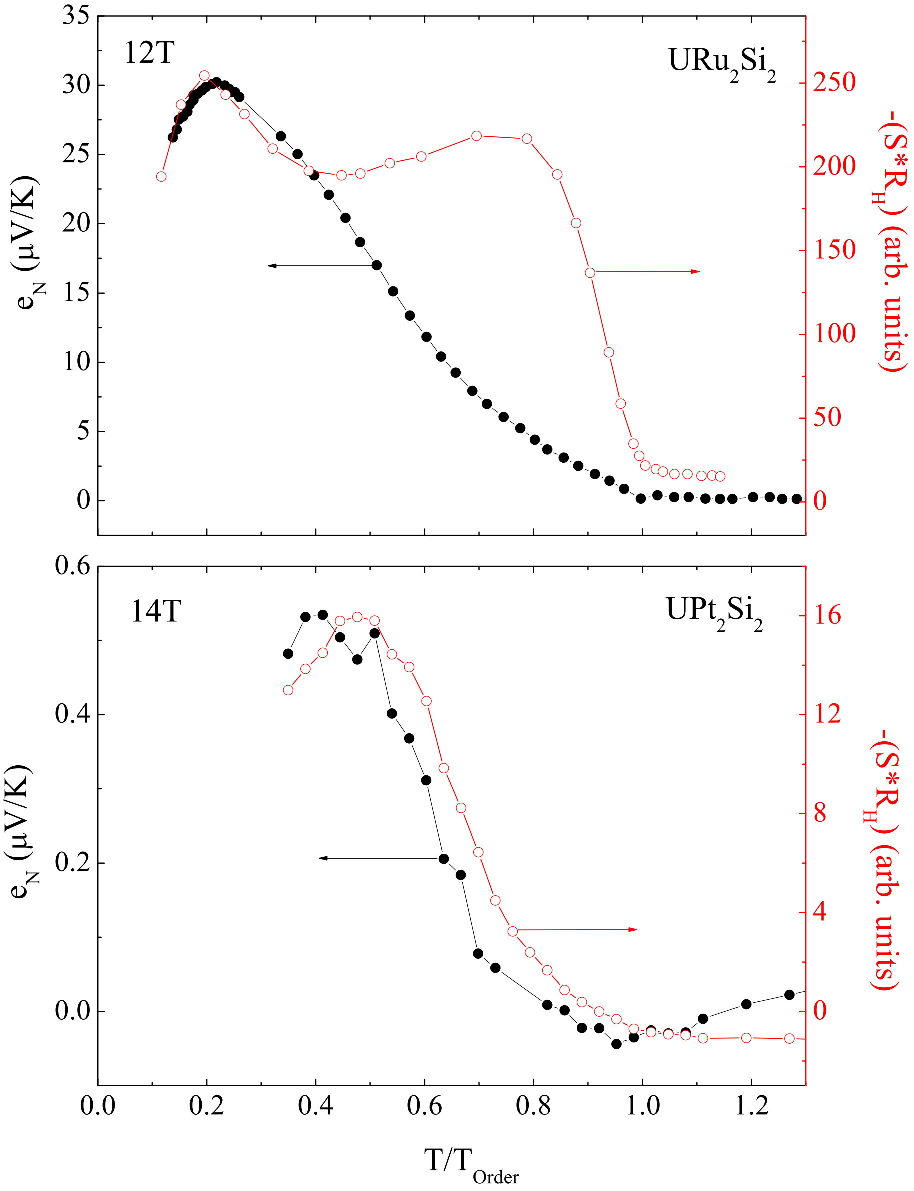

Figure 8.11: Upper panel: The Nernst signal of URu_2Si_2 compared to the product of its thermopower and Hall coefficient at $H = 12\,T$. Data are taken from [11] with a $T_{Order} = T_{HO} = 17.5\,K$. The lower panel depicts the scaling behavior for UPt_2Si_2 as expected from calculations for a generic antiferromagnet due to the opening of a superzone gap [14]. The maximum positions of roughly $0.5 \cdot T_{Order}$ well agree with the theoretical expectations. Here, $T_{Order} = T_N = 31.5\,K$.

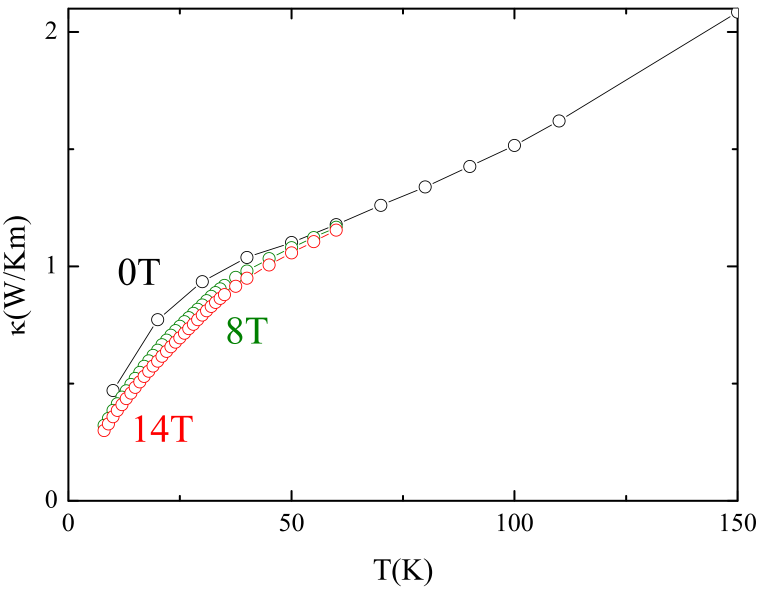

Figure 8.12: Thermal conductivity of UPt_2Si_2 for the denoted fields along the c axis. Magnetic Field is applied along a.

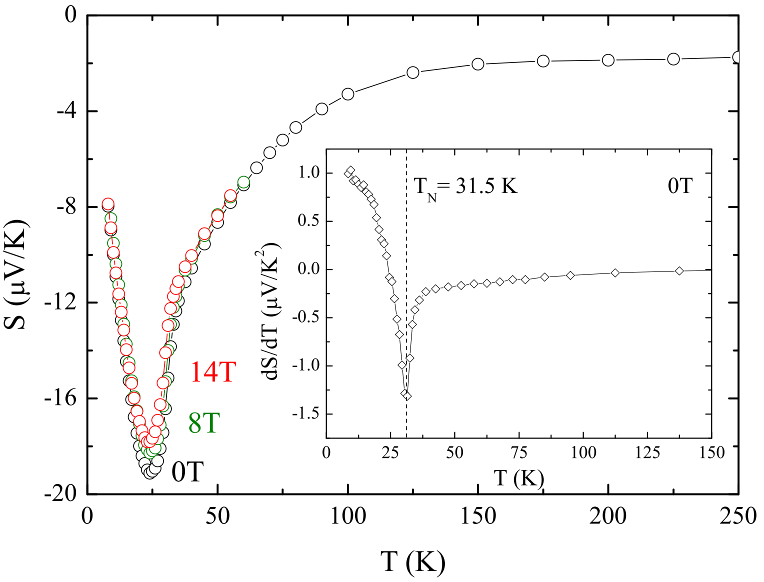

Figure 8.13: Thermopower of UPt_2Si_2 for 0, 8T and 14T. ∇T is directed along the c axis while $B||a$. Inset: Temperature derivative of the zero-field thermopower. The transition into the antiferromagnetic state shows up as a clear peak at 31.5 K.

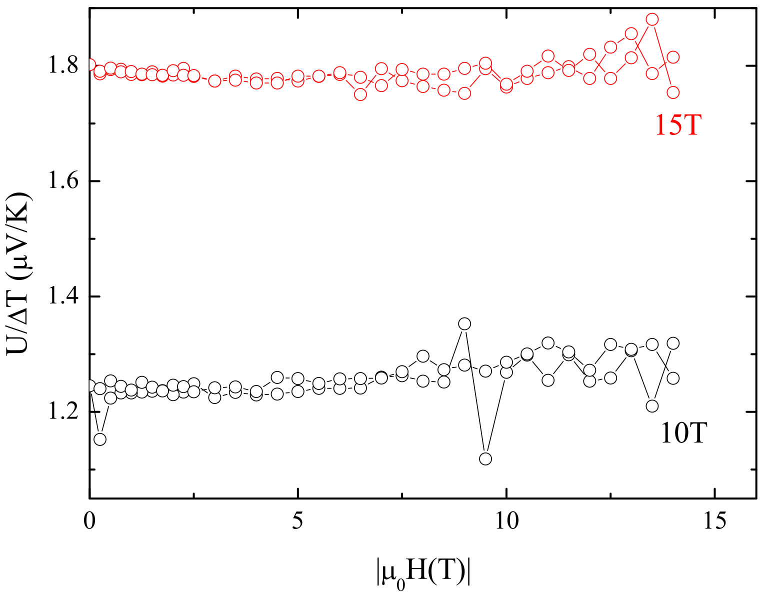

Figure 8.14: Raw voltage of the Nernst contacs divided by the applied temperature gradient for 10 K and 15 K. It is clearly seen already by eye, that no antisymmetric signals can be extracted but noise. Please note the pronounced difference to the raw voltages for $\nabla T||a, B||c$ in the inset of Fig. 8.8.

8.4.3 Conclusion

To summarize the results derived for the thermal transport measurements along the c axis, they very well fit into the picture of localized electronic transport reported by refs. [12, 231]. A Nernst signal could not be resolved. The magnitude of the thermopower is larger than along a which is in agreement with expectations from the simple free-electron estimation of Eq. 3.8: The lower the charge carrier concentration the larger the thermopower. The thermal conductivity displays the characteristics that are expected for amorphous or glass-like structures. Furthermore, the magnetic field dependences of all transport properties along this direction are nearly absent.

Not so for the thermal and electronic transport measured along a. Here, pronouced increases of the Nernst effect, the thermopower and the Hall coefficient are detectable. The thermal conductivity was found to be predominantly phononic with a strong magnetic field dependence indicating that spin fluctuations play an important role as scatterer of phonons. The resistivity is rather flat at high temperatures and shows a knee-like decrease below T_N. Thus, UPt$_2$Si$_2$ is metallic along a and localized along c. A theory, already developed in 1972 by Abelskii and Dik [13, 14] calculated the thermopower and the Nernst effect in generic antiferromagnets assuming a superzone gap opening at T_N. The according measurements presented here are in very good agreement with these predictions. Furthermore, we could attribute this gap opening to only a portion of the Fermi surface. Otherwise, a metal to insulator transition would be visible in the behavior of the resistivity.

9 Summary

In this thesis, the Nernst effect in high-temperature superconductors is investigated. This effect gained much interest because it is usually very small in ordinary metals, but was found to display a large signal in the vortex liquid phase of the high-T_c's. The Nernst effect is a thermo-magnetic effect that occurs when a temperature gradient and a magnetic field are applied to the sample. The voltage that develops transverse to both external sources is the Nernst voltage. The generation of voltages is of different origin in the high-T_c's compared to normal conducting materials. As a consequence of the Josephson equations, moving vortices produce a perpendicular voltage. A vortex appears in the vortex-liquid state of the high-T_c's and can be thought of as a magnetic flux line that penetrates the bulk of the sample and is encircled by a Cooper-pair supercurrent. In order to make such a structure move through the sample, either an electric current or a temperature gradient has to be applied. Since supercurrents are involved, vortices and thereby pronounced Nernst voltages are intimately related to the superconducting phase. Thus, it really was a surprise that large Nernst voltages survive up to temperatures that reach far out of the superconducting phase [4]. This was extensively studied thereafter in a wide doping range of the high-T_c's [9]. The generic phase diagram of the high-T_c compounds starts at zero doping in an antiferromagnetic phase. With increasing hole doping concentrations, this phase breaks down relatively fast. A few percent more charge carriers already lead to the onset of superconductivity. The corresponding T_c values increase with further hole doping concentrations until a maximum is reached. The corresponding doping concentration is referred to as "optimally" doped. Lower concentrations define the "underdoped" region. The whole superconducting region has the shape of a dome and is therefore given the name "superconducting dome". Long before large Nernst signals were found above T_c, other measurements already indicated that the phase that is found above T_c, especially at the underdoped side, behaves quite distinct from a normal metal. At temperatures roughly as high as room temperature, signatures of reduced density of states were indicated by optical conductivity measurements [5]. Because of this "only" reduced density of states, the phase that is exhibited above T_c in the underdoped region of the high-T_c's is called "pseudogap" phase. The close relation of anomalous Nernst signals and vortices or vortex-like excitations make such measurements predestined to investigate the nature of the pseudogap phase which is found up to the crossover temperature T^*. This was done mostly by scanning the region above the superconducting dome in the underdoped samples.

We were able to significantly expand these studies. Given the opportunity to simultaneously tune T^* and T^ν by inducing Ni ions into the CuO planes [10], the Nernst effect is systematically investigated in a wide temperature range from below T_c to high above. The investigated system is $\mathrm{NdBa_2\{Cu_{1\text{-}y}Ni_y\}_3O_{7-\delta}}$. This is done on one hand in dependence of the oxygen content which varies the charge carrier concentration. On the other hand, the Ni concentration is varied from 0% to 12%, thereby enhancing T^* and simultaneously suppressing T_c with increasing Ni concentrations. So to say, a third axis is accessed in the phase diagram of the cuprates. The temperatures to which the anomalous Nernst signal is detectable is the onset temperature T^ν. The goal of this work was to find out whether T^ν follows T_c or T^*, since both can be influenced by altering the charge carrier content or the impurity concentration. The onset temperatures of the anomalous Nernst signals are determined as the slightest detectable deviation from the quasiparticle background above T_c. The Ni-dependent T^ν are found at temperatures of $T^\nu \simeq T_c + 20K$ for $\mathrm{NdBa_2\{Cu_{1\text{-}y}Ni_y\}_3O_7}$ with y=0,3%,6%,12%. The next step is to alter the charge carrier concentration by reducing the oxygen content to $\mathrm{NdBa_2\{Cu_{1\text{-}y}Ni_y\}_3O_{6.9}}$. Going from y=0% Ni ($T_c = 82\,\mathrm{K}$) to y=3% Ni ($T_c = 38\,\mathrm{K}$), T^ν is only slightly reduced from ≃95 K to ≃80 K, respectively. In $\mathrm{NdBa_2\{Cu_{1\text{-}y}Ni_y\}_3O_{6.8}}$, T^ν stays nearly constant at ≃80 K for y=0% and y=3%Ni. Overall, since the pseudogap is drastically increased with increasing Ni concentrations, T^ν clearly does not track the enhanced pseudogap in any sample series that is investigated in this work [24]. This and other results [178, 202] indicate that there remain questions in the interpretation of the pseudogap phase in terms of preformed pairs only. Now, theories are challenged to bring the results of the onsets of anomalous Nernst signals in the pseudogap phase of different high-T_c systems into a consistent picture.

In the second part of this work the Nernst effect and other transport properties of $\mathrm{UPt_2Si_2}$, including electrical ones such as the resistivity and the Hall effect and thermal transport properties such as the thermal conductivity, the thermopower and the Righi-Leduc effect were investigated. These investigations were motivated by the findings of a giant Nernst effect in the related system $\mathrm{URu_2Si_2}$ [11]. Although $\mathrm{URu_2Si_2}$ is superconducting, the Nernst signal is found to emerge at temperatures clearly above T_c ≈1.5 K and is not attributed to the superconducting phase. It is related to a reduction of the Fermi energy due to a depletion of charge carriers upon entering the mysterious "hidden order" [45, 213, 214] phase at about 17 K [11]. In contrast to $\mathrm{URu_2Si_2}$, $\mathrm{UPt_2Si_2}$ is neither superconducting, nor does it belong to the class of the "heavy Fermions". It forms a local-moment antiferromagnetic ground state [12]. Nevertheless, a Nernst signal emerges at the onset of the antiferromagnetic transition in $\mathrm{UPt_2Si_2}$. It displays a linear magnetic field dependence and forms a maximum at about $15\,\mathrm{K} \simeq T_N/2$. Additionally, the thermopower and the Hall effect are also subjected to a pronounced increase upon crossing into the antiferromagnetic phase. For $\mathrm{URu_2Si_2}$, it has been argued that large Nernst signals can arise from long scattering times and small Fermi energies. In order to establish this relation of $\omega_0\tau/\epsilon_F \propto e_N$ fine structures in the energy dependence of τ at the Fermi energy have been disregarded. Such an approach is, however, not describing the data for $\mathrm{UPt_2Si_2}$. In an early theory, published in 1972, Abelskii and Dik *et al.* [13, 14] calculated the thermopower and the Nernst coefficient for a generic antiferromagnet under the assumption of a gapping of the Fermi surface at T_N in addition to phonon and spin scattering mechanisms. These calculations astonishingly well predict the behavior of the measured quantities of $\mathrm{UPt_2Si_2}$. Not only the onsets of the signals and the maxima positions meet the forecasts of the theory, but also the predicted scaling $S \cdot R_H \propto e_N$ is well fulfilled by the measured data of UPt_2Si_2. Thus, the emergence of the Nernst signal is ascribed to an opening of a gap at the Fermi surface. Yet, this gapping cannot affect the whole Fermi surface, otherwise the system would undergo a metal-to-insulator transition, which is not seen in the resistivity [26]. This scenario of a partial gapping is consistent with a recent publication of electronic transport and neutron diffraction studies [12]. Since such a partial gap exists also in URu_2Si_2, the large Nernst signal in found in this substance might also be related to the gapped region of the Fermi surface.

List of Figures

3.1 Illustration of the Seebeck effect. 12
3.2 Illustration of the Nernst effect in metals. 14
3.3 Comparison of the overall magnitude of Nernst signals[39] 17
3.4 Ambipolar Nernst Effect in $NbSe_2$ [40] 18
3.5 Nernst Effect in URu_2Si_2[11] 19
3.6 e_N and α_{xy} vs magnetic field in $CeCoIn_5$ 20
3.7 Nernst signals scale with magnetization in ferromagnets[58] 21

4.1 Junction of normal and superconducting material. 25
4.2 Magnetization of type-I and type-II superconductors. 26
4.3 Illustration of magnetic flux lines in a type-II superconductor. 26
4.4 Schematic phase diagram of type II superconductors 28
4.5 Vortex melting lines for two optimally doped samples 29
4.6 Voltage generation by moving vortices 30
4.7 Hall angle of Vortices 33
4.8 Resistive Voltage in Niobium 34
4.9 Transverse temperature gradient vs. longitudinal voltage 35
4.10 Peltier effect in $Bi_{1.76}Pb_{0.24}Sr_2Ca_2Cu_3O_\delta$ 36
4.11 Spectrum of particles in the vortex core 37
4.12 Forces acting on a vortex in a current driven resistive state. 39
4.13 Current driven vortex motion, spectral flow effect 40
4.14 Simple sketch of thermal driven vortex flow. 42
4.15 Structure of $NdBa_2Cu_3O_7$ 44
4.16 Structure development with oxygen doping 45
4.17 Phase diagram Cuprates 48
4.18 Phase diagram $YBCO_{6+x}$ 48
4.19 Copper Oxygen layers, development with doping 49
4.20 Development of the Fermi surface from superconducting to normal state . . 51
4.21 Three different pseudogap models 51

5.1 Polished surface of $NdBa_2(Cu_{0.97}Ni_{0.03})O_7$ 54
5.2 Schematic drawing of sample preparation 55
5.3 Nernst contacts vs. a fixing pin 56
5.4 Field dependence of offset voltages 58
5.5 Effect of different chip heater currents on sample temperature 59
5.6 Independence of Nernst effect on sweep rate 60

5.7 Raw voltage of Nernst and thermopower contacts 62
5.8 Symmetric and antisymmetric parts of the contacts 62
5.9 Maximum geometry error estimation. 64
5.10 $e_N(T,B)$ of $La_{1.93}Sr_{0.07}CuO_4$ 65
5.11 Contour plot LSCO and $e_N(T,B)$ of $La_{1.93}Sr_{0.07}CuO_4$ [9]. 65

6.1 Contour plot of LSCO and $e_N(T,B)$ in LSCO, x=0.12 [9] 68
6.2 Diamagnetism and Nernst signal in Bi2212 [174, 175] 69
6.3 Optical conductivity of $NdBa_2\{Cu_{1-y}Ni_y\}_3O_{6.8}$ [10] 69
6.4 3D sketch of the Ni influence on T_c and T^* 70

7.1 Contact scheme for the magneto-thermal transport measurements 73
7.2 κ_{xx} and κ_{xy} in YBCO [36] 75
7.3 $\kappa(T,B)$ in O_7 for different Ni concentrations 76
7.4 $\kappa(T,B)$ in $O_{6.9}$ for different Ni concentrations 78
7.5 $\kappa(T,B)$ in $O_{6.9}$ for different Ni concentrations 78
7.6 $S(T)$ of $NdBa_2Cu_3O_{7-\delta}$, δ =0, 0.1, 0.2 81
7.7 $S(T)$ of $YBa_2Cu_3O_{7-\delta}$ [129, 192] 81
7.8 $S(T)$ of O_7 for different Ni concentrations 83
7.9 $S(T)$ of $O_{6.9}$ for different Ni concentrations 84
7.10 $S(T)$ of $O_{6.8}$ for different Ni concentrations 84
7.11 $S(B)$ in O_7 85
7.12 $S(B)-S(0)$ in O_7 86
7.13 $S(B)$ in $O_{6.8}$ 86
7.14 $S(B)-S(0)$ in $O_{6.8}$ 87
7.15 $e_N(B)$ in $NdBa_2\{Cu_{1\text{-y}}Ni_y\}_3O_{7-\delta}$ for $\delta=0$ and Ni=0,.03,.06,.12 88
7.16 $e_N(B)$ in $NdBa_2\{Cu_{1\text{-y}}Ni_y\}_3O_{7-\delta}$ for $\delta=0.2$ and Ni=0,.03,.06 89
7.17 $e_N(B)$ in $NdBa_2\{Cu_{1\text{-y}}Ni_y\}_3O_{7-\delta}$ for $\delta=0.1$ and Ni=0,.03 90
7.18 T^ν of $NdBa_2\{Cu_{1-x}Ni_x\}_3O_{7-\delta}$ for $\delta=0,0.1$ and different Ni concentrations 92
7.19 T^ν of Ni=0,0.03 for $NdBa_2\{Cu_{1\text{-y}}Ni_y\}_3O_{7-\delta}$ with $\delta=0,0.1,0.2$ 93
7.20 Phase diagram T^ν vs T_c 94
7.21 T^ν vs T_c in Irradiated YBCO [178] 94
7.22 Revised phase diagram of the cuprates [204] 95
7.23 Thermal Hall angle O_7, $T<T_c$ 97
7.24 Thermal Hall angle O_7, $T\sim T_c$ 98
7.25 Thermal Hall angle $O_6.8$ 98
7.26 Thermal Hall angle LSCO, x=0.15 99

8.1 Sketch of the origin of the Kondo temperature, single impurity case 102
8.2 Structure and χ of UPt_2Si_2 104
8.3 Resistivity of UPt_2Si_2 105
8.4 $d\rho/dT$ of UPt_2Si_2 105

8.5 Comparison of the antisymmetric raw voltages of longitudinal and transversal electric contacts . . . 106
8.6 Thermal conductivity of UPt_2Si_2 along a . . . 107
8.7 Thermopower of UPt_2Si_2 for magnetic fields of 0, 8 T, and 14 T . . . 108
8.8 Nernst signal of UPt_2Si_2 . . . 109
8.9 $e_N/T = N/T$ vs Hall angle in URu_2Si_2 and UPt_2Si_2 . . . 111
8.10 Calculated temperature dependences of e_N and S in antiferromagnets . . . 112
8.11 e_N vs. $S \cdot R_H$ . . . 114
8.12 Thermal conductivity of UPt_2Si_2 along c . . . 115
8.13 Thermopower of UPt_2Si_2 along c . . . 115
8.14 Raw voltage of the Nernst contacts for 10 K and 15 K, $\nabla T || c$ . . . 116

Bibliography

[1] J.G. Bednorz and K.A. Müller. Z. Physik B **64**, 189–193 (1986).

[2] L.N. Cooper. Phys. Rev. **104**, 1189 (1956).

[3] A.V. Ettingshausen and W. Nernst. Wied. Ann. **29**, 343 (1886).

[4] Z.A. Xu, N.P. Ong, Y. Wang, T. Kakeshita, and S. Uchida. Nature **406**, 486 (2000).

[5] C.C. Homes, T. Timusk, R. Liang, D.A. Bonn, and W.N. Hardy. Phys. Rev. Lett. **71**, 1645 (1993).

[6] W.W. Warren, R.E. Walstedt, G.F. Brennert, R.J. Cava, R. Tycko, R.F. Bell, and G. Dabbagh. Phys. Rev. Lett. **62**, 1193 (1989).

[7] H. Alloul, T. Ohno, and P. Mendels. Phys. Rev. Lett. **63**, 1700 (1989).

[8] D.C. Johnston. Phys. Rev. Lett. **62**, 957 (1989).

[9] Y. Wang, L. Li, and N.P. Ong. Phys. Rev. B **73**, 024510 (2006).

[10] A.V. Pimenov, A.V. Boris, L. Yu, V. Hinkov, T. Wolf, J.L. Tallon, B. Keimer, and C. Bernhard. Phys. Rev. Lett. **94**, 227003 (2005).

[11] R. Bel, H. Jin, K. Behnia, J. Flouquet, and P. Lejay. Phys. Rev. B **70**, 220501 (2004).

[12] S. Suellow, A. Otop, A. Loose, J. Klenke, O. Prokhnenko, R. Feyerherm, R.W.A. Hendrikx, J.A. Mydosh, and H. Amitsuka. J. Phys. Soc. Jpn. **77**, 024708 (2008).

[13] S.S. Abelskii and Y.P. Irkhin. Soviet Physics - Solid State **13**, 2035 (1972).

[14] E.G. Dik and S.S. Abelskii. Soviet Physics - Solid State **17**, 454 (1975).

[15] L.D. Landau and E.M. Lifschitz. *Lehrbuch der Theoretischen Physik, Bd. V:Statistische Physik I.* Akademie Verlag Berlin (1987).

[16] S.R.de Groot and P. Masur. *Grundlagen der Thermodynamik irreversibler Prozesse.* BI-Hochschultaschenbücher 162/162a (1969).

[17] N.W. Ashcroft and N.D. Mermin. *Solid State Physics.* Saunders College Publishing New York (1976).

[18] F. Reif. *Fundamentals of Statistical and Thermal Physics.* McGraw-Hill (1985).

[19] W. Greiner, L. Neise, and H. Stöcker. *Thermodynamik und Statistische Mechanik* volume 9. Verlag Harri Deutsch (1993).

[20] T. Fließbach. *Statistische Physik.* Spektrum Akademischer Verlag GmbH 3. edition (1999).

[21] E. Gratz and H. Nowotny. *Transportphaenomene in Festkoerpern.* Vorlesungsskript (2004).

[22] M. Galffy. PhD thesis, Universität zu Köln (1990).

[23] A.S. Alexandrov and V.N. Zavaritsky. Phys. Rev. Lett. **93**, 217002 (2004).

[24] N. Johannsen, T. Wolf, A.V. Sologubenko, T. Lorenz, A. Freimuth, and J.A. Mydosh. Phys. Rev. B **76**, 020512 (2007).

[25] Y.Y. Wang, Z.A. Xu, T. Kakeshita, S. Uchida, S. Ono, Y. Ando, and N.P. Ong. Phys. Rev. B **64**, 224519 (2001).

[26] N. Johannsen, S. Süllow, A. V. Sologubenko, T. Lorenz, and J. A. Mydosh. arXiv:0804.1318 (2008).

[27] D.V. Livanov. Phys. Rev. B **60**, 13439 (1999).

[28] T.J. Seebeck. Abh. der Preussischen Akademie der Wiss. pages 265–373 (1822-23).

[29] F.J. Blatt and P.A. Schroeder. *Thermoelectric Power of Metals.* Plenum Press New York (1976).

[30] J.M. Ziman. *Principles of the Theory of Solids.* Cambridge University Press (1972).

[31] A. Abrikosov. *Fundamentals of the Theory of Metals.* North-Holland (1988).

[32] R.D. Barnard. *Thermoelectricity in Metals and Alloys.* Taylor and Francis Ltd London (1972).

[33] A.J. Millis and P.A. Lee. Phys. Rev. B **35**, 3394 (1987).

[34] J.L. Cohn, S.A. Wolf, V. Selvamanickam, and K. Salama. Phys. Rev. Lett. **66**, 1098 (1991).

[35] Y. Zhang, N.P. Ong, Z.A. Xu, K. Krishana, R. Gagnon, and L. Taillefer. Phys. Rev. Lett. **84**, 2219 (2000).

[36] B. Zeini, A. Freimuth, B. Buchner, R. Gross, A.P. Kampf, M. Klaser, and G. Muller-Vogt. Phys. Rev. Lett. **82**, 2175 (1999).

[37] H.C. Ri, R. Gross, F. Gollnik, A. Beck, R.P. Huebener, P. Wagner, and H. Adrian. Phys. Rev. B **50**, 3312 (1994).

[38] E.H. Sondheimer. Proc. R. Soc. Lond. A **193**, 484 (1948).

[39] K. Behnia, M.A. Measson, and Y. Kopelevich. Phys. Rev. Lett. **98**, 076603 (2007).

[40] R. Bel, K. Behnia, and H. Berger. Phys. Rev. Lett. **91**, 066602 (2003).

[41] T. Yokoya, T. Kiss, A. Chainani, S. Shin, M. Nohara, and H. Takagi. Science **294**, 2518 (2001).

[42] R.T. Delves. Rep. Prog. Phys. **28**, 249 (1965).

[43] P.J. Price. Phys. Rev. **104**, 1223 (1956).

[44] R. Okazaki, Y. Kasahara, H. Shishido, M. Konczykowski, K. Behnia, Y. Haga, T.D. Matsuda, Y. Onuki, T. Shibauchi, and Y. Matsuda. Phys. Rev. Lett. **100**, 037004 (2008).

[45] T.T.M. Palstra, A.A. Menovsky, J. Vandenberg, A.J. Dirkmaat, P.H. Kes, G.J. Nieuwenhuys, and J.A. Mydosh. Phys. Rev. Lett. **55**, 2727 (1985).

[46] C. Broholm, J.K. Kjems, W.J.L. Buyers, P. Matthews, T.T.M. Palstra, A.A. Menovsky, and J.A. Mydosh. Phys. Rev. Lett. **58**, 1467 (1987).

[47] V. Barzykin and L.P. Gorkov. Phys. Rev. Lett. **70**, 2479 (1993).

[48] P. Santini and G. Amoretti. Phys. Rev. Lett. **73**, 1027 (1994).

[49] A.E. Sikkema, W.J.L. Buyers, I. Affleck, and J. Gan. Phys. Rev. B **54**, 9322 (1996).

[50] Y. Okuno and K. Miyake. J. Phys. Soc. Japan **67**, 2469 (1998).

[51] H. Ikeda and Y. Ohashi. Phys. Rev. Lett. **81**, 3723 (1998).

[52] P. Chandra, P. Coleman, J.A. Mydosh, and V. Tripathi. Nature **417**, 831 (2002).

[53] N. Keller, S.A.J. Wiegers, J.A.A.J. Perenboom, A. de Visser, A.A. Menovsky, and J.J.M. Franse. J. Magn. Magn. Mat. **177**, 298 (1998).

[54] C. Petrovic, P.G. Pagliuso, M.F. Hundley, R. Movshovich, J.L. Sarrao, J.D. Thompson, Z. Fisk, and P. Monthoux. J. Phys. – Condens. Matter **13**, L337 (2001).

[55] H. Kontani. Phys. Rev. Lett. **89**, 237003 (2002).

[56] M.R. Norman, Q.M. Si, Y.B. Bazaliy, and R. Ramazashvili. Phys. Rev. Lett. **90**, 116601 (2003).

[57] Y. Onose, L. Li, C. Petrovic, and N.P. Ong. EPL **79**, 17006 (2007).

[58] T. Miyasato, N. Abe, T. Fujii, A. Asamitsu, S. Onoda, Y. Onose, N. Nagaosa, and Y. Tokura. Phys. Rev. Lett. **99**, 086602 (2007).

[59] Alpheus W. Smith. Phys. Rev. **17**(1), 23–37 (Jan 1921).

[60] W.L. Lee, S. Watauchi, V.L. Miller, R.J. Cava, and N.P. Ong. Phys. Rev. Lett. **93**, 226601 (2004).

[61] Y. Taguchi, Y. Oohara, H. Yoshizawa, N. Nagaosa, and Y. Tokura. Science **291**, 2573 (2001).

[62] R. Karplus and J.M. Luttinger. Phys. Rev. **95**, 1154 (1954).

[63] J.W. Ye, Y.B. Kim, A.J. Millis, B.I. Shraiman, P. Majumdar, and Z. Tesanovic. Phys. Rev. Lett. **83**, 3737 (1999).

[64] J. Smit. Physica **21**, 877 (1955).

[65] L. Berger. Phys. Rev. B **2**, 4559 (1970).

[66] H. Kamerlingh Onnes. Communications from the Physical Laboratory of the University of Leiden **124c**, 818 (1911).

[67] W. Meissner and R. Ochsenfeld. Naturwissenschaften **21**, 787 (1933).

[68] W. Buckel. *Supraleitung.* VCH Verlagsgesellschaft mbH 5. edition (1994).

[69] C. Kittel. *Einführung in die Festkörperphysik.* R. Oldenburg Verlag 12. edition (1999).

[70] M. Tinkham. *Introduction to Superconductivity.* McGraw-Hill International Editions 2. edition (1996).

[71] J.B. Ketterson and S.N. Song. *Superconductivity.* Cambridge University Press (1999).

[72] V.V. Schmidt. *The Physics of Superconductors.* Springer Verlag Berlin Heidelberg New York (1997).

[73] R.P. Huebener. *Magnetic Flux Structures in Superconductors.* Springer Verlag Berlin Heidelberg New York (1979).

[74] A.A. Abrikosov. SOVIET PHYSICS JETP-USSR **5**, 1174 (1957).

[75] M.R. Eskildsen, M. Kugler, S. Tanaka, J. Jun, S.M. Kazakov, J. Karpinski, and O. Fischer. Phys. Rev. Lett. **89**, 187003 (2002).

[76] J. Bardeen, L.N. Cooper, and J.R. Schrieffer. Phys. Rev. **108**, 1175 (1957).

[77] G. Blatter and B.I. Ivlev. Phys. Rev. B **50**, 10272 (1994).

[78] G. Blatter, B. Ivlev, Y. Kagan, M. Theunissen, Y. Volokitin, and P. Kes. Phys. Rev. B **50**, 13013 (1994).

[79] A. Houghton, R.A. Pelcovits, and A. Sudbo. Phys. Rev. B **40**, 6763 (1989).

[80] D.S. Fisher, M.P.A. Fisher, and D.A. Huse. Phys. Rev. B **43**, 130 (1991).

[81] P.W. Anderson. Rev. Mod. Phys. **38**, 298 (1966).

[82] A. Freimuth. *Vortices in Unconventional Superconductors and Superfluids* chapter Vortex Dynamics in a Temperature Gradient, pages 321–339. Springer Series in Solid-State Sciences 2002.

[83] H. Lamb. *Hydrodynamics.* Dover Publications, Inc. (1932).

[84] E.B. Sonin. Phys. Rev. B **55**, 485 (1997).

[85] P. Nozieres and W.F. Vinen. Philosophical Magazine **14**, 667 (1966).

[86] H.C. Ri, F. Kober, A. Beck, L. Alff, R. Gross, and R.P. Huebener. Phys. Rev. B **47**, 12312 (1993).

[87] A.G. Van Vijfeijken and A.K. Niessen. Phillips. Res. Rep. **20**, 505 (1965).

[88] A.G. Van Vijfeijken. Phillips Res. Rep. Suppl. **8**, 1 (1968).

[89] A.G. Van Vijfeijken and A.K. Niessen. Physics Lett. **16**, 23 (1965).

[90] P.G. Degennes and J. Matricon. Rev. Mod. Phys. **36**, 45 (1964).

[91] P.G. DeGennes. *Superconductivity of Metals and Alloys.* W.A. Benjamin (1966).

[92] M. Gálffy. PhD thesis, Universität zu Köln (1990).

[93] C. Hohn. PhD thesis, Universität zu Köln (1994).

[94] A. Dascoulidou, M. Galffy, C. Hohn, N. Knauf, and A. Freimuth. Physica C **201**, 202 (1992).

[95] A. Freimuth. *Superconductivity, Frontiers in Solid State Sciences Vol.1* chapter Transport Properties in the Mixed State of High Temperature Superconductors, pages 393–449. World-Scientific, Singapore 1992.

[96] M. Galffy, A. Freimuth, and U. Murek. Phys. Rev. B **41**, 11029 (1990).

[97] R.P. Huebener, R.T. Kampwirth, and A. Seher. J. Low Temp. Phys. **2**, 113 (1970).

[98] J. Lowell, J.S. Munoz, and J.B. Sousa. Phys. Rev. **183**, 497 (1969).

[99] V.A. Rowe and R.P. Huebener. Phys. Rev. B **2**, 4489 (1970).

[100] P.R. Solomon and F.A. Otter. Phys. Rev. **164**, 608 (1967).

[101] M. Galffy, C. Hohn, and A. Freimuth. Annalen der Physik **3**, 215 (1994).

[102] M. Stone. Phys. Rev. B **54**, 13222 (1996).

[103] T.D.C. Bevan, A.J. Manninen, J.B. Cook, J.R. Hook, H.E. Hall, T. Vachaspati, and G.E. Volovik. Nature **386**, 689 (1997).

[104] C. Caroli, P.G. Degennes, and J. Matricon. Physics Lett. **9**, 307 (1964).

[105] N.B. Kopnin and G.E. Volovik. Phys. Rev. Lett. **79**, 1377 (1997).

[106] Y.G. Makhlin. Phys. Rev. B **56**, 11872 (1997).

[107] D. Rainer, J.A. Sauls, and D. Waxman. Phys. Rev. B **54**, 10094 (1996).

[108] N.B. Kopnin, G.E. Volovik, and U. Parts. Europhys. Lett. **32**, 651 (1995).

[109] N.B. Kopnin and V.E. Kravtsov. Zh. Eks. I Teor. Fiziki **71**, 1645 (1976).

[110] N.B. Kopnin and M.M. Salomaa. Phys. Rev. B **44**, 9667 (1991).

[111] N.B. Kopnin. Phys. Rev. B **47**, 14354 (1993).

[112] N.B. Kopnin and A.V. Lopatin. Phys. Rev. B **51**, 15291 (1995).

[113] A. Freimuth and M. Zittartz. Phys. Rev. Lett. **84**, 4978 (2000).

[114] M.J. Stephen. Phys. Rev. Lett. **16**, 801 (1966).

[115] Y.B. Kim and M.J. Stephen. *Superconductivity, Vol.2* chapter Flux Flow and Irreversible Effects, pages 1107–1165. World-Scientific, Singapore 1969.

[116] R.P. Huebener. Supercond. Sci. Tech. **8**, 189 (1995).

[117] F. Prado, A. Caneiro, and A. Serquis. Physica C **295**, 235 (1998).

[118] T.A. Zaleski and T.K. Kopec. Phys. Rev. B **74**, 014504 (2006).

[119] Y. Iye. *Physical properties of High-Temperature superconductors III* chapter Transport Properties of High Tc Cuprates. World Scientific 1992.

[120] Y. Iye. Comments Cond. Mat. Phys. **16**, 89 (1992).

[121] D.E. Farrell, C.M. Williams, S.A. Wolf, N.P. Bansal, and V.G. Kogan. Phys. Rev. Lett. **61**, 2805 (1988).

[122] D.E. Farrell, S. Bonham, J. Foster, Y.C. Chang, P.Z. Jiang, K.G. Vandervoort, D.J. Lam, and V.G. Kogan. Phys. Rev. Lett. **63**, 782 (1989).

[123] P.A. Lee. Phys. Rev. Lett. **71**, 1887 (1993).

[124] G. Preosti, H.S. Kim, and P. Muzikar. Phys. Rev. B **50**, 13638 (1994).

[125] Y. Sun and K. Maki. Phys. Rev. B **51**, 6059 (1995).

[126] P.J. Hirschfeld and N. Goldenfeld. Phys. Rev. B **48**, 4219 (1993).

[127] J.W. Loram, K.A. Mirza, and P.F. Freeman. Physica C **171**, 243 (1990).

[128] H. Alloul, P. Mendels, H. Casalta, J.F. Marucco, and J. Arabski. Phys. Rev. Lett. **67**, 3140 (1991).

[129] S.D. Obertelli, J.R. Cooper, and J.L. Tallon. Phys. Rev. B **46**, 14928 (1992).

[130] J.L. Tallon, J.R. Cooper, P.S.I.P.N. Desilva, G.V.M. Williams, and J.W. Loram. Phys. Rev. Lett. **75**, 4114 (1995).

[131] C. Bernhard, J.L. Tallon, C. Bucci, R. DeRenzi, G. Guidi, G.V.M. Williams, and C. Niedermayer. Phys. Rev. Lett. **77**, 2304 (1996).

[132] P. Monthoux, A.V. Balatsky, and D. Pines. Phys. Rev. B **46**, 14803 (1992).

[133] T. Moriya, Y. Takahashi, and K. Ueda. J. Phys. Soc. Japan **59**, 2905 (1990).

[134] N.E. Bickers, D.J. Scalapino, and S.R. White. Phys. Rev. Lett. **62**, 961 (1989).

[135] P. Monthoux and D. Pines. Phys. Rev. B **49**, 4261 (1994).

[136] D. Pines. Physica C **282**, 273 (1997).

[137] P. Mendels, H. Alloul, G. Collin, N. Blanchard, J.F. Marucco, and J. Bobroff. Physica C **235**, 1595 (1994).

[138] E.W. Hudson, K.M. Lang, V. Madhavan, S.H. Pan, H. Eisaki, S. Uchida, and J.C. Davis. Nature **411**, 920 (2001).

[139] T.B. Lindemer, E.D. Specht, P.M. Martin, and M.L. Flitcroft. Physica C **255**, 65 (1995).

[140] Y.K. Kuo, C.W. Schneider, M.J. Skove, M.V. Nevitt, G.X. Tessema, and J.J. McGee. Phys. Rev. B **56**, 6201 (1997).

[141] Z.A. Xu, J.Q. Shen, S.R. Zhao, Y.J. Zhang, and C.K. Ong. Phys. Rev. B **72**, 144527 (2005).

[142] M.R. Presland, J.L. Tallon, R.G. Buckley, R.S. Liu, and N.E. Flower. Physica C **176**, 95 (1991).

[143] J.L. Tallon, C. Bernhard, H. Shaked, R.L. Hitterman, and J.D. Jorgensen. Phys. Rev. B **51**, 12911 (1995).

[144] J.M. Tranquada, D.E. Cox, W. Kunnmann, H. Moudden, G. Shirane, M. Suenaga, P. Zolliker, D. Vaknin, S.K. Sinha, M.S. Alvarez, A.J. Jacobson, and D.C. Johnston. Phys. Rev. Lett. **60**, 156 (1988).

[145] N.F. Mott. *Metal-Insulator Transitions.* Taylor and Francis London (1990).

[146] M. Kriener. PhD thesis, Universität zu Köln (2005).

[147] S.L. Cooper, G.A. Thomas, A.J. Millis, P.E. Sulewski, J. Orenstein, D.H. Rapkine, S.W. Cheong, and P.L. Trevor. Phys. Rev. B **42**, 10785 (1990).

[148] K. Berggold. PhD thesis, Universität zu Köln (2006).

[149] M.A. Kastner, R.J. Birgeneau, G. Shirane, and Y. Endoh. Rev. Mod. Phys. **70**, 897 (1998).

[150] M.R. Norman, D. Pines, and C. Kallin. Adv. in Phys. **54**, 715 (2005).

[151] J.M. Tranquada, A.H. Moudden, A.I. Goldman, P. Zolliker, D.E. Cox, G. Shirane, S.K. Sinha, D. Vaknin, D.C. Johnston, M.S. Alvarez, A.J. Jacobson, J.T. Lewandowski, and J.M. Newsam. Phys. Rev. B **38**, 2477 (1988).

[152] V.J. Emery. Phys. Rev. Lett. **58**, 2794 (1987).

[153] J. Zaanen, G.A. Sawatzky, and J.W. Allen. Phys. Rev. Lett. **55**, 418 (1985).

[154] J. Hubbard. Proceedings of the Royal Society of London Series A - Mathematical and Physical Sciences **276**, 238 (1963).

[155] N.F. Mott. Rev. Mod. Phys. **40**, 677 (1968).

[156] P.E. Sulewski, P.A. Fleury, K.B. Lyons, S.W. Cheong, and Z. Fisk. Phys. Rev. B **41**, 225 (1990).

[157] R. Coldea, S.M. Hayden, G. Aeppli, T.G. Perring, C.D. Frost, T.E. Mason, S.W. Cheong, and Z. Fisk. Phys. Rev. Lett. **86**, 5377 (2001).

[158] S. Shamoto, M. Sato, J.M. Tranquada, B.J. Sternlieb, and G. Shirane. Phys. Rev. B **48**, 13817 (1993).

[159] F.C. Zhang and T.M. Rice. Phys. Rev. B **37**, 3759 (1988).

[160] H. Ding, T. Yokoya, J.C. Campuzano, T. Takahashi, M. Randeria, M.R. Norman, T. Mochiku, K. Kadowaki, and J. Giapintzakis. Nature **382**, 51 (1996).

[161] M.R. Norman, H. Ding, M. Randeria, J.C. Campuzano, T. Yokoya, T. Takeuchi, T. Takahashi, T. Mochiku, K. Kadowaki, P. Guptasarma, and D.G. Hinks. Nature **392**, 157 (1998).

[162] D.S. Marshall, D.S. Dessau, A.G. Loeser, C.H. Park, A.Y. Matsuura, J.N. Eckstein, I. Bozovic, P. Fournier, A. Kapitulnik, W.E. Spicer, and Z.X. Shen. Phys. Rev. Lett. **76**, 4841 (1996).

[163] C. Renner, B. Revaz, J.Y. Genoud, K. Kadowaki, and O. Fischer. Phys. Rev. Lett. **80**, 149 (1998).

[164] C. Renner, B. Revaz, K. Kadowaki, I. Maggio-Aprile, and O. Fischer. Phys. Rev. Lett. **80**, 3606 (1998).

[165] S.H. Pan, J.P. O'Neal, R.L. Badzey, C. Chamon, H. Ding, J.R. Engelbrecht, Z. Wang, H. Eisaki, S. Uchida, A.K. Guptak, K.W. Ng, E.W. Hudson, K.M. Lang, and J.C. Davis. Nature **413**, 282 (2001).

[166] K.M. Lang, V. Madhavan, J.E. Hoffman, E.W. Hudson, H. Eisaki, S. Uchida, and J.C. Davis. Nature **415**, 412 (2002).

[167] N. Nagaosa and P.A. Lee. Phys. Rev. B **45**, 966 (1992).

[168] P.A. Lee. Physica C **408-10**, 5 (2004).

[169] J.L. Tallon, J.W. Loram, G.V.M. Williams, J.R. Cooper, I.R. Fisher, J.D. Johnson, M.P. Staines, and C. Bernhard. Phys. Stat. Sol. B **215**, 531 (1999).

[170] P.C. Dai, H.A. Mook, S.M. Hayden, G. Aeppli, T.G. Perring, R.D. Hunt, and F. Dogan. Science **284**, 1344 (1999).

[171] K. Berggold. diploma thesis, Universität zu Köln (2002).

[172] C. Zobel. PhD thesis, Universität zu Köln (2002).

[173] G.W. Gerlach. *Handbuch der Physik.* Springer Berlin (1928).

[174] Y.Y. Wang, L. Li, M.J. Naughton, G.D. Gu, S. Uchida, and N.P. Ong. Phys. Rev. Lett. **95**, 247002 (2005).

[175] N.P. Ong, Y.Y. Wang, L. Li, and M.J. Naughton. Phys. Rev. Lett. **98**, 119702 (2007).

[176] P. Spathis, H. Aubin, A. Pourret, and K. Behnia. arXiv:0712.2655 (2007).

[177] V.J. Emery and S.A. Kivelson. Nature **374**, 434 (1995).

[178] F. Rullier-Albenque, R. Tourbot, H. Alloul, P. Lejay, D. Colson, and A. Forget. Phys. Rev. Lett. **96**, 067002 (2006).

[179] C. Uher. J. Superconductivity **3**, 337 (1990).

[180] S.J. Hagen, Z.Z. Wang, and N.P. Ong. Phys. Rev. B **40**, 9389 (1989).

[181] R.C. Yu, M.B. Salamon, J.P. Lu, and W.C. Lee. Phys. Rev. Lett. **69**, 1431 (1992).

[182] S.D. Peacor, R.A. Richardson, F. Nori, and C. Uher. Phys. Rev. B **44**, 9508 (1991).

[183] S.T. Ting, P. Pernambucowise, and J.E. Crow. Phys. Rev. B **50**, 6375 (1994).

[184] A.V. Inyushkin, A.A. Taldenkov, and S.Yu. Shabanov. cond-mat/9710213 (1997).

[185] K. Krishana, N.P. Ong, Y. Zhang, Z.A. Xu, R. Gagnon, and L. Taillefer. Phys. Rev. Lett. **82**, 5108 (1999).

[186] K. Krishana, N.P. Ong, Q. Li, G.D. Gu, and N. Koshizuka. Science **277**, 83 (1997).

[187] K. Krishana, J.M. Harris, and N.P. Ong. Phys. Rev. Lett. **75**, 3529 (1995).

[188] M.B. Salamon, F. Yu, and V.N. Kopylov. J. Supercond. **8**, 449 (1995).

[189] R.M. Cleary. Phys. Rev. **175**, 587 (1968).

[190] R.P. Huebener, A.V. Ustinov, and V.K. Kaplunenko. Phys. Rev. B **42**, 4831 (1990).

[191] R.P. Huebener. Physica C **168**, 605 (1990).

[192] J.R. Cooper, S.D. Obertelli, A. Carrington, and J.W. Loram. Phys. Rev. B **44**, 12086 (1991).

[193] P.J. Ouseph and M.R. Obryan. Phys. Rev. B **41**, 4123 (1990).

[194] C. Sulkowski, T. Plackowski, and W. Sadowski. Phys. Rev. B **57**, 1231 (1998).

[195] A.J. Lowe, S. Regan, and M.A. Howson. Phys. Rev. B **44**, 9757 (1991).

[196] R.S. Liu, P.P. Edwards, Y.T. Huang, S.F. Wu, and P.T. Wu. J. of Solid State Chem. **86**, 334 (1990).

[197] Y.Y. Wang, S. Ono, Y. Onose, G. Gu, Y. Ando, Y. Tokura, S. Uchida, and N.P. Ong. Science **299**, 86 (2003).

[198] V. Oganesyan and I. Ussishkin. Phys. Rev. B **70**, 054503 (2004).

[199] D. Podolsky, S. Raghu, and A. Vishwanath. cond-mat/0612096v1 (2006).

[200] P.C. Li, S. Mandal, R.C. Budhani, and R.L. Greene. Phys. Rev. B **75**, 184509 (2007).

[201] D.N. Dias, E.S. Caixeiro, and E.V.L. de Mello. arXiv:cond-mat/0607075v2 (2007).

[202] Z.A. Xu, E. Ahmed, Z.W. Zhu, J.Q. Shen, and X. Yao. Physica C **460**, 833 (2007).

[203] A.M. Tsvelik and A.V. Chubukov. Phys. Rev. Lett. **98**, 237001 (2007).

[204] M. Franz. Nature **3**, 686 (2007).

[205] D.I. Khomskii. Basic aspects of modern solid state physics 2005.

[206] P.B. Visscher. Phys. Rev. B **10**, 943 (1974).

[207] P.B. Visscher. Phys. Rev. B **10**, 932 (1974).

[208] M. Granath, V. Oganesyan, S.A. Kivelson, E. Fradkin, and V.J. Emery. Phys. Rev. Lett. **87**, 167011 (2001).

[209] V.J. Emery, S.A. Kivelson, and O. Zachar. Phys. Rev. B **56**, 6120 (1997).

[210] J.M. Kosterlitz and D.J. Thouless. J. Phys. C – Solid State Phys. **6**, 1181 (1973).

[211] I. Hetel, T.R. Lemberger, and M. Randeria. Nature **3**, 700 (2007).

[212] D.R. Nelson and J.M. Kosterlitz. Phys. Rev. Lett. **39**, 1201 (1977).

[213] W. Schlabitz, J. Baumann, B. Pollit, U. Rauchschwalbe, H.M. Mayer, U. Ahlheim, and C.D. Bredl. Z. Physik B **62**, 171 (1986).

[214] M.B. Maple, J.W. Chen, Y. Dalichaouch, T. Kohara, C. Rossel, M.S. Torikachvili, M.W. Mc Elfresh, and J.D. Thompson. Phys. Rev. Lett. **56**, 185 (1986).

[215] C. Broholm, H. Lin, P.T. Matthews, T.E. Mason, W.J.L. Buyers, M.F. Collins, A.A. Menovsky, J.A. Mydosh, and J.K. Kjems. Phys. Rev. B **43**, 12809 (1991).

[216] H. Amitsuka, K. Matsuda, I. Kawasaki, K. Tenya, and M. Yokoyama. J. Magn. Magn. Mat. **310**, 214 (2007).

[217] R. Bel, K. Behnia, Y. Nakajima, K. Izawa, Y. Matsuda, H. Shishido, R. Settai, and Y. Onuki. Phys. Rev. Lett. **92**, 217002 (2004).

[218] M.S. Nam, A. Ardavan, S.J. Blundell, and J.A. Schlueter. Nature **449**, 584 (2007).

[219] W. Wu, I.J. Lee, and P.M. Chaikin. Phys. Rev. Lett. **91**, 056601 (2003).

[220] P. W. Anderson and P. Morel. Phys. Rev. **123**, 1911 (1961).

[221] J. Kondo. Prog. Theor. Phys. **32**, 37 (1964).

[222] M.A. Ruderman and C. Kittel. Phys. Rev. **96**, 99 (1954).

[223] T. Kasuya. Prog. Theor. Phys. **16**, 45 (1956).

[224] K. Yosida and M. Tachiki. Prog. Theor. Phys. **17**, 331 (1957).

[225] L. Chelmicki, J. Leciejewicz, and A. Zygmunt. J. Phys. Chem. Solids **46**, 529 (1985).

[226] T. Endstra, G.J. Nieuwenhuys, A.A. Menovsky, and J.A. Mydosh. J. Appl. Phys. **69**, 4816 (1991).

[227] T.T.M. Palstra, A.A. Menovsky, G.J. Nieuwenhuys, and J.A. Mydosh. J. Magn. Magn. Mat. **54-7**, 435 (1986).

[228] R.A. Steeman, E. Frikkee, S.A.M. Mentink, A.A. Menovsky, G.J. Nieuwenhuys, and J.A. Mydosh. J. Phys. – Condens. Matter **2**, 4059 (1990).

[229] T.T.M. Palstra. PhD thesis, unpublished (1986).

[230] G.J. Nieuwenhuys. Phys. Rev. B **35**, 5260 (1987).

[231] A. Otop. PhD thesis, TU Braunschweig (2006).

[232] N.H. Andersen. *Crystalline Electric Field and Structural Effects in f-electron Systems.* Plenum, New York (1980).

[233] K. Berggold, J. Baier, D. Meier, J.A. Mydosh, T. Lorenz, J. Hemberger, A. Balbashov, N. Aliouane, and D.N. Argyriou. Phys. Rev. B **76**, 094418 (2007).

[234] K. Behnia, D. Jaccard, and J. Flouquet. J. Phys. – Condens. Matter **16**, 5187 (2004).

[235] N.H. vanDijk, F. Bourdarot, J.C.P. Klaasse, I.H. Hagmusa, E. Bruck, and A.A. Menovsky. Phys. Rev. B **56**, 14493 (1997).

Publications

Publications of this thesis

1. **Magnetothermal evidence of a partial gap at the Fermi surface of $\mathbf{UPt_2Si_2}$**
   N. Johannsen, S. Süllow, A.V. Sologubenko, T. Lorenz and J.A. Mydosh
   Physical Review B **78**, 121103(**R**) (2008)

2. **Nernst effect in $\mathbf{NdBa_2\{Cu_{1\text{-}y}Ni_y\}_3O_{7-\delta}}$ (y=0-0.12)**
   N. Johannsen, Th. Wolf, A.V. Sologubenko, T. Lorenz, A. Freimuth and J.A. Mydosh
   Physical Review B **76**, 020512(**R**) (2007)

3. **Invited talks**
   a) **Nernst Effect of Ni-doped $\mathbf{NdBa_2Cu_3O_{7-\delta}}$**
      MPI CPfS, Nöthnitzer Str. 40, Dresden (14.2.08)

   b) **Thermal expansion and Magnetostriction of TlCuCl3**
      AG Lang, Physikalisches Institut Frankfurt (24.5.04)

4. **Conference contributions**
   - Spring Meeting of the DFG Working Committee for solid state physics in the years 2003 to 2008.
   - Workshop of SFB 608 on Quantum Matter, October 2007

   - International Workshop of SFB 608 on Strongly Correlated Transition Metal Compounds, Cologne 2005

Other publications

1. **Uniaxial pressure dependencies of the phase boundary of $\mathbf{TlCuCl_3}$**
   N. Johannsen, A. Oosawa, H. Tanaka, A. Vasiliev, and T. Lorenz
   Physica B 378-380, 1043 (2006)

2. **Magnetoelastic Coupling in the Spin-Dimer System $\mathbf{TlCuCl_3}$**
   N. Johannsen, A. Vasiliev, A. Oosawa, H. Tanaka, and T. Lorenz
   Phys. Rev. Lett. **95**, 017205 (2005).

Danksagung

Bleibt mir zu guter Letzt noch allen zu danken, die zu dieser wirklich sehr schönen Zeit der letzten Jahre beigetragen haben. Zuerst natürlich bei Prof. Freimuth der mir diese Arbeit erst möglich gemacht hat. Das etwas exotischere Thema "Nernst Effekt" hat genau den Puls der Zeit getroffen, der Hype läuft auch noch... Das hat natürlich richtig Spaß gemacht.

Prof. Mydosh möchte ich auch sehr herzlich danken. Seine Unterstützung war immer sehr prompt: ...Niko, i am already working on it...als Erwiderung auf die Zusendung meines Manuskripts in den Feiertagen um Ostern. Auch Danke für die tolle Werbung für mein Paper unter dem "who is who" der Supraleitungskoryphäen in Aspen.

Thomas Lorenz danke ich erstmal für viel gemeinsamen Spaß und Humor im Institut, nach wie vor wird viel gelacht! Natürlich zeichnet er auch für einige schöne Formulierungen dieser Arbeit verantwortlich: ab jetzt wird "Yet" öfter mal eingebaut. In letzter Zeit häuften sich auch wieder die berühmten "Zettel"-sessions...Gemeinsam auf dem Weg zu neuen Erkenntnissen.

Dabei kann ich jetzt eigentlich auch nahtlos dazu übergehen, dem "Paper-Team" zu Danken. Alex Sologubenko - ich hoffe wir oder Du packen das MgB2 noch -, John und Thomas. Diskussionen im Team sind großartig!

Prof. Schadschneider möchte ich an dieser Stelle dafür danken, daß er, wie schon in meiner Diplomarbeit Zweitgutachter geworden ist, woran sein wohlgelaunter Kalender nicht ganz unschuldig war.

Prof. Ruschewitz danke ich für den Vorsitz.

Thomas Wolf vom IFP in Karlruhe danke ich für die zuverlässige Zusammenarbeit. Die Proben waren erstklassig!

Komme ich jetzt doch erstmal zu Zimmer 218. Was für ein Kosmos sich doch hinter einer einfachen Tür verbergen kann. Olli Heyer, eine Seelenverwandschaft! Kurzweil auf allen Gebieten und eine kämpferische Konkurrenz um den gnadenlosen Hirsch-index. Mal sehen wer sich zuerst von der Zwei entfernt.. Martin Valldor, der alte Schwede und "Heavy Metal" Chemiker, der die Physik auch mal aus anderen Winkeln ausleuchtet. Insgesamt eine herrliche Kombination in diesem Raum. Schade, daß auch die schönsten Zeiten mal zu Ende gehen. Auch unsere Ehemaligen 218'ner müssen hier unbedingt Erwähnung finden: Holger Joth - geteilter Rückenschmerz ist halber Rückenschmerz! Unvergessen sind auch unsere Frikadellen-Ap-Samstage. Und Mohammed Benomar als gelebtes Vorbild an arabisch-mediterraner Gelassenheit.

Meinen Nachbarn, Christina Hilgers "Hengeln" und Carsten danke ich natürlich für aufpeppelnde Mahlzeiten, gemeisames Bouldern und Klettern und Korrekturlesungen. Das ist ja jetzt auch abseits der Uni schon eine lange Freundschaft, die hoffentlich auch noch lange währt. Genauso wie mit den Mitgliedern unserer erweiterten Haus-Wg, Anika und Holger, welchen ich während der gesamten Zeit immer wieder kulinarische Köstlichkeiten und entspannende Zocker-Abende zu verdanken hatte. Rita und Phillip sorgten auch für angenehme Ablenkungen diversester Art.

Eva Benckiser danke ich für die unzähligen Kletterfahrten, mal sie, mal ich, und einfach viel Spaß in der ganzen Zeit.

Kai Berggold danke ich für diverse Skripte und das KSR und natürlich auch für die Begeisterung für meine Skripte, auch wenn hier sonst niemand "antisymmetrisiert". Auch für schöne Parties.

Olaf Schumann sei gedankt für das gemeinsame Interesse erstmal an vernünftigen Betriebssystemen, sich daran quasi direkt anschließend für den unermüdlichen Einsatz an der Netzwerk-Front. VPN war Gold wert! Jonas danke ich auf dem gleichen Weg.

Den neuen Doktoranden Jens und Kerstin danke ich auch und wünsche weiterhin viel Spaß. Den sonstigen Ehemaligen wie Jörg, Daniel, Mathias und allen anderen für eine schöne Zeit und interressante Gespräche.

Der Dienstags-Radgruppe für die nachwievor anhaltende Schnittjagt und viel Unsinn zwischendurch.

Den neuen Diplomanden ebenso.

Besonderer Dank natürlich auch an Rolf Dommel. Ohne das Helium wäre selbstverständlich nichts gelaufen. Auch für ein nettes Schwätzchen zwischendurch, gelegentlich auch mal bei einem kleinen Umtrunk. Ebenso den gesamten Werkstätten. Dank auch an Ralf Müller für Kaffee und Wasserversorgungen. Ich glaube ich war einer der besten Kunden.

Nun noch einen sehr herzlichen Dank an die Menschen, die mich auch privat ertragen müssen. Meinen Eltern, meinem Bruder Daniel (der "Gimp"-Experte) und meiner Freundin Tine, die mich einfach bei allem unterstützen.

Offizielle Erklärung

Ich erkläre, dass ich die von mir vorgelegte Dissertation selbstständig angefertigt, die benutzten Quellen und Hilfsmittel vollständig angegeben und die Stellen der Arbeit - einschließlich Tabellen, Karten und Abbildungen -, die anderen Werken im Wortlaut oder dem Sinn nach entnommen sind, in jedem Einzelfall als Entlehnung kenntlich gemacht habe; dass diese Dissertation noch in keiner anderen Fakultät oder Universität zur Prüfung vorgelegen hat; dass sie - abgesehen von den in der Publikationsliste angegebenen Teilpublikationen - noch nicht veröffentlicht worden ist sowie, dass ich eine solche Veröffentlichung vor Abschluss des Promotionsverfahrens nicht vornehmen werde. Die Bestimmungen dieser Promotionsordnung sind mir bekannt. Die von mir vorgelegte Dissertation ist von
Prof. Dr. A. Freimuth betreut worden.

Köln, den 7. Mai 2008

Niko Johannsen

Abstract

In this thesis, the Nernst effect in high-temperature superconductors is investigated. This effect gained much interest because it is usually very small in metals and was found to display a large signal in the vortex liquid phase of the high-T_c's. The more surprising that large Nernst voltages were found to survive up to temperatures that reach far out of the superconducting phase [4]. This was extensively studied thereafter in wide doping range of the high-T_c's [9]. We were able to significantly expand these studies by tuning T^* and T^ν independently. This was done by inducing Ni ions into the CuO planes of $NdBa_2\{Cu_{1-y}Ni_y\}_3O_{7-\delta}$ [10] which allowed to study the Nernst effect in a wide parameter range. This is done on one hand in dependence of the oxygen content which varies the charge carrier concentration. On the other hand, the Ni concentration is varied from 0% to 12%, thereby enhancing T^* and simultaneously suppressing T_c with increasing concentrations. So to say, a third axis is accessed in the phase diagram of the cuprates. The temperatures to which the anomalous Nernst signal is detectable is the onset temperature T^ν. The goal of this work was to find out whether T^ν follows T_c or T^*, since both can be influenced by altering the charge carrier content or the impurity concentration. The onset temperatures of the anomalous Nernst signals are determined as the slightest detectable deviation from the quasiparticle background above T_c. Overall, T^ν clearly does not track the enhanced pseudogap temperatures in any sample series that is investigated in this work [24].

In the second part of this work, the Nernst effect and other transport properties of UPt_2Si_2, including electrical ones such as the resistivity and the Hall effect and thermal ones, as the thermal conductivity, the thermopower and the Righi-Leduc effect were investigated. These investigations were motivated by the findings of a giant Nernst effect in the related system URu_2Si_2 [11]. And indeed, a pronounced Nernst signal was found also in UPt_2Si_2. In an early theory, published in 1972, Abelskii and Dik *et al.* [13, 14] calculated the thermopower and the Nernst coefficient for a generic antiferromagnet under the assumption of a gapping of the Fermi surface at T_N in addition to phonon and spin scattering mechanisms. These calculations astonishingly well predict the behavior of the measured quantities of UPt_2Si_2. The onsets of the signals as well as the maxima positions meet the forecasts of the theory. Thus, the emergence of the Nernst signal is ascribed to an opening of a gap at the Fermi surface. Yet, this gapping cannot affect the whole Fermi surface, otherwise the system would undergo a metal-to-insulator transition, which is not seen in the resistivity [26]. This scenario of a partial gapping is consistent with a recent publication of electronic transport and neutron diffraction studies [12].

Kurzzusammenfassung

In dieser Arbeit wurde der Nernst-Effekt an Hochtemperatursupraleitern untersucht. Dieser Effekt gewann in letzter Zeit deutlich an Bedeutung durch seine auffallend großen Werte in der Flußschlauchphase von Hochtemperatursupraleitern. In normalen Leitern ist dieser Effekt verschwindend klein. Da diese anormal großen Werte mit charakteristischem Profil eigentlich nur in der supraleitenden Phase auftreten war es umso überraschender, erhöhte Nernst-Spannungen auch in der normalleitenden Phase oberhalb der Sprungtemperatur (T_c) anzutreffen [4]. Konsequenterweise wurde dieser Bereich in Abhängigkeit der Ladungsträgerdotierung intensiv untersucht [9]. In dieser Arbeit konnte eine solche Studie deutlich erweitert werden. In dem System $NdBa_2\{Cu_{1\text{-}y}Ni_y\}_3O_{7-\delta}$ ist es möglich, durch Ni-Dotierung einerseits T_c zu unterdrücken und andererseits die Pseudogap-Temperatur T^* zu vergrößern. Ni-Dotierungen in diesem System lassen die Ladungsträgerkonzentration im wesentlichen unverändert. In Abhängigkeit der Ni-Konzentration und des Sauerstoffgehalts konnte so systematisch das Verhältnis zwischen der Temperatur bis zu welcher das Nernst-Signal nachgewiesen werden konnte (T^ν) und T^* untersucht werden. Als Ergebnis ist festzuhalten, daß in keiner der gemessenen Probenserien eine Relation von T^ν und T^* hergestellt werden konnte [24].

Im zweiten Teil wurden Transporteigenschaften von UPt_2Si_2 mit Betonung des Nernst Effektes untersucht. Es konnte das Auftreten eines Nernst Signals parallel mit dem Übergang in die Antiferromagnetische Phase bei 31.5 K nachgewiesen werden. Ähnliche Anstiege sind in der Thermokraft und dem Hall Effekt zu beobachten. Nach theoretischen Vorhersagen von 1972 für einen modellhaften Antiferromagneten, sind diese Anstiege eine Folge des Auftretens einer Energielücke für Ladungsträger in der Fermi-Fläche [13, 14]. Da das System, wie durch Widerstandmessungen gezeigt wurde, jedoch keine Anzeichen eines Wechsels zu isolierendem Verhalten zeigt, wird diese Energielücke nur einem Teil der Fermi-Fläche zugeschrieben [26].